

**EXPERIMENTAL AND NUMERICAL STUDY
ON CORROSION-INDUCED DAMAGES ON
REINFORCED CONCRETE STRUCTURES**

QIAO Di

EXPERIMENTAL AND NUMERICAL STUDY ON CORROSION-INDUCED DAMAGES ON REINFORCED CONCRETE STRUCTURES

By

QIAO Di

A Dissertation Submitted to Nagoya University
In Partial Fulfillment of the Requirements for
The Degree of Doctoral of Engineering

Department of Civil Engineering
Graduate School of Engineering, Nagoya University
Nagoya, JAPAN

ABSTRACT

In recent years, deterioration of reinforced concrete (RC) structures caused by chloride-induced corrosion of reinforcing steel bars has been a growing concern for durability of structures. Rebar corrosion may result in several types of damages on RC structures: loss of effective concrete section due to concrete cracking and cover spalling, loss of rebar tensile performance due to a reduced cross section and reduced bond strength between corroded rebars and the concrete. These damages can compromise the load bearing capacity of an RC structure. In addition to these effects on structural safety, corrosion may also lead to falling concrete, which increases the risk to human safety. Therefore, it is of great importance to fully understand the influences of corrosion on RC structures. Meantime, a reliable means to assess the residual strength and crack development is essential. Such a method could contribute to optimized and efficient maintenance work that would extend the service life of RC structures in corrosive environments. This study aims to clarify the corrosion-caused damages in three-dimensional level, where crack propagation and cover spalling as well as tensile performance of corroded rebars influenced by various corrosion distributions around or along the rebar are focused. On the other hand, a time-dependent electro-mechanical model based on Rigid Body Spring Method (RBSM) is developed for the evaluation of both concrete cracking and tensile degradation of rebars due to corrosion.

In order to better simulate the natural corrosion state of rebars resulting from chloride attack, an electric corrosion method using a salt-water pool on concrete cover is introduced for the experimental study. The development of corrosion degree and the corrosion profiles represented by radius losses along the rebar surface are investigated as a basic study. It shows that the cracks generated in concrete cover may cause an increase of corrosion rate on the rebar portion nearby. A simple method for simulating various corrosion profiles by bare rebars and different cathode arrangements is also proposed. The use of a small cathode is confirmed to be able to concentrate the resulting corrosion to a certain extent.

The 2D concrete cracking behavior caused by rebar corrosion is examined experimentally and analytically. Different cover thicknesses as 10 and 30mm are considered. The corrosion-expansion model based on RBSM is used in the analysis, which takes into account non-uniform corrosion around the rebar. Parametric studies

using the corrosion-expansion model are carried out to investigate the effects of the corrosion distribution around the rebar and concrete material properties on crack propagation respectively. The results indicate that internal crack pattern is strongly related to the corrosion distribution rather than cover thickness as suggested by the theoretical crack pattern. Surface crack initiation is determined by tensile strength of concrete, while the propagation of surface crack is delayed with an increase of fracture energy.

In comparison with the 2D cracking behavior, the 3D crack propagation caused by local corrosion along the rebar length is investigated. In the experiments, a local corrosion state, that is corrosion concentrates at the center part of the rebar, is simulated using salt-water pools of various sizes and the corresponding crack patterns are studied. In the analysis, the corrosion-expansion model is applied to examine the crack propagation and potential cover spalling by assuming a similar distribution of corrosion amount along the rebar to the test results. The test and analysis both demonstrate that the internal crack patterns vary along the rebar length direction. At the area where the concentrated corrosion occurs, lateral cracks incline to the concrete surface instead of propagating to the concrete sides as shown in 2D cracking behavior. Outside this area, vertical cracks are dominant.

The tensile behavior of rebars corroded with various corrosion profiles is investigated with a digital image processing method. Both bare-rebar specimens and those corroded in concrete are tested, showing that tensile degradation resulting from corrosion is closely related to radius loss variability along the rebar length. Local corrosion may lead to a more tensile degradation. For the evaluation of tensile behavior, a numerical model based on RBSM incorporated with a truss network is proposed, which takes into consideration corrosion profile. Good agreement with the test data is obtained with this model, which offers an accurate method of estimating the residual tensile capacity of corroded rebars.

A time-dependent electro-mechanical model based on RBSM is developed for the combined analysis of concrete cracking and tensile degradation of rebars due to corrosion. The proposed model is verified with the test results of the basic study. The analysis of cracking process by this model is also carried out for the local corrosion cases. The model can be used to establish a numerical model to assess the damage extent of RC structures exposed to corrosion and to estimate their remaining service lives as well as to design repair strategies.

ACKNOWLEDGEMENTS

First and foremost, I would like to express my sincerest gratitude to my supervisor, Professor Hikaru Nakamura, who guided, inspired, assisted, and supported me to pursue a doctoral degree. Throughout my study, he provided encouragement, insightful discussions, valid advice and lots of good ideas. Without his patience and great efforts, this dissertation would have never been completed. I am very thankful to Associate Professor Yoshihito Yamamoto for his enthusiasm and his help in numerical simulations. Sincere thanks also go to the other members of my examination committee: Professor Toshiaki Mizobuchi of Hosei University, Professor Yoshito Itoh and Professor Kazuo Tateishi for their time and valuable feedback on this dissertation.

I would like to thank all members of Concrete Laboratory for the great times we shared. I gratefully acknowledge Dr. Taito Miura for his kind supports during my experimental work. I am particularly thankful to Mr. Chen Ju, my former tutor, for his valuable friendship and continuous helps during my first year in Japan.

I would like to pay special thankfulness and appreciation to Prof. Itoh's Laboratory for providing the laser meter for my experimental study. I am indebted to Dr. Mikihiro Hirohata for several discussions that helped me to solve the problem of laser meter. For all technical assistance during rebar tensile tests, I wish to thank Mr. Hiroya Nakashima.

I gratefully acknowledge that the Ministry of Education, Culture, Sports, Science and Technology (Monbukagakusho) provided me with a scholarship for my study in Nagoya University.

I am deeply thankful to my parents, Mr. Zhengfu Qiao and Mrs. Fengmei Yan, for their love, support, encouragement and sacrifices. The last word of thanks I have saved for my wife, Ning Su, who is the best thing in my life.

Table of Contents

ABSTRACT	I
ACKNOWLEDGEMENTS	III
Table of Contents	IV
List of Tables.....	VIII
List of Figures	IX
1 General Introduction	1
1.1 Background	1
1.2 Literature review	4
1.2.1 Corrosion-induced cracking behavior	4
1.2.2 Surface crack width propagation.....	6
1.2.3 Analysis of concrete cracking caused by rebar corrosion	7
1.2.4 Tensile performance of corroded rebars and evaluation method	8
1.3 Study objective and research significance	9
1.4 Organization of dissertation contents.....	10
2 Development of Electric Corrosion Method for Controlled Corrosion Profile	14
2.1 Introduction.....	14

2.2	Electric corrosion test on single-rebar concrete specimens	15
2.2.1	Test setup and procedure.....	15
2.2.2	Corrosion degree and profile.....	20
2.2.3	Concrete crack pattern.....	23
2.3	Electric corrosion test on bare rebar specimens using different cathode arrangements	24
2.3.1	Experimental program.....	24
2.3.2	Corrosion degree and profile.....	26
2.4	Summary and conclusions	30
3	Evaluation of 2D Concrete Cracking caused by Rebar Corrosion	32
3.1	Introduction.....	32
3.2	Experimental setup.....	33
3.3	Test results	35
3.4	Analytical model	38
3.4.1	Three-dimensional RBSM.....	38
3.4.2	Material models.....	38
3.4.3	Corrosion-expansion model	39
3.4.4	Modeling for non-uniform corrosion around the rebar	41
3.5	Analytical results in comparison to test data	41
3.6	Effect of corrosion distribution around rebar.....	43
3.7	Effect of concrete material properties	48
3.8	Summary and conclusions	53
4	Evaluation of 3D Concrete Cracking and Cover Spalling due to Local Corrosion	55
4.1	Introduction.....	55

4.2	Experimental setup.....	56
4.3	Experimental results.....	58
4.3.1	Corrosion distribution along rebar	58
4.3.2	Concrete crack pattern.....	59
4.3.2.1	30mm cover case	59
4.3.2.2	10mm cover case	62
4.4	Analysis outlines	65
4.5	Analytical results and discussions.....	66
4.6	Summary and conclusions	72
5	Experimental Investigation of Tensile Behavior of Corroded Rebars.....	74
5.1	Introduction.....	74
5.2	Test series.....	75
5.3	Uniaxial tensile tests and digital image processing	77
5.4	Tensile test results	79
5.5	Summary and conclusions	83
6	Evaluation Method of Tensile Performance of Corroded Rebars.	84
6.1	Introduction.....	84
6.2	Truss Network.....	85
6.3	Rebar material model	85
6.4	Analytical procedures.....	87
6.5	Analytical results compared with test data.....	90
6.5.1	Corrosion profiles.....	90
6.5.1.1	Uniform cases	90
6.5.1.2	Quarter cases.....	93

6.5.2	Evaluation of tensile performance.....	94
6.6	Summary and conclusions	97
7	Development of Electro-mechanical Model for Combined Analysis of Corrosion-caused Damage	98
7.1	Introduction.....	98
7.2	Analytical process flow.....	99
7.3	Analytical results.....	103
7.3.1	Electric corrosion process	103
7.3.2	Internal crack pattern.....	107
7.3.3	Tensile behavior of corroded rebars.....	108
7.4	Application in local corrosion case.....	110
7.5	Summary and conclusions	115
8	Summary and Conclusions.....	116
8.1	Conclusions.....	116
8.2	Recommendations for future study	119
	References	120

List of Tables

Table 2.1 Mixture proportions of concrete	18
Table 2.2 Test series on single-rebar specimens	18
Table 2.3 Test variables for corrosion test using bare rebars	26
Table 3.1 Test conditions for study of 2D cracking behavior	34
Table 4.1 Test variables for study of 3D cracking behavior	57
Table 5.1 Test series for tensile performance of corroded rebars	75
Table 6.1 Parameters used in potential distribution analysis (Conyers 2013).....	88
Table 7.1 Test conditions of single-rebar specimens carried out	99

List of Figures

Figure 1.1 Electrochemical mechanism of chloride-induced corrosion	2
Figure 1.2 Service life of RC structures subjected to chloride-induced corrosion.....	3
Figure 1.3 Bažant’s cracking mode	5
Figure 1.4 Tsutsumi’s criterion for internal crack pattern.....	5
Figure 1.5 Organization of the dissertation	11
Figure 2.1 Distribution of corrosion products layer (Yuan & Ji, 2009).....	15
Figure 2.2 Classic electric corrosion method	16
Figure 2.3 Test of single-rebar specimen using classic method.....	16
Figure 2.4 Diagram of electric corrosion test.....	17
Figure 2.5 Electric corrosion test using salt-water pool	19
Figure 2.6 Measuring corrosion profiles by laser meter.....	20
Figure 2.7 Measured corrosion degree	21
Figure 2.8 Measured radius losses along rebar.....	21
Figure 2.9 Rebar cross section after corrosion	22
Figure 2.10 Ratio of radius losses between top and bottom sides.....	22
Figure 2.11 Internal crack patterns under various corrosion amounts	23
Figure 2.12 Diagram of one experimental unit using bare rebar.....	25
Figure 2.13 Preparation of corroded rebar specimens by electric corrosion method.....	26

Figure 2.14 Measured corrosion degree in the test with bare rebars	27
Figure 2.15 Corrosion profiles for uniform cases (3% corrosion)	28
Figure 2.16 Corrosion profiles for uniform cases (9% corrosion)	28
Figure 2.17 Corrosion profiles for uniform cases (15% corrosion)	29
Figure 2.18 Experimental observation (corrosion products adhered to rebar surface) ..	29
Figure 2.19 Corrosion profiles for quarter cases	30
Figure 3.1 Specimen dimension for studying 2D cracking behavior	33
Figure 3.2 Electric corrosion test for 2D cracking behavior	34
Figure 3.3 Measured distribution of corrosion degrees for RC10 and RC30.....	35
Figure 3.4 Surface cracking states for RC10 and RC30 (top view)	36
Figure 3.5 Corrosion states of rebar samples	36
Figure 3.6 Internal crack patterns for RC10 and RC30.....	37
Figure 3.7 Voronoi particle definition of RBSM element.....	38
Figure 3.8 Concrete material model	39
Figure 3.9 Corrosion-expansion model (Tran et al. 2011)	40
Figure 3.10 Non-uniform corrosion model	41
Figure 3.11 3D view of RBSM model.....	42
Figure 3.12 Simulated internal crack patterns for RC10 and RC30.....	43
Figure 3.13 Comparison of internal crack patterns between different corrosion distributions (2.5% corrosion)	44
Figure 3.14 Comparison of internal crack patterns between different corrosion distributions (5% corrosion)	44
Figure 3.15 Surface crack evolution for different corrosion distributions (240.5mm side- cover)	46

Figure 3.16 Comparison of internal crack patterns between different corrosion distributions (90.5mm side-cover).....	47
Figure 3.17 Internal crack patterns observed in test (Kawamura et al. 2010).....	47
Figure 3.18 Surface crack evolution for different side-cover thicknesses	48
Figure 3.19 Concrete surface deformation for different side-cover thicknesses.....	48
Figure 3.20 Stress-displacement relationships investigated for effects of concrete material properties	49
Figure 3.21 Surface crack development for various tensile strengths.....	50
Figure 3.22 Surface crack development for various fracture energies	51
Figure 3.23 Internal crack pattern of specimen with a width of 150mm.....	52
Figure 3.24 Internal crack pattern of specimen with a width of 600mm.....	52
Figure 3.25 Lateral crack length of specimen with a width of 600mm varied in fracture energy	53
Figure 4.1 Practical case of local corrosion-induced concrete spalling	56
Figure 4.2 Electric corrosion test for 3D cracking behavior	57
Figure 4.3 Cutting position for investigating internal crack pattern.....	58
Figure 4.4 Measured distribution of corrosion degree	59
Figure 4.5 Surface crack patterns of test specimens with 30mm cover	60
Figure 4.6 Internal crack patterns of test specimens with 30mm cover	61
Figure 4.7 Surface crack patterns of test specimens with 10mm cover	63
Figure 4.8 Internal crack patterns of test specimens with 10mm cover	63
Figure 4.9 Assumed corrosion distributions for analysis	65
Figure 4.10 Corrosion states around rebar at different positions in test.....	66
Figure 4.11 Simulated surface crack patterns for local corrosion	67

Figure 4.12 Simulated internal crack patterns for local corrosion	68
Figure 4.13 Deformation under various corrosion distributions (magnification $\times 50$) 3% corrosion	69
Figure 4.14 Concrete surface deformation caused by various corrosion distribution	70
Figure 4.15 Evaluation of spalling area	71
Figure 5.1 Typical corrosion profiles of rebar specimens in tensile testing.....	76
Figure 5.2 Tensile test setup	78
Figure 5.3 Comparison of local stress-strain relationships obtained by strain gauges and image processing method (U10-9%)	79
Figure 5.4 Effect of circumferential corrosion state on tensile performance	81
Figure 5.5 Effect of longitudinal corrosion state on tensile performance	82
Figure 6.1 Truss network.....	85
Figure 6.2 Stress-strain relationship of sound rebars (Kato 1979).....	86
Figure 6.3 Applicability of stress-strain relationship in simulations.....	86
Figure 6.4 Analytical process flow for evaluating tensile behavior of corroded rebars.	87
Figure 6.5 Analytical model for analysis of potential distribution.....	88
Figure 6.6 Calculation of degradation factors	90
Figure 6.7 Influence of adhered corrosion products on the potential distribution	91
Figure 6.8 Comparison of simulated corrosion profiles to test results (uniform cases).	92
Figure 6.9 Comparison of potential distribution between uniform and quarter cases....	93
Figure 6.10 Comparison of simulated corrosion profiles to test results (quarter cases)	93
Figure 6.11 Comparison of simulated load-deformation relationships to test results....	94
Figure 6.12 Estimates of residual tensile strength and elongation of corroded rebars...	95
Figure 6.13 Comparison of simulated local strain profiles to test results	96

Figure 7.1 Three-phase material model	100
Figure 7.2 Coupled electro-mechanical model.....	101
Figure 7.3 Relation of current efficiency to crack width.....	102
Figure 7.4 Potential distribution at the center section of the specimen.....	103
Figure 7.5 Simulated rebar section without crack effect.....	104
Figure 7.6 Modeled ratio of radius losses between top and bottom sides.....	105
Figure 7.7 Verification of relationship between crack width and current efficiency ...	106
Figure 7.8 Simulated rebar section with crack effect	106
Figure 7.9 Modeled radius losses along rebar	106
Figure 7.10 Simulated internal crack patterns	108
Figure 7.11 Simulated load-deformation relationships of corroded rebars.....	109
Figure 7.12 Simulated local strain profiles.....	109
Figure 7.13 Electric boundary conditions for local corrosion case	110
Figure 7.14 Potential distributions at different sections for L300C30	111
Figure 7.15 Potential distributions at different sections for L100C30	111
Figure 7.16 Simulated corrosion distributions along rebar	113
Figure 7.17 Simulated surface crack patterns by electro-mechanical model	114
Figure 7.18 Simulated internal crack patterns by electro-mechanical model.....	114

1 General Introduction

1.1 Background

Corrosion of reinforcing steel bars is a principal cause of deterioration of reinforced concrete (RC) structures. In recent years, durability of RC structures affected by rebar corrosion has been a significant concern, especially for structures in marine environments or road structures exposed to de-icing salts. Corrosion can cause several types of damages on RC structures: loss of effective concrete section due to concrete cracking and cover spalling, loss of rebar tensile performance due to a reduced cross section and decreased bond strength between corroded rebars and the concrete. These damages may compromise the load-bearing capacity of an RC structure. In addition to the effects on structural safety, corrosion may also lead to falling concrete, which increases the risk to human safety. The maintenance and reparation of structures damaged by rebar corrosion can cause relatively high direct and indirect costs (Yunovich and Thompson 2003).

Corrosion of a rebar embedded in concrete is a very complicated process. Normally, a passive film that is formed due to the highly alkaline environment of concrete protects the rebar from corrosion (Gouda and Halaka 1970). However, it can be destroyed through the ingress of chloride ions or the carbonation of the concrete cover, triggering the corrosion process. Figure 1.1 shows a schematic of electrochemical mechanism of chloride-induced corrosion in concrete (Bertolini et al. 2004). A rebar area becomes depassivated when the chloride concentration of the concrete nearby reaches a threshold value. It acts as the anode where iron is oxidized, while the adjacent areas still with passive films are the cathodes where oxygen reduction occurs. The transport of electrons within the rebar from the anode to the cathode associated with the transport of hydroxyl ions OH^- within concrete towards the anodic area constitute a

circuit of electric current. In this way, ferrous hydroxide $\text{Fe}(\text{OH})_2$ is formed, which further reacts with oxygen and water to form typical red rust.

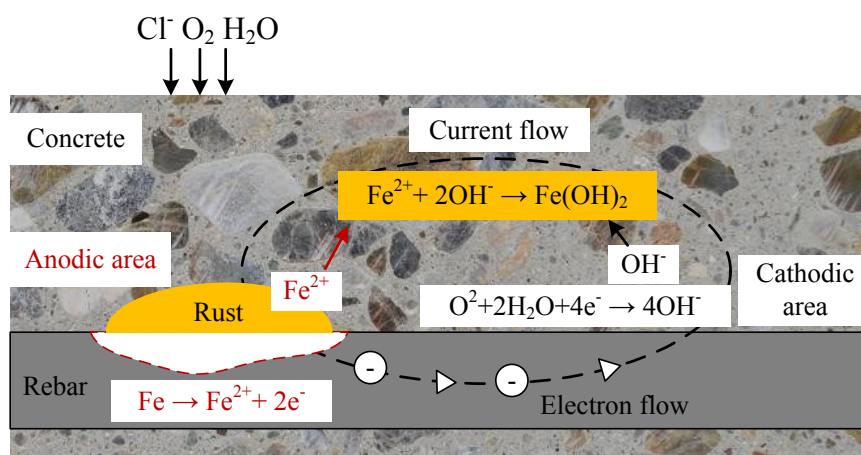


Figure 1.1 Electrochemical mechanism of chloride-induced corrosion

The JSCE standard specifications for concrete structures (JSCE 2002) define the service life of RC structures subjected to chloride-induced rebar corrosion as four stages: initial stage, propagation stage, acceleration stage and deterioration stage, which is illustrated in Figure 1.2. The first stage is considered to be the time period until the start of corrosion in structures, within which chloride ions gradually penetrate into concrete and accumulate at the rebar surface. The second stage is defined as the time period from the initiation of corrosion to the appearance of concrete cracks. As corrosion propagates, the corrosion products generated build up tensile stresses on the surrounding concrete due to a greater volume than that of the original rebar, which eventually leads to concrete cracking. In the third stage, cracks enable a faster transport of chloride, oxygen and water, causing a higher corrosion rate than that of propagation stage. The affected structures demonstrate a considerable damage level, i.e. cracks become wide and connected, and the cross-sectional areas of rebars are obviously reduced, resulting in a loss of tensile capacity. The occurrence of excessive concrete deflection or cover spalling is often considered as the boundary between acceleration stage and deterioration stage, which also indicates the serviceability limit state (Andrade et al. 1993b, Li et al. 2004, Akiyama et al. 2014). The fourth stage is the time period up to final collapse due to a complete loss of strength.

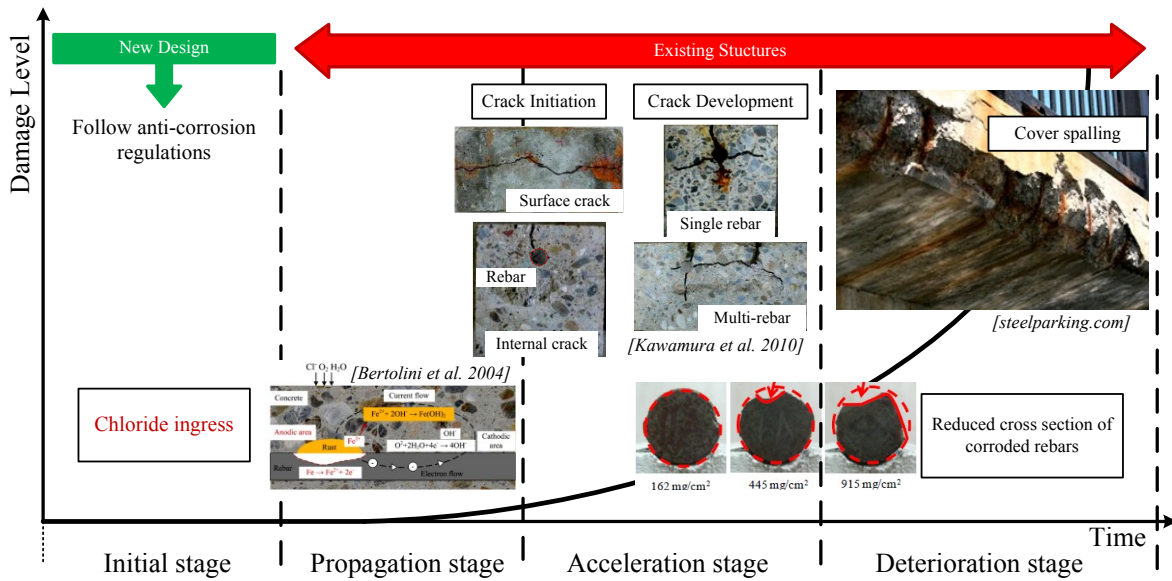


Figure 1.2 Service life of RC structures subjected to chloride-induced corrosion

In order to extend the service life of RC structures in corrosive environments, an appropriate time for repair or rehabilitation should be determined. Hence, it is of great importance to assess the damage level of corroded structures, which requires sufficient knowledge of corrosion-induced concrete cracking and spalling behavior as well as the tensile performance of corroded rebars. A certain amount of studies relating to these aspects have been reported. The experimental investigations were conducted to study crack initiation (Andrade et al. 1993b, Alonso et al. 1998, Nguyen et al. 2006) and crack propagation (Tsutsumi et al. 1996, Kawamura et al. 2010). The theoretical crack patterns proposed by Bažant (1979) and Tsutsumi et al. (1996) indicate the geometric conditions of cross section of a concrete member for the occurrence of cover spalling. The tests concerning tensile behavior of corroded rebars were also carried out (Cairns et al. 2005, Du et al. 2005), with which empirical equations for the estimation of residual tensile capacity were given. Although these results are contributable to the evaluation of corrosion-caused damages on RC structures, there is a lack of data about the effects of corrosion distribution. On the other hand, a number of analytical studies were performed to simulate the corrosion-induced cracking process. In comparison to the test results, they can simulate well crack initiation and propagation with considerations of penetration of corrosion products into concrete pores and cracks (Toongoenthong and

Maekawa 2005, Val et al. 2009, Tran et al. 2011, Michel et al. 2014) and non-uniform corrosion around the rebar (Du et al. 2006, Tran et al. 2011). However, the analytical studies are limited to two-dimensional cracking behavior, where local corrosion along the rebar is not considered. Moreover, there is no model capable of evaluation of both concrete cracking and tensile degradation of corroded rebars, which is an important component in the analytical models required to assess corrosion-induced damages of RC structures. The present research situation accordingly gives rise to the need for this study, which attempts to study the damages caused by rebar corrosion both experimentally and analytically with a specific focus on the influences of corrosion distribution.

1.2 Literature review

1.2.1 Corrosion-induced cracking behavior

Corrosion-induced cracks in concrete propagate and the nearby cracks join together to form a fracture plane that runs through the rebar, causing cover spalling (Li et al. 2007). Hence, the spalling behavior is clearly related to internal crack patterns.

Bazant (1979) suggested that cracking caused by rebar corrosion could occur basically in two different modes, considering that concrete with embedded rebars was a thick-wall cylinder and corrosion products distributed uniformly around rebars. The cracking modes are dependent upon the cover thickness C and the rebar spacing S (see Figure 1.3). If spacing S of the rebars is larger than six times the rebar diameter D and/or the cover thickness C is relatively small, two cracks propagate diagonally from the rebar to the concrete surface at an angle of 45° , which eventually incurs cover spalling. This mode is defined as spalling mode. If the cover thickness is larger than $(S-D)/2$, the two cracks propagate separately to adjacent rebars and form parallel cracks to the concrete surface, resulting in delamination. The crack mode is defined as delamination mode.

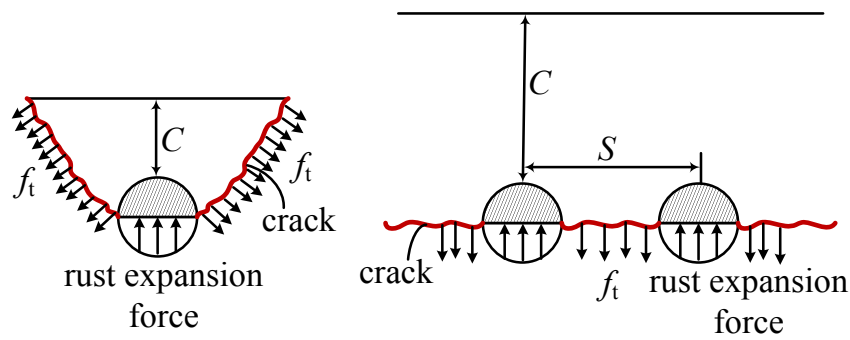


Figure 1.3 Bažant's cracking mode

Tsutsumi et al. (1996) proposed a similar criterion with the ratio of concrete cover thickness to rebar diameter for the internal crack patterns of single-rebar specimens (see Figure 1.4). This criterion is based on the elastic theory that accounts for stress concentration. If k value is less than 3, cracks propagate diagonally to the concrete surface; if k value is greater than 3, cracks develop in the shortest path to the concrete surface, i.e. a vertical crack occurs in the concrete cover along with two horizontal cracks.

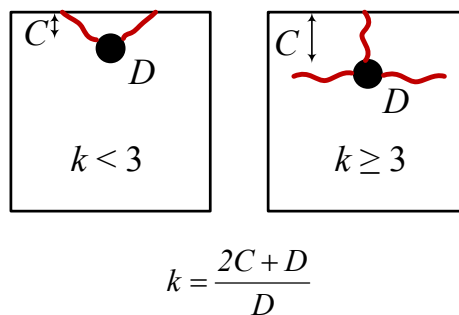


Figure 1.4 Tsutsumi's criterion for internal crack pattern

In an evaluation of the bridge deck survey findings and laboratory research data, Callahan et al. (1970) indicated that corrosion-induced cracks could be either inclined or horizontal in the plane of reinforcement, depending on the cover thickness. The inclined crack may occur when concrete cover is smaller than 25.4mm, while the horizontal crack may occur when the cover thickness is greater than 31.8mm. The experimental studies using electric corrosion method conducted by Caré et al. (2010) and Kawamura

et al. (2010) also show internal crack pattern is strongly influenced by the position of rebar and concrete cover thickness.

The theoretical and experimental studies reported demonstrate that the corrosion-caused internal crack pattern highly depends on the geometry and configuration of the cross section of a concrete member. This finding is based on the assumption that corrosion products distribute invariably along the rebar, which is only two-dimensional cracking behavior. In the case of local corrosion, how cracks propagate and the applicability of the theoretical crack patterns are not clear.

1.2.2 Surface crack width propagation

A great number of experimental studies have been contributed to surface cracking behavior due to rebar corrosion, which are mostly conducted by electric corrosion method that is the employment of anodic current to the rebar. In these studies, a large part was to investigate the cracking time (Rasheeduzzafar et al. 1992, Vu et al. 2005, Caré and Raharinaivo 2007) and a few were extended to surface crack propagation.

Andrade et al. (1993b) and Alonso et al. (1998) analyzed their test results and suggested that surface crack development could be related to rebar radius loss. A radius loss of about 15-50 μm is necessary to generate the first visible crack and in the following propagation crack width is in lineal relationship with radius loss, which may be influenced by cover to rebar diameter ratio and corrosion rate. Caré and Raharinaivo (2007) also reported that visible cracking corresponded at a radius loss of 63 μm . Through measurements of strain on the upper surface of concrete, Nguyen et al. (2006) suggested a similar surface cracking process including two stages generation and propagation. Kawamura et al. (2010) and Tran et al. (2011) investigated the concrete surface deformation during the cracking process using a laser meter. Their results indicated that surface deformation reached a maximum value at the position where crack opened and the distribution of the surface deformation was related to the internal crack pattern. The test carried out by Kawamura et al. (2010) considering effects of various cross-sectional dimensions of specimens demonstrated that surface crack initiated at a corrosion amount of 50mg/cm² that was independent on the section

dimension, while the propagation speed of surface crack for a large side-cover thickness is comparatively small.

These results are valuable for understanding of surface cracking behavior. Most of studies have indicated the effect of cover thickness to rebar diameter ratio and that of water to cement ratio on the surface crack initiation and propagation, whereas the influence of corrosion distribution has not been taken into consideration.

1.2.3 Analysis of concrete cracking caused by rebar corrosion

As for the analytical studies on corrosion-induced cracking, the numerical models are focused herein. Finite element method (FEM) incorporated with either the smeared crack model or the discrete crack model has been widely used to simulate the cracks initiation and propagation. The volume expansion of corrosion products was simulated using nodal displacements (Dagher and Kulendran 1992, Lundgren 2002, Chen and Mahadevan 2008) or by a thermal analogy (Val et al. 2009, Michel et al. 2014). In the early studies, uniform corrosion around a rebar is always assumed (for example, Chen and Mahadevan 2008). However, in the situations of natural corrosion resulting from chloride attack, the corrosion occurs at the rebar surface facing the concrete cover, leading to non-uniform expansion pressure (Yuan and Ji 2009). The effect of non-uniform corrosion on concrete cracking behavior was studied analytically by Du et al. (2006) and Jang & Oh (2010), which generally indicated that non-uniform corrosion might cause faster appearance of cracks in concrete cover than uniform corrosion. Although the numerical techniques for modeling of concrete cracking due to rebar corrosion are developed rapidly in recent years, the studies concerning the effect of local corrosion are not yet sufficient.

On the other hand, the Rigid Body Spring Method (RBSM), a discrete numerical analysis method developed by Kawai (1977), which can simulate well localized damages of concrete, has been used to address corrosion-caused cracking (Tran et al. 2011, Qiao et al. 2014, 2015b and 2015c). The expansion pressure was modeled as an initial strain problem and non-uniform corrosion was taken into consideration. The cracking behavior of concrete specimens with various section dimensions was simulated

reasonably comparing to the test results (Qiao et al. 2014). The RBSM is used in this study to clarify the three-dimensional cracking behavior influenced by local corrosion.

1.2.4 Tensile performance of corroded rebars and evaluation method

A number of experimental studies involving the tensile performance of reinforcements affected by corrosion have been carried out. The corroded rebars used in these studies had been affected by natural corrosion processes, such as the ones removed from real structures (Papadopoulos et al. 2011, Zhang et al. 2012), or by artificial corrosion processes, including the electric method (Almusallam 2001, Cairns et al. 2005, Du et al. 2005, Lee and Cho 2009, Zhang et al. 2012) and salt spray (Apostolopoulos et al. 2007 and 2013, Lee and Cho 2009, Papadopoulos et al. 2007 and 2011). In spite of the different corrosion methods, the various studies have similarly demonstrated that corrosion may decrease yield and ultimate tensile strengths, and significantly reduce ultimate strain or elongation. By applying regression analysis to the experimental results, some empirical correlations with average corrosion degree η (%) have been proposed to estimate the residual tensile capacity F from that of non-corroded rebars F_0 . These empirical relationships all have a similar form (Du et al. 2005, Lee and Cho 2009, Zhang et al. 2012):

$$F = (1.0 - \alpha \cdot \eta) F_0 \quad (1.1)$$

Coefficient α is determined from test data and may change with the corrosion method and rebar type. In a similar way, Cairns et al. (2005) recommended that empirical equations based on the average section loss are suitable for evaluating residual strength and ductility.

Using these empirical equations, satisfactory agreement with test results can be obtained if coefficient α is appropriately chosen. Lee and Cho (2009) introduced empirical equations into a material constitutive law for reinforcement and suggested that it is possible to numerically analyze the strength of RC structures containing corroded reinforcement with this constitutive law. Dekoster et al. (2003) and Kallias & Rafiq (2010) have adopted these empirical equations in a rebar material model to investigate the flexural behavior of corroded RC beams using the FEM.

Although the applicability of the empirical equations has been confirmed, there is variability in the recommended values of coefficient α . This might result from the varied corrosion states produced by different corrosion methods. The electric method yields a more uniform corrosion while the natural corrosion process is more localized. Comparing these different corrosion states, Zhang et al. (2012) indicated that natural corrosion could have a greater impact on tensile degradation than corrosion caused by the electric method due to the greater cross-sectional loss at certain locations. Moreover, the coefficients needed to evaluate yield and ultimate strengths as well as elongation may also differ, which makes the selection for a numerical model difficult. A better option may be using corrosion topography or profile, which can account for the effect of local corrosion (Cairns et al. 2005, Qiao et al. 2015a).

1.3 Study objective and research significance

For the design of new RC structures, current design standards or regulations stipulate some specific requirements to prevent or to delay corrosion of reinforcements, whereas they are absent for a large number of existing structures. Hence, the existing structures may be seriously damaged by rebar corrosion, especially those exposed to chloride-laden environments. In order to prolong the service life of the affected structures, it is necessary to evaluate the corrosion-caused damage level and conduct efficient maintenance works, which require a full understanding of the influences of corrosion on RC structures. However, as referenced earlier, the work on this topic is still insufficient.

Therefore, one objective of this study is to clarify the corrosion-caused damages in three-dimensional level, where crack propagation and cover spalling, as well as tensile performance of corroded rebars influenced by corrosion distribution are investigated thoroughly. Another objective is to develop the corrosion-expansion model based on the RBSM (Tran et al, 2011) to a time-dependent electro-mechanical model for the combined analysis of concrete cracking and tensile degradation of rebars due to corrosion.

This study is contributable to a better understanding of the factors affecting the development of corrosion-induced cracks, including internal crack patterns and surface crack width. Moreover, the behavior of cracking and cover spalling resulting from local corrosion is elucidated. The proposed evaluation method for the tensile behavior of corroded rebars can accurately estimate the residual tensile capacity. It is integrated into the electro-mechanical model, which also offers good prediction of the electric corrosion process of rebars and associated crack development. The model newly developed is a solid step towards a reliable means of assessing corrosion-caused damages of RC structures.

1.4 Organization of dissertation contents

The flow of this dissertation is shown in Figure 1.5. The dissertation generally consists of two parts. The first part is related to concrete cracking behavior due to rebar corrosion. Both two-dimensional (2D) and three-dimensional (3D) cracking behavior is examined using an electric corrosion method that can simulate natural corrosion pattern. Meantime, the corrosion-expansion model is applied in the analysis to study the cracking mechanism. The second part investigates tensile performance of corroded rebars, in which a numerical model is developed to evaluate the tensile behavior and verified by comparisons to the test data. In the end, the electro-mechanical model for the combined analysis is proposed. The contents of this dissertation are briefly explained as follows.

Chapter 1 is the introduction part, including a general background of the study, a review of related references, the study objectives and the organization of the dissertation.

In Chapter 2, an electric corrosion method using a salt-water pool on the concrete cover is introduced, which can approximate the natural corrosion state of a rebar due to chloride attack. The electric corrosion process implemented by this method is investigated in terms of corrosion degree and corrosion profile that is represented by radius losses along the rebar. The interaction between electric corrosion and cracks is explained. A simple test method is also proposed for simulating various corrosion profiles in which bare rebar specimens and different cathode arrangements are used.

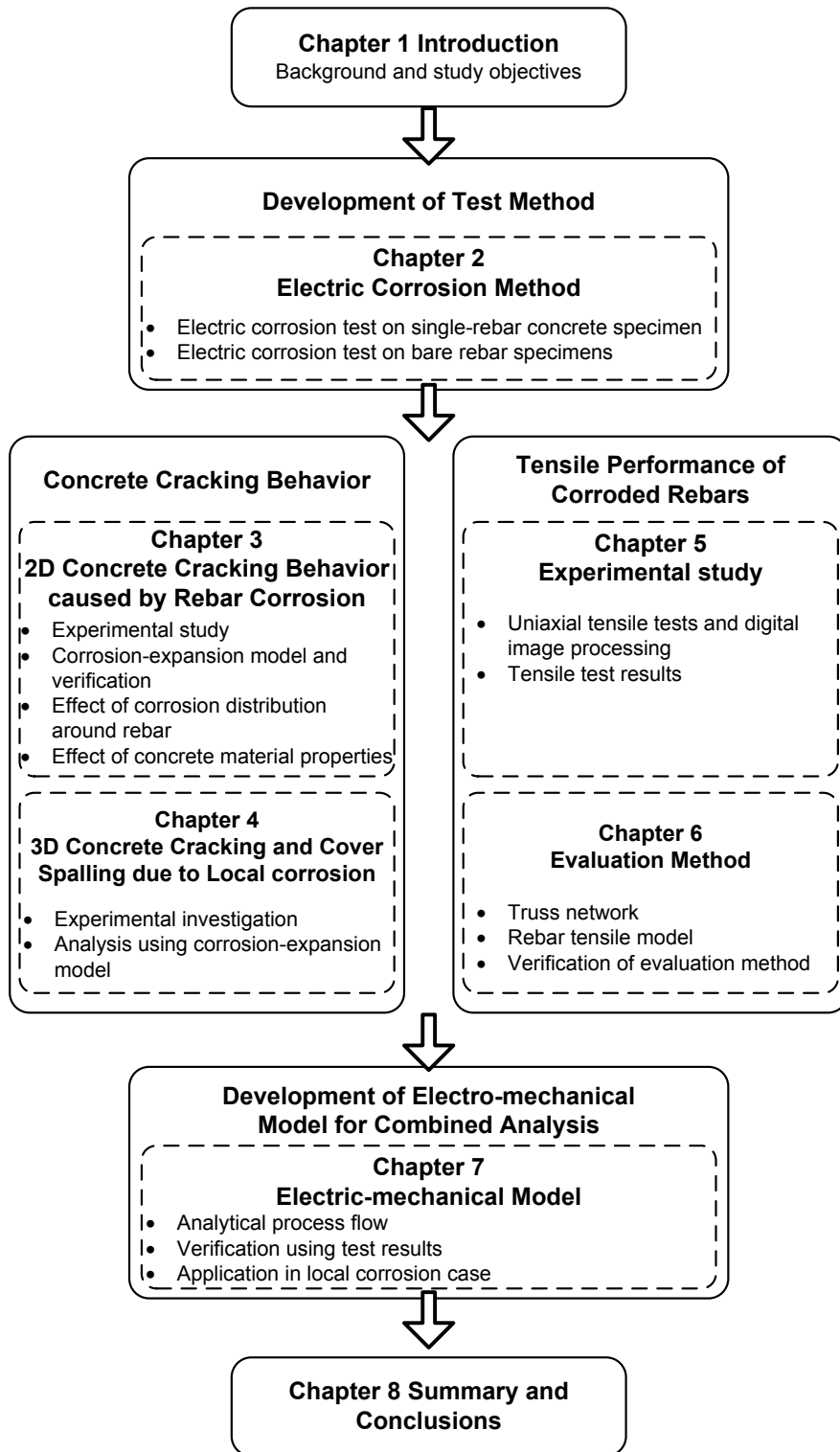


Figure 1.5 Organization of the dissertation

Chapter 3 presents an investigation of 2D cracking behavior, which is studied both experimentally and analytically. In the experiments, the single-rebar specimens with different cover thicknesses were tested using the proposed electric corrosion method and the crack patterns were observed. In the analysis, the corrosion-expansion model was used to simulate the cracking behavior in comparison to the test results, where a non-uniform corrosion model was assumed. The parametric studies with regard to the effects of corrosion distribution around a rebar and concrete material properties are carried out respectively to clarify the influencing factors of crack initiation and propagation.

In Chapter 4, the 3D crack propagation caused by local corrosion along the rebar is studied compared with the 2D cracking behavior. The local corrosion state, i.e. corrosion concentrates at the center part of the rebar, was simulated using salt-water pools of various sizes in the experiments. The resulting crack patterns and the relation to the cover spalling were examined. In addition, the corrosion-expansion model was applied to simulate the crack propagation and to predict spalling area by assuming similar distributions of corrosion amounts along the rebar to the test results. The 3D cracking mechanism is discussed in the analysis.

Chapter 5 shows an experimental study on the tensile behavior of rebars corroded with various corrosion profiles. Both bare rebar specimens and those corroded in concrete are considered. A digital image processing method was employed to obtain the strain distribution along a test specimen when the tensile load was applied. The applicability of some empirical equations is checked with the test results.

In Chapter 6, a quantitative evaluation method for the tensile performance of corroded rebars is proposed in consideration of corrosion profile. This model is implemented using the RBSM incorporated with a truss network and verified with the test results of bare rebar specimens.

In Chapter 7 The corrosion-expansion model and the model for evaluating tensile behavior of corroded rebars are combined to build a time-dependent electro-mechanical model for RC members. The applicability of the newly developed model is confirmed by comparing the simulated corrosion degree, radius losses along the rebar, concrete crack patterns and the residual tensile performance to the test results. The model is also applied on the local corrosion cases to analyze the cracking process.

Lastly, Chapter 8 includes the conclusions derived from the study and recommendations for future research.

2 Development of Electric Corrosion Method for Controlled Corrosion Profile

2.1 Introduction

Natural corrosion of a rebar embedded in concrete is a slow process, since it may take several years for chloride ions penetrating through concrete cover. For the evaluation of structural behavior of corroded RC members, researchers thus employ several accelerating corrosion techniques to obtain the desired corrosion damage in a reasonably short time. Adding chlorides into a concrete mix (Treadaway et al. 1989, Liu and Weyers 1998), the impressed current method (Grimes et al. 1979, Caré and Raharinaivo 2007) that is applying an external direct electric current to the rebar, or a combination of the two methods (Andrade et al. 1993b, Yuan et al. 2007) are widely used to accelerate the corrosion process. However, the typical corrosion pattern implemented by the above methods is uniform corrosion around the rebar (Yuan et al. 2007, Poursaee and Hansson 2009). It is different from the natural corrosion state resulting from chloride attack. Yuan and Ji (2009) observed the distribution of corrosion products around the rebars that were obtained by exposing the RC specimens to an artificial climate environment. The test results indicated that the corrosion products distributed on the half circumference of the rebar facing the concrete cover only (see Figure 2.1).

In order to better represent the natural chloride-induced corrosion pattern, an electric corrosion method using a salt-water pool on the concrete cover is introduced for the experimental study. A basic study for the investigation of the electric corrosion process by this method, including corrosion degree and radius losses along the rebar surface, is carried out. A simple method for simulating various corrosion profiles using

bare rebar specimens and different cathode arrangements is also proposed, which is a basis for implementing local corrosion on RC specimens and also prepares the test samples for the study of tensile performance of corroded rebars.

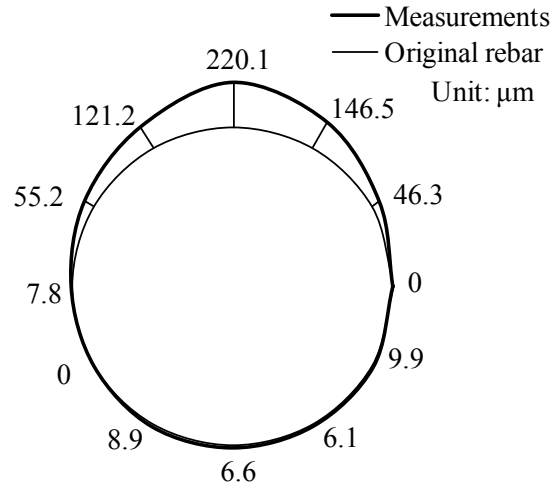


Figure 2.1 Distribution of corrosion products layer (Yuan & Ji, 2009)

2.2 Electric corrosion test on single-rebar concrete specimens

2.2.1 Test setup and procedure

The test setup of a traditional electric corrosion method that prevails in the studies of corrosion related problems (Yuan et al. 2007, Val et al. 2009, and Caré et al. 2010) is explained in Figure 2.2. Normally the test specimen is immersed in sodium chloride (NaCl) solution and applied with direct current to accelerate the corrosion process, although the level of salt water or the applied current density may be varied. An attempt to study corrosion-induced cracking behavior had been made using this method and the resulting internal crack pattern was observed (see Figure 2.3). As can be seen, an inside crack under the rebar occurred, suggesting that the rebar was uniformly corroded and the expansion pressure acted in all direction around the rebar. The objective of this study is on the basis of the corrosion resulting from chloride ions that is non-uniform corrosion around the rebar. Hence a different test method should be developed.

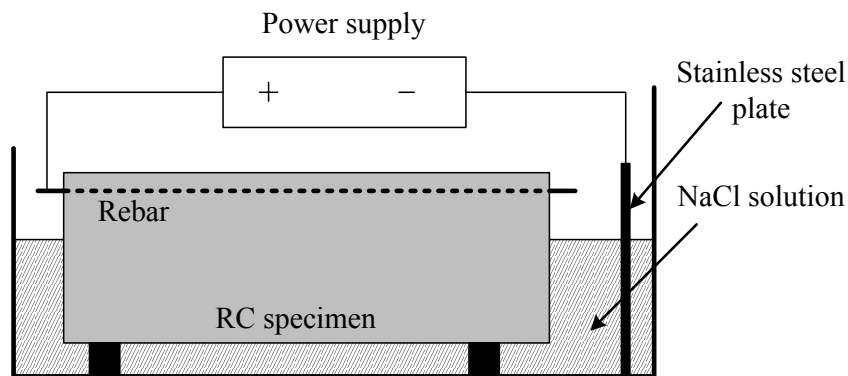


Figure 2.2 Classic electric corrosion method

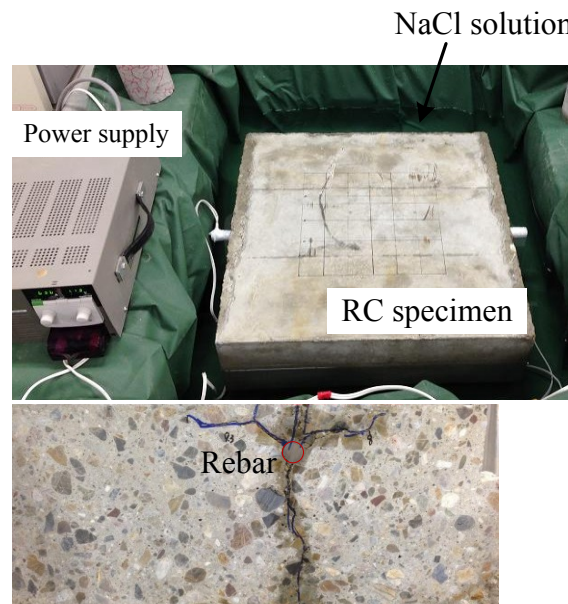


Figure 2.3 Test of single-rebar specimen using classic method

Poursaee & Hansson (2009) and Malumbel et al. (2012) recommend that only selected faces of concrete members should be contaminated with chlorides, similar to the practical situations. In current test, a 100mm wide water pool filled with 3% NaCl solution was set on the top surface of each specimen, right above the rebar. A copper plate was placed in the water pool as the cathode. Figure 2.4 shows a diagram of the electric corrosion test. It is presumed that the corrosion current for the rebar upper part facing the concrete cover would be greater than that for the lower part, attributable to the smaller distance from the upper part to the cathode. On the other hand, the cracks generated in the concrete cover can cause faster chloride ingress (Djerbi et al. 2008),

increasing the corrosion rate of the upper part. Therefore, the corrosion pattern around the rebar can be expected to be non-uniform, i.e. the half circumference facing the concrete cover is more corroded. Moreover, the distribution of corrosion along the rebar can be controlled with salt-water pools of various lengths, which is to be discussed in Chapter 4.

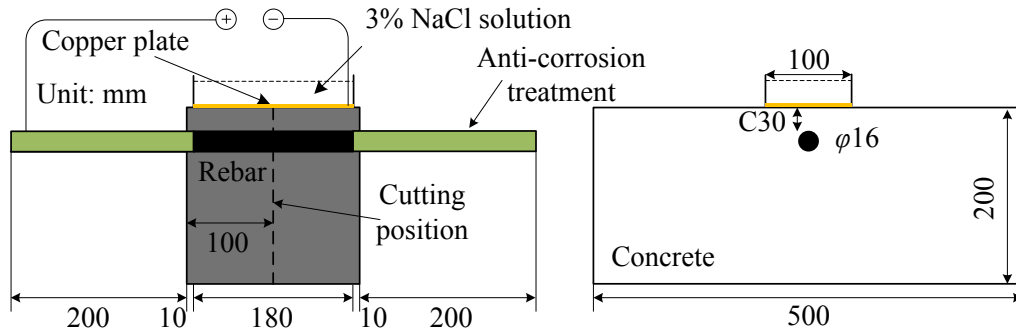


Figure 2.4 Diagram of electric corrosion test

The internal crack pattern is largely influenced by the geometry and configuration of the cross section of a concrete specimen, for instance side-cover thickness and adjacent rebars (Kawamura et al. 2010). In order to remove these effects, a cross-sectional dimension of 500mm×200mm was used in the experimental study (see Figure 2.4). In each concrete specimen having a length of 200mm, a 600mm long round rebar SR235 (JIS 2010) with a diameter of 16mm was partly embedded at a depth of 30mm and the rebar extended 200mm beyond the specimen at each end. Round rebars were used for easily measuring radius loss by a laser meter. It is considered that round and deformed rebars can produce similar cracking behavior, as radial expansion pressure would be similar for both types of rebar (Mullard and Stewart 2011). The laser meter has a limited scanning length of 200mm. Hence the length of the rebar part exposed to corrosion was confined to 180mm by coating the other parts with anti-corrosion paint, waterproof tape and insulating tape in sequence to prevent from corrosion. The rebars were used directly as received, i.e. the mill scale of the area studied was left intact. Before casting the concrete, the rebar samples with anti-corrosion covers were weighted for the initial weight.

A total of 20 specimens were made with High Early Strength Portland Cement. Table 2.1 shows the mixture proportions of concrete used to cast the specimens, which was always applied in the experimental study. The maximum diameter of coarse aggregate used was 20mm and the volume fraction of coarse aggregate to total aggregate was 0.6. After casting, the specimens were cured in a room at 20°C for 14 days and then the electric corrosion test was conducted. Prior to the test, the concrete elastic modulus, compressive strength and splitting tensile strength were determined as 30.75GPa, 38.45MPa and 2.94MPa respectively.

Table 2.1 Mixture proportions of concrete

W/C(%)	s/a(%)	Unit (kg/m ³)				
		Water	Cement	Sand	Aggregate	AE (liter/m ³)
56.5	44	166	294	779	990	1.18

The testing time was varied as shown in Table 2.2 to obtain different concrete cracking situations. Specimens were named in the form T86, meaning a time of approximately 86hours applied with direct current. Four specimens were used for each test series and connected in series to a DC power, by which a constant current was supplied (see Figure 2.5). The nominal current density applied in the test was about 900 μ A/cm² (a current intensity of 0.08A for ϕ 16 rebar), which was greater than the maximum corrosion rate recorded in the real corrosion case (100 μ A/cm² as indicated by Andrade et al. (1993b)). Although current density may affect the evolution rate of surface crack width (Alonso et al. 1998, El Maaddawy & Soudki 2003), there are no conclusive findings regarding the effects on crack pattern. Hence, a large current density was used to allow quick cracks generation, as referred to in other reported electric corrosion tests (Mangat & Elgarf 1999, Yuan et al. 2007).

Table 2.2 Test series on single-rebar specimens

Series	Testing time (hours)	Current flow (A*hr)
T86, T205, T341, T500, T625	86.18, 204.53, 340.89, 500, 625	6.89, 16.36, 27.27, 40, 50



Figure 2.5 Electric corrosion test using salt-water pool

One of the four specimens for each test series was cut after the corrosion test for observing internal crack pattern. The other three specimens were broken and the rebars embedded were collected and cleaned by immersing them in 10% ammonium citrate solution for 24 hours and then using a steel brush to remove corrosion products. The mass loss Δm (g) of each rebar sample measured as the difference between the initial weight and the remaining weight was used to determine the corrosion degree η over the whole corroded area with a length of l_c and the current efficiency N :

$$\eta = \frac{\Delta m}{l_c m_u} \quad (2.1)$$

$$N = \Delta m / \left(\frac{ItM}{nF} \right) \quad (2.2)$$

Where m_u is the unit mass (1.58g/mm), l_c is the corroded length (180mm), I is the current intensity (0.08A), t is the testing time (s), M is the molar mass of iron (55.85g/mol), n is the valency (2), and F is Faraday's constant (9.65×10^4 C/mol).

The corrosion profiles of corroded specimens were measured using a laser meter with a precision of $0.1\mu\text{m}$ afterwards. Various measurement lines located at twelve different circumferential positions around the corroded specimens were tested, which had an interval of 30° (see Figure 2.6). The top line is the nearest side to the concrete surface. Along the test line the measurement interval was $50\mu\text{m}$. The non-corroded parts at the sides of the corroded area with a length of 10mm were used as reference levels, using which the measured values were transformed into relative heights. Each corroded specimen was measured before the corrosion test to obtain the initial level. The

difference between the initial level and the measured level after the corrosion test was treated as the radius loss. Meanwhile, a Fast Fourier Transform was performed to remove the influences of imperceptible vibrations during the measurements and then an Inverse Fourier Transform was conducted to obtain radius loss. Microwaves with frequencies of more than five wave periods in each 10mm of length were removed (Mada, 2000).

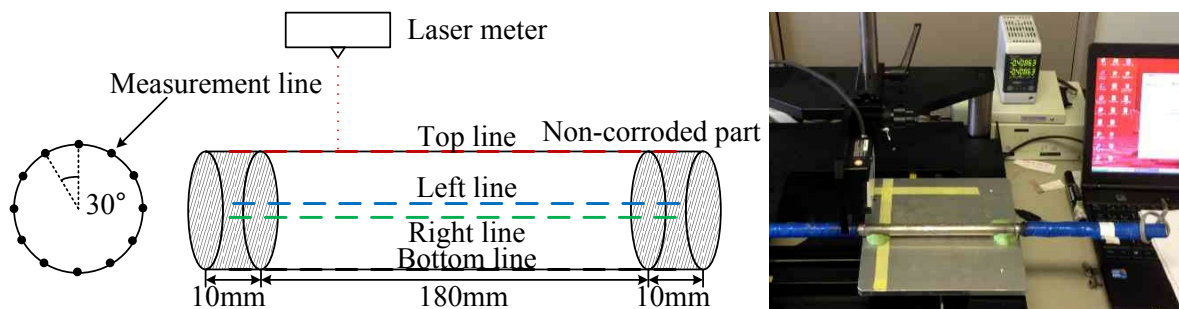


Figure 2.6 Measuring corrosion profiles by laser meter

2.2.2 Corrosion degree and profile

Figure 2.7 shows the development of corrosion degree against accumulated current flow, in which the corresponding current efficiencies are also indicated. The practical corrosion degrees η by the electric corrosion method applied are within a range from 0.65% to 6.83% when the testing time is from 86.18 to 625 hours. They are much smaller than those estimated based on Faraday's law (see $N=1$ in Figure 2.7) due to the occurrence of a reaction competitive with oxidation of rebar, probably the split of water to oxygen and hydrogen. During the corrosion test, it was noticed that some gases bubbled out of the water pool, which were considered to be oxygen and hydrogen. As the testing time increases, the current efficiency slightly increases, implying a rise of corrosion rate. Nossoni and Harichandran (2012) suggested that the current efficiency of the electric corrosion test increases when the chloride concentration in the concrete is increased. Therefore, the rise of corrosion rate may be caused by the ingress of chloride ions into the concrete.

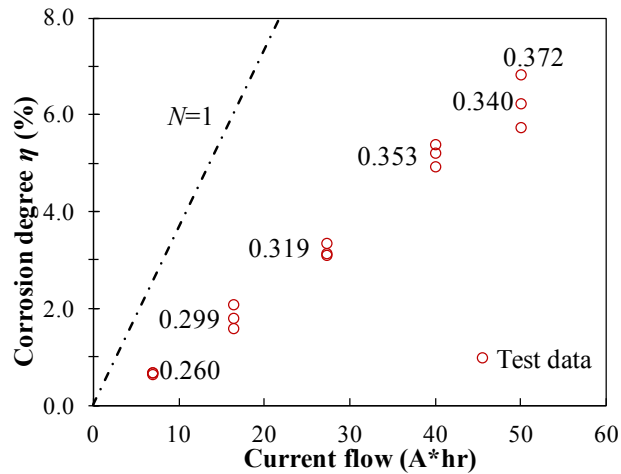


Figure 2.7 Measured corrosion degree

In order to clarify the corrosion pattern of corroded specimens, the measured radius losses along the top and bottom lines are compared in Figure 2.8. With an increase of corrosion degree, the radius losses along the top line have an obvious development, while the radius losses along the bottom line hardly increase. It indicates that the applied electric corrosion method results in a non-uniform corrosion in the circumferential direction. On the other hand, the radius losses are similar along the rebar length direction when the corrosion degree is small (testing time not exceeding 341 hours). For the series of T500 and T625, the radius losses at two ends of the corroded area are greater than those at the center part. During the corrosion test a certain amount of corrosion products exuded from the sides of the concrete specimens, i.e. the sides from which the rebars extended. It may promote the corrosion rates at the ends of the corroded area.

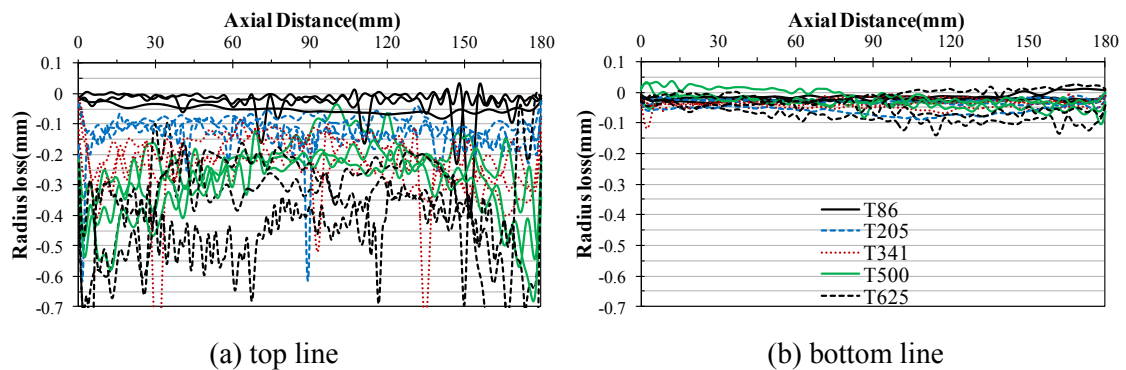


Figure 2.8 Measured radius losses along rebar

The average value for each measurement line was obtained to demonstrate the typical corrosion pattern around the rebar (see Figure 2.9). The ratio of the average radius loss at the top quarter side RL_U to that at the bottom side RL_D is shown in Figure 2.10. It is clear that the difference of the radius loss between the upper and the lower circumferences enlarges as the corrosion develops. This tendency may be attributed to the cracks appearing in the concrete, which accelerates the chloride transport and thereby increases the corrosion rate for the part near cracks.

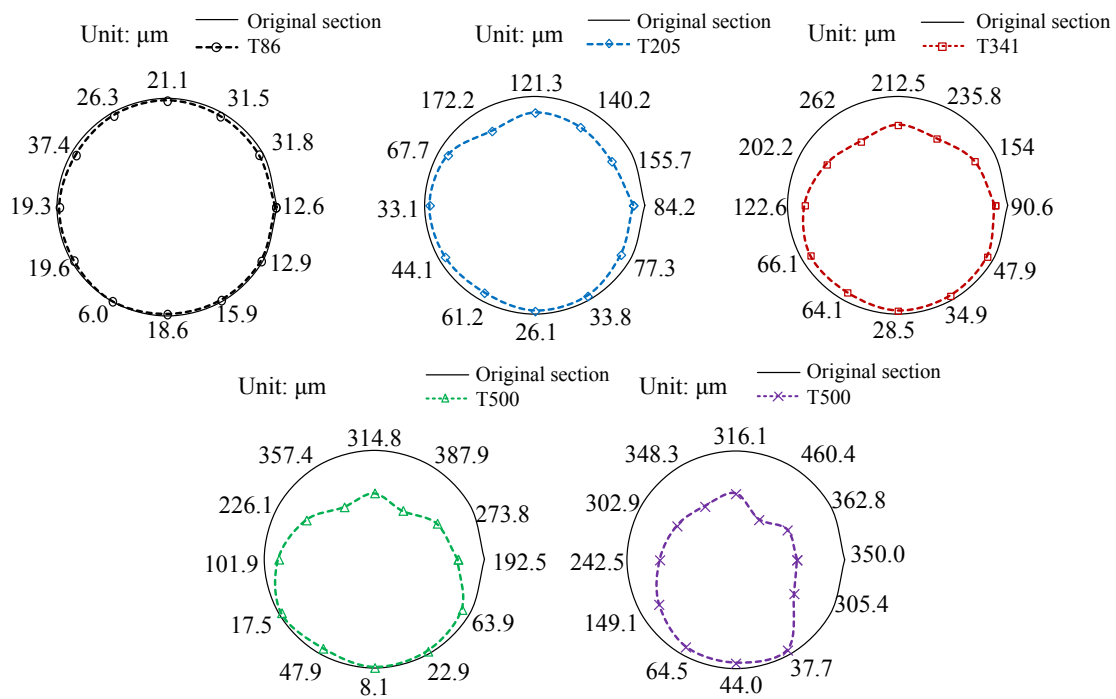


Figure 2.9 Rebar cross section after corrosion

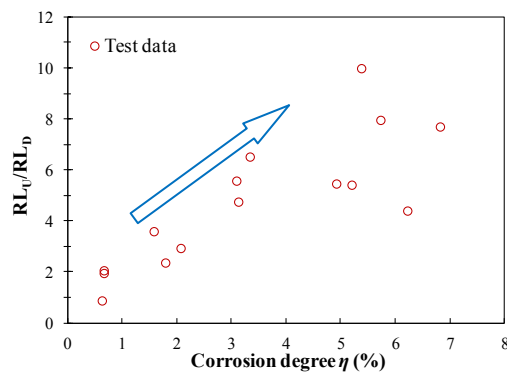


Figure 2.10 Ratio of radius losses between top and bottom sides

Unlike the classic electric corrosion method in which specimen is immersed in salt solutions or chloride is added to the concrete mix, the method applied herein uses a salt-water pool on the concrete cover, which makes the chloride transport unidirectional. The corrosion pattern implemented is similar to that observed from the specimens corroded under an artificial climate environment (see Figure 2.1). Thereby, this method is considered to be a better one for the reproduction of the corrosion occurring under practical chloride-contaminated conditions within a relatively short time.

2.2.3 Concrete crack pattern

Figure 2.11 shows internal crack patterns of the specimens under different corrosion amounts, which were observed at the cutting position as shown in Figure 2.4.

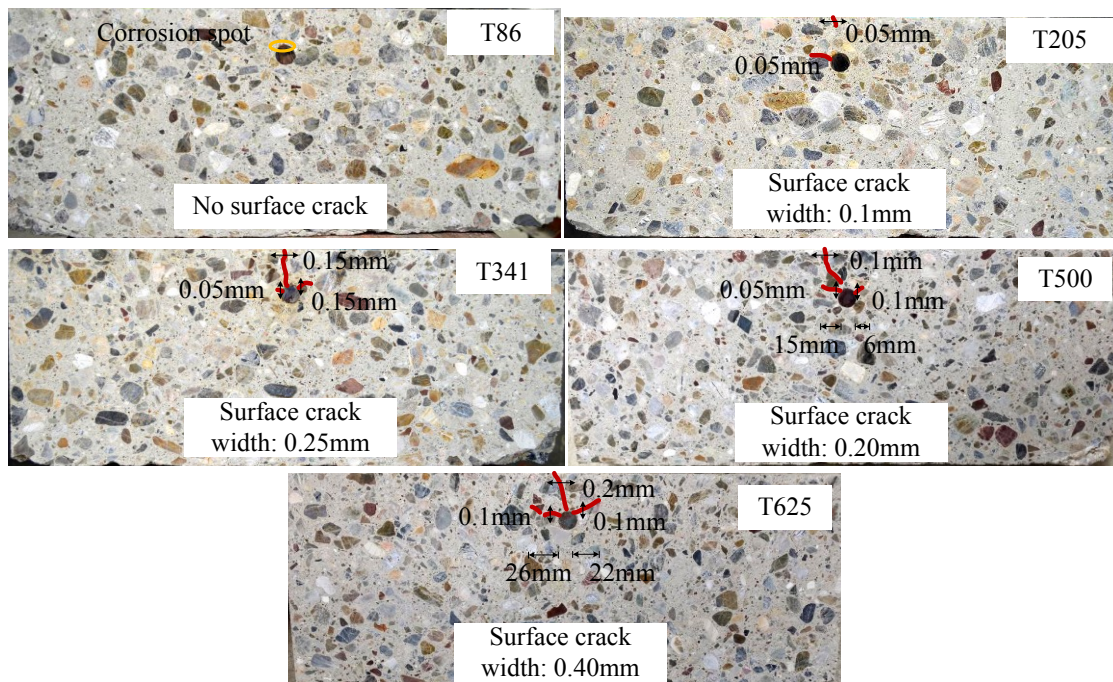


Figure 2.11 Internal crack patterns under various corrosion amounts

A visible vertical crack initiates from the concrete surface. As corrosion amount increases, the surface crack becomes wider and the vertical crack propagates to the rebar along with the appearance of lateral cracks. The developed vertical crack provides a flow channel for chloride ions and further increases the corrosion rate of the rebar upper

part (see Figure 2.9), suggesting that the corrosion rates at various positions around the rebar may be in a relation with the crack width nearby.

2.3 Electric corrosion test on bare rebar specimens using different cathode arrangements

2.3.1 Experimental program

In the experimental study, a simple and fast method of simulating various corrosion profiles along the rebar, such as local corrosion, is desired for the study of mechanical properties of corroded rebars. To achieve this goal, the corroded rebar specimens were prepared through an accelerated corrosion process, in which they were straightly exposed to salty water and subjected to a direct current. In reported experimental investigations, corrosion tests of bare rebars have been performed by exposing the specimens to the natural atmosphere (Allam et al. 1994, Maslehuddin et al. 1990) or immersing them in a stainless steel tube filled with salty water and connected to a direct current (Du et al. 2005). The radius losses of the corroded specimens prepared by these two methods varied irregularly along the rebar length, which causes difficulty in clarifying the effects of different corrosion states and also in numerical model validation. Hence, different cathode arrangements were used in this study to obtain various and comparable corrosion profiles.

The experimental unit is illustrated Figure 2.12. To build each unit, one 600mm long round rebar with the same type as those used in the previous study on RC specimens was partly embedded in a 250mm long PVC pipe. The rebar extended 175mm beyond the pipe at each end. The pipe, with an inner diameter of 68mm, was fully filled with 3% NaCl solution. For the measurement of radius losses along the rebar specimens, they were initially treated in the same way as those in the former study, i.e. the length of the corroded part was 180mm and the left parts were covered with anti-corrosion treatments. However, the mill scale of the part exposed to corrosion was carefully removed using a grinder before corrosion testing in order to implement micro-cell corrosion.

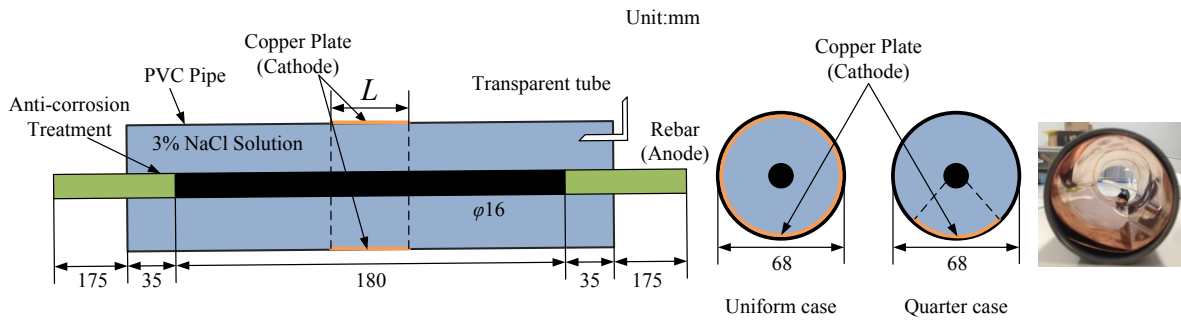


Figure 2.12 Diagram of one experimental unit using bare rebar

The feature of the method applied is a varied arrangement of cathode. In the experiment, a complete or only one-quarter tubular copper plate was placed around the rebar as the cathode. The cathode varied in length to simulate different corrosion profiles. It is presumed that the varying distance from a point on the rebar surface to the cathode would lead to different corrosion currents at various points on the rebar surface. More distant points would be subjected to lower corrosion currents, so corrosion should be concentrated at the center part of the rebar. The measured radius losses along the rebar specimens after the corrosion tests proved this point. A tube was used in the experimental device to assist in the transfer of gases generated by the cathode reaction. The hydrogen embrittlement effect on the mechanical properties of rebars is ignored in this experiment, since the tested rebars (SR235), which have an ultimate strength of less than 1000MPa, are not generally considered susceptible (Kirby 1996) and the test results show no appreciable effect either.

Table 2.3 presents a list of test variables. A range of average corrosion degrees over the test area from 3% to 15% was considered. Specimens were named in the form U10-3%, which means a uniform case with a cathode length of 10mm and an objective average corrosion degree of 3% over 180mm test area. Three specimens were used for each test series. To ensure the same objective corrosion degree, all units were connected in series to the DC power and then supplied with a constant current (see Figure 2.13). Various degrees of corrosion can be achieved by supplying current for different times based on Faraday's law. The current density was $1.0\text{mA}/\text{cm}^2$ as referred to in other reported studies (Andrade et al. 1991, Du et al. 2005).

Table 2.3 Test variables for corrosion test using bare rebars

	Series	Length of cathode (mm)	Objective average corrosion degree (Current flow, A*hr)
Uniform case	U180, U100, U40, U10	180, 100, 40, 10	3% (8.2), 9% (24.7), 15% (41.2)
Quarter case	Q180, Q10	250, 10	9% (24.7)



Figure 2.13 Preparation of corroded rebar specimens by electric corrosion method

After the designed corrosion testing time, the corroded specimens were cleaned with 10% ammonium hydrogen citrate and then weighted to obtain the mass loss Δm . The corrosion degree η was determined using the equation (2.1). The corrosion profiles of corroded specimens were measured using the laser meter. Four measurement lines, including the top, bottom, left and right lines were tested (see Figure 2.6). The radius loss was also obtained as the difference between the measurement levels before and after the corrosion test.

2.3.2 Corrosion degree and profile

Figure 2.14 presents the measured corrosion degree. Since the rebar specimens were directly exposed to salt water, the actual corrosion degree follows Faraday's law accurately, showing that the current efficiency nearly equals 1.

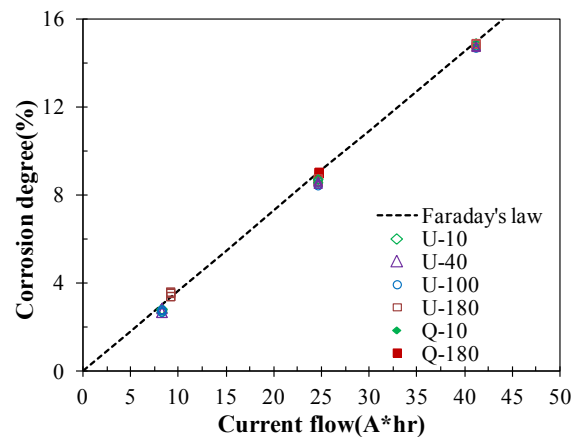
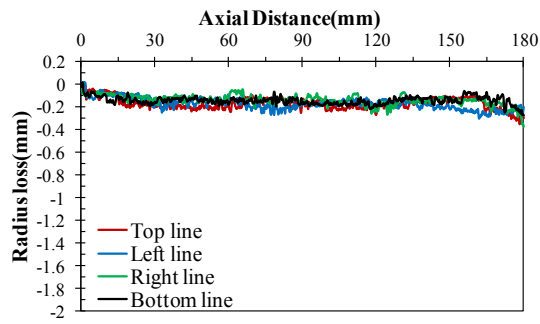


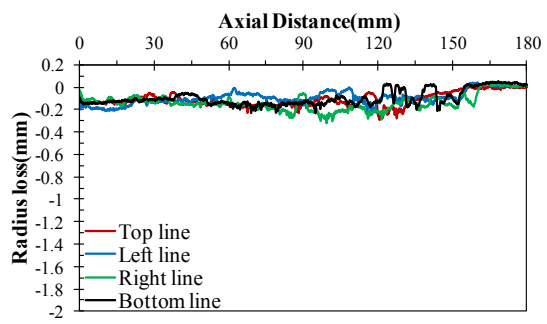
Figure 2.14 Measured corrosion degree in the test with bare rebars

Figure 2.15 and Figure 2.16 show the measured loss of radius along the corroded part for the uniform cases with corrosion degrees of 3% and 9% respectively. Most of the specimens show that the radius losses along the four measurement lines are similar, indicating that the specimens are uniformly corroded in the circumferential direction. Comparing the series with different cathode lengths, it can be found that the corrosion profiles of the U180 series are linear, while in the U10 series the radius loss at the center is about 3-4 times that at the ends of the corroded part. Hence, the use of a small cathode in the electric method concentrates the corrosion in the center to a certain extent, which can simulate local corrosion along the rebar length.

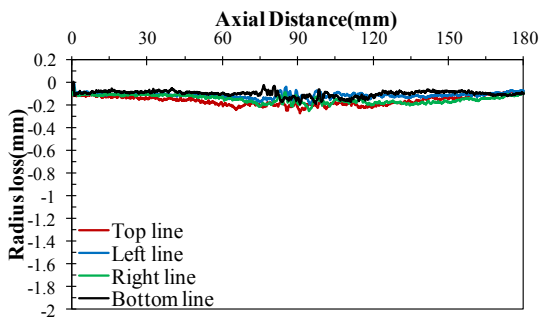
When the corrosion degree reaches 15%, the corrosion profiles become asymmetrical, i.e. one end is more corroded than the other end (see Figure 2.17). During the corrosion tests, it was noticed that some corrosion products adhered to the specimen surface as shown in Figure 2.18, a phenomenon only found in the cases with 15% corrosion. These adhered corrosion products may affect the distribution of corrosion current along the specimen surface and result in the asymmetrical corrosion profile. Related effects on the corrosion process will be discussed in Chapter 6.



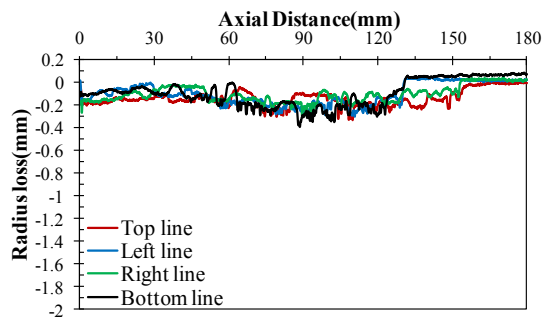
(a) U180-3%



(b) U100-3%

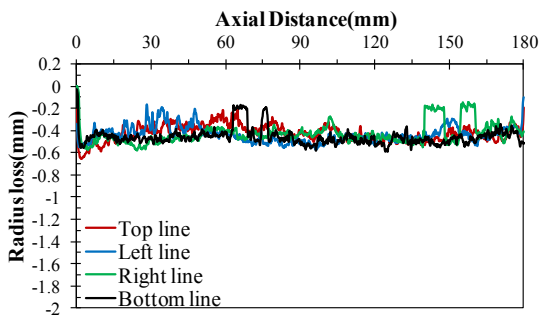


(c) U40-3%

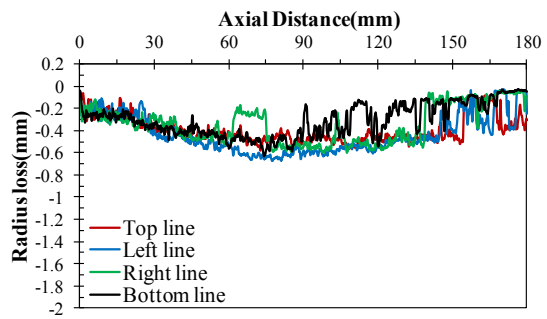


(d) U10-3%

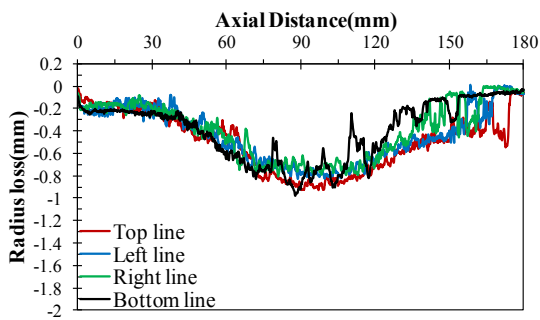
Figure 2.15 Corrosion profiles for uniform cases (3% corrosion)



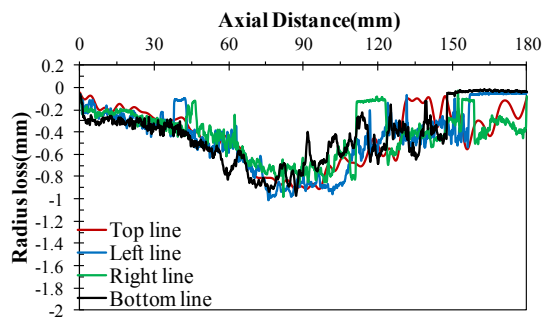
(a) U180-9%



(b) U100-9%



(c) U40-9%



(d) U10-9%

Figure 2.16 Corrosion profiles for uniform cases (9% corrosion)

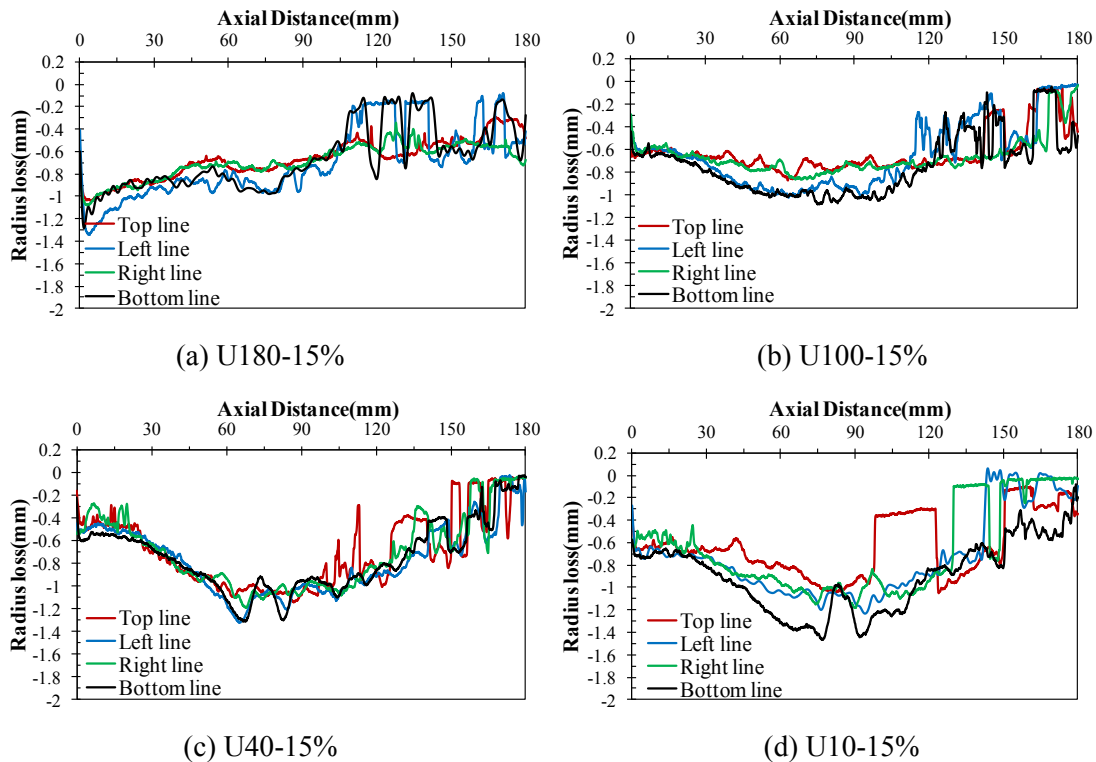


Figure 2.17 Corrosion profiles for uniform cases (15% corrosion)



Figure 2.18 Experimental observation (corrosion products adhered to rebar surface)

Corrosion profiles of the quarter cases are shown in Figure 2.19, where circumferential non-uniform corrosion can be confirmed. The radius loss along the bottom line, which is closer to the cathode, is evidently larger than those along other measurement lines. Radius losses along the left and right lines are almost the same due to their symmetric location away from the cathode, while the top line shows the least

loss since the distance from the cathode is the largest. To some extent, the corrosion pattern demonstrated in the series of Q180 approximates that observed in the tests of RC specimens. They are used to investigate the effect of various circumferential corrosion states on the tensile behavior of corroded rebars.

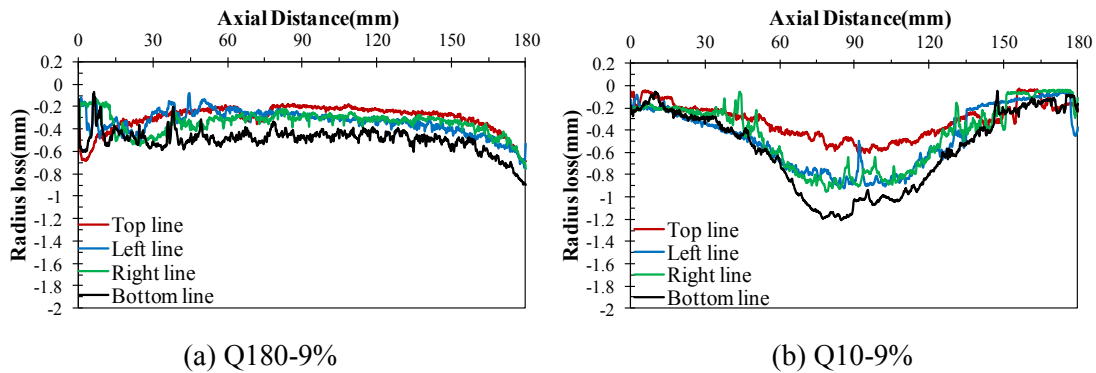


Figure 2.19 Corrosion profiles for quarter cases

2.4 Summary and conclusions

The electric corrosion method using a salt-water pool on the concrete cover is proposed to simulate the natural corrosion pattern caused by chloride attack. The measured radius losses along the rebar surface under different corrosion amounts demonstrate that the circumference facing the concrete cover is more corroded, which is similar to that observed under artificial climate environment. It is also found that the cracks generated in the concrete cover may enlarge the difference of corrosion rates between various positions around the rebar. Since the structural behavior of RC members exposed to chloride-induced corrosion is focused on the study rather than the electrochemistry of corrosion, this method is applicable. But we should bear in mind that the electrochemistry involved and the type of corrosion products formed in electric corrosion test are different from those in natural corrosion.

The test results show a relatively low but increasing current efficiency with time, which is probably caused by the mutual effect between electric corrosion and cracking. It makes the control of corrosion process as well as cracking condition difficult and

Faraday's law may be inappropriate to predict the corrosion extent. Hence a model that can analyze the electric corrosion process and related crack propagation is required.

On the other hand, the experiment on bare rebar specimens is carried out to obtain different corrosion states along the rebar, which confirms that the method with various cathode arrangements is capable of simulating various corrosion profiles around or along the rebar. The use of a small cathode concentrates the resulting corrosion to a certain extent, suggesting local corrosion in an RC specimen can be achieved by using a small salt-water pool with a length less than that of the rebar.

3 Evaluation of 2D Concrete Cracking caused by Rebar Corrosion

3.1 Introduction

Corrosion-induced damage of RC structures is usually demonstrated in the form of concrete cracking and spalling. The concrete cracking may not result in a significant loss of the structural strength of RC members (Andrade et al. 1993b, Li 2003), whereas it raises a risk to human safety by concrete falling. Therefore, there is a need for the study of concrete cracking behavior caused by corrosion of reinforcements, especially the propagation of internal cracks that is related to cover spalling.

In this chapter, the 2D cracking behavior is discussed. Many researches concerning concrete cracking due to corrosion have been done on the basis of behavior in the plane of reinforcement, which have been studied both experimentally (Alonso et al. 1998, Caré et al. 2010) and analytically (Lundgren 2002, Michel et al. 2014). In these studies, crack initiation is mainly focused. With regard to the development of cracks, although the theoretical models (Bažant 1979, Tsutsumi et al. 1996) have been proposed, they are based on an assumption of uniform corrosion around the rebar, which is different from the practical corrosion state caused by chloride ions. Hence, the electric corrosion method introduced previously, which can simulate the natural corrosion pattern, is used to examine 2D crack propagation. Different cover thicknesses as 10 and 30mm are considered.

In the meantime, the corrosion-expansion model (Tran et al. 2011) that takes into consideration circumferentially non-uniform corrosion is used to simulate the cracking process. The simulated internal crack patterns are compared with those observed in the test. Parametric studies concerning the effects of corrosion distribution

around the rebar and concrete material properties are also carried out to clarify the influencing factors of crack initiation and propagation.

3.2 Experimental setup

In the experiment, a type of single-rebar slab specimens was used, which had the same cross-sectional dimension as those in the basic study but an extended length to 600mm (see Figure 3.1). A 550mm long deformed rebar SD345 (JIS 2010) with a diameter of 19mm was completely embedded in each specimen. In order to account for the effect of cover thickness, two specimens having different concrete cover depths of 10 and 30mm were investigated. According to the crack criterion by Tsutsumi et al. (1996), the k values are 2.05 and 4.16 for the two specimens respectively. Therefore, the two different crack patterns as shown in Figure 1.4 can be expected.

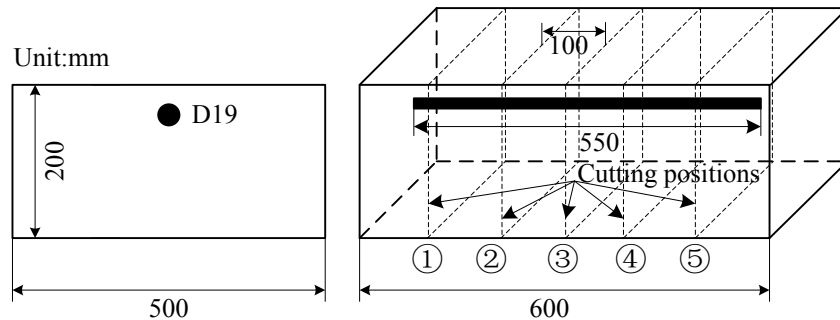


Figure 3.1 Specimen dimension for studying 2D cracking behavior

The two specimens named as RC30 and RC10 based on the cover thickness were casted using High Early Strength Portland Cement and coarse aggregates having a maximum diameter of 20mm. The mix proportion as shown in Table 2.1 was used. Before casting, the rebar of each specimen was measured for the initial mass m_0 (g) and the length l_0 (mm). After casting, they were cured for 14 days. The corrosion test using the proposed electric corrosion method was conducted afterwards. At the start of the testing, the concrete elastic modulus, compressive strength and splitting tensile strength were determined to be 31.95GPa, 39.92MPa and 2.97MPa separately.

For the study of 2D cracking behavior, an even distribution of corrosion amounts along the rebar length is targeted. Hence, the salt-water pool set on the concrete cover had a length of 500mm. Table 3.1 shows the test condition. The current density applied in the testing was $900\mu\text{A}/\text{cm}^2$ and the objective current flow was $159.77\text{A}\cdot\text{hr}$. During the test a severe cracking condition was found on the surface of RC10 and the corrosion testing of this specimen was thereby ended with a smaller current flow of $79.89\text{A}\cdot\text{hr}$. Although another specimen was tested again with the same test setup, a similar situation of surface cracking appeared under a current flow of $71.3\text{A}\cdot\text{hr}$. Since in the first specimen the internal crack patterns along the length of the rebar are comparatively consistent with each other, it is used for discussion. A schematic of the electric corrosion test is shown in Figure 3.2.

Table 3.1 Test conditions for study of 2D cracking behavior

Specimens	Cover thickness (mm)	Length of salt-water pool (mm)	Current flow (A*hr)
RC30	30	500	159.77
RC10	10		79.89, 71.30

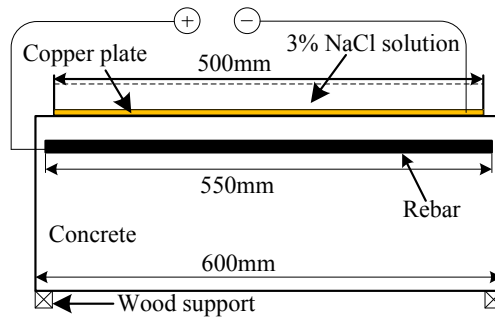


Figure 3.2 Electric corrosion test for 2D cracking behavior

After the corrosion tests, the specimens were cut at the positions as shown in Figure 3.1 with an interval of 100mm for the investigation of internal crack patterns. A crack scale was used to measure the crack widths and lengths. The rebars were obtained and cleaned using 10% diammonium hydrogen citrate firstly and then by a steel brush. To determine the corrosion distribution along the rebar, the rebar samples were further cut into small segments with a length of approximately 50mm. They were weighted for

the residual mass m (g) and measured for the precise length l (mm) by vernier caliper. The corrosion degree η of each rebar segment was determined as follows:

$$\eta = \frac{m_0 l - m l_0}{m_0 l} \quad (3.1)$$

3.3 Test results

Figure 3.3 shows the measured corrosion degrees against the corresponding positions along the rebar, in which each data represents the corrosion degree of a rebar portion about 50mm long. The corrosion degrees at different positions along the rebar of RC30 all seem to be close to 3%, while for RC10 a relatively concentrated corrosion occurs from 250mm to 450mm.

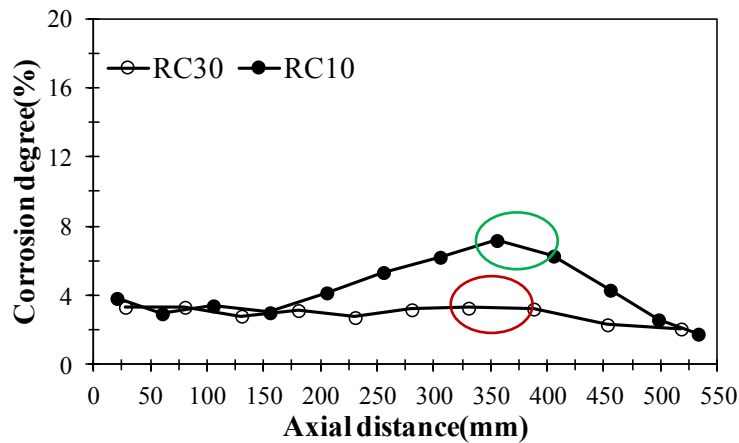


Figure 3.3 Measured distribution of corrosion degrees for RC10 and RC30

The appearance of concentrated corrosion in RC10 can be ascribed to the mutual effect between cracking and corrosion, i.e. cracks enable faster transport of chloride and water, thereby accelerating corrosion and causing more cracks. Figure 3.4 shows the surface crack conditions for RC10 and RC30. The part where multi-cracks occur (see cracks marked in blue in the specimen of RC10) corresponds to the area with the concentrated corrosion. On the other hand, a single crack in the rebar length direction (marked in red) appears on the surface of RC30.

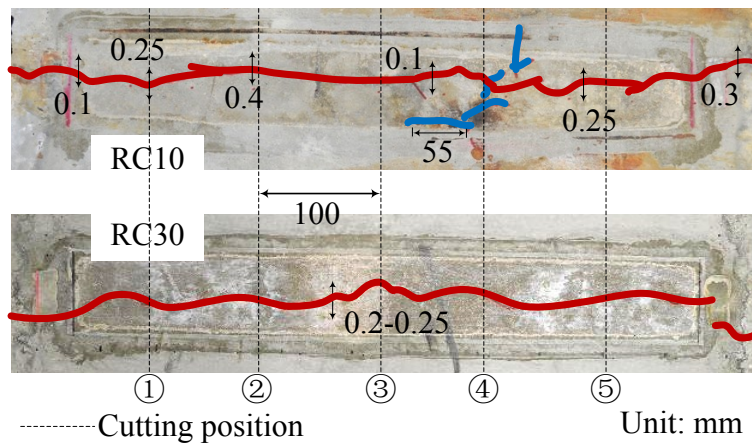


Figure 3.4 Surface cracking states for RC10 and RC30 (top view)

Two rebar samples obtained from the positions as indicated in Figure 3.3 are selected for the demonstration of the typical corrosion state around the rebar (see Figure 3.5). It is obvious that the upper part is far more corroded than the lower part.

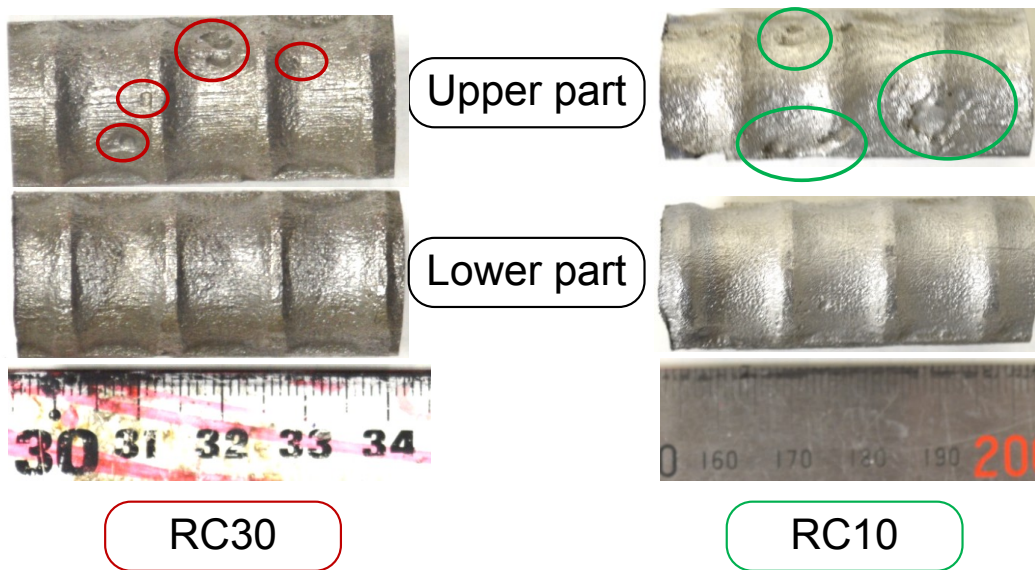
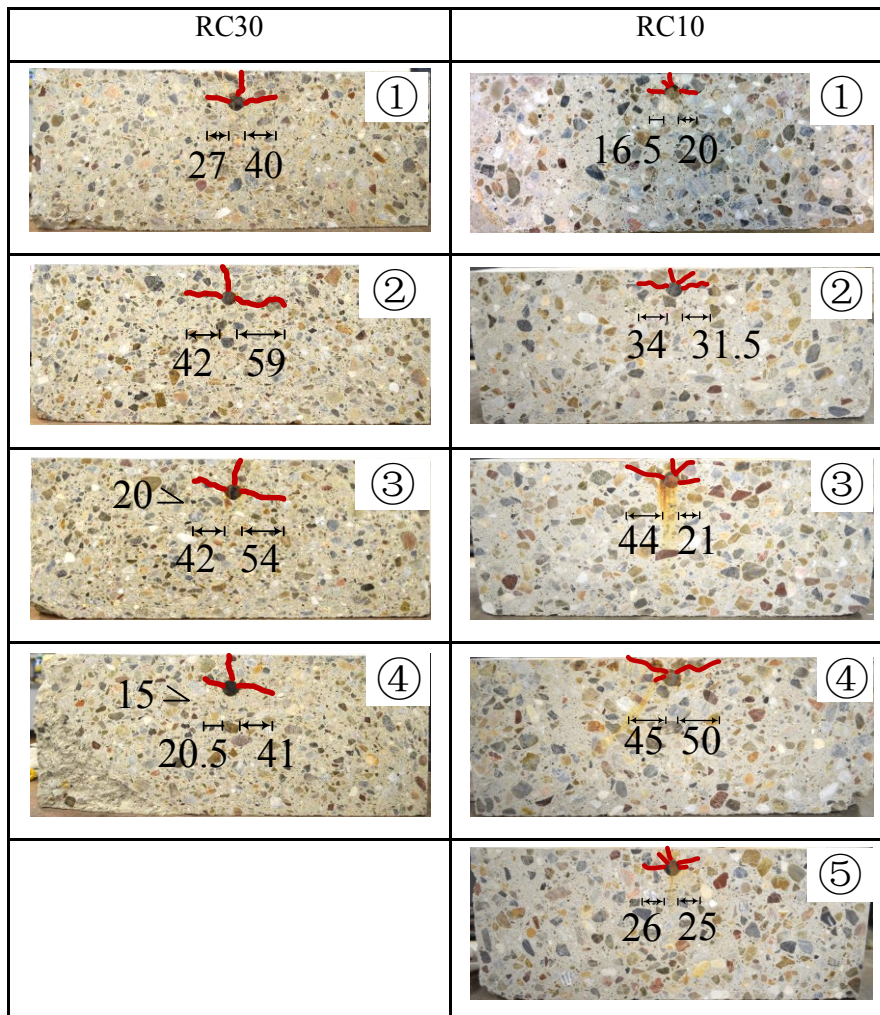


Figure 3.5 Corrosion states of rebar samples

Figure 3.6 compares the internal crack patterns observed from each cut section (see Figure 3.4) between the test specimens. For RC30, the internal crack patterns on different cut sections are nearly the same. One vertical crack connects the concrete surface to the rebar and two lateral cracks that are roughly parallel to the concrete

surface propagate to the concrete sides, which form the same crack pattern as suggested by Tsutsumi et al. (1996). For RC10, the expected internal crack pattern that consists of two inclined cracks only appears on the section ④, while the other four sections present a similar crack pattern including a vertical crack, a small inclined crack and two nearly horizontal cracks. This result suggests that the applicability of the theoretical models to predict internal crack pattern caused by chloride-induced corrosion is limited. The internal crack pattern may be affected by other factors besides the cover thickness. In order to clarify the influencing factors of 2D cracking behavior, a numerical analysis is carried out.



Unit: mm

Figure 3.6 Internal crack patterns for RC10 and RC30

3.4 Analytical model

3.4.1 Three-dimensional RBSM

The RBSM is a kind of discrete approaches, which represents a continuum material as an assemblage of rigid particle elements interconnected by zero-length springs along their boundaries (see Figure 3.7). The elements are randomly generated with Voronoi Diagram. Each of the elements has six degrees of freedom at its nucleus. At the center point of every triangle formed by the center of gravity and the vertices of the boundary between two elements, three springs, one normal and two shear springs, are defined. The response of the spring model provides an understanding of the interaction between particle elements instead of the internal behavior of each element based on continuum mechanics. In a RBSM model, cracks appear at the boundaries between adjacent rigid particles and the crack width can be automatically calculated as the relative displacement between their centers, which facilitate the simulation of crack pattern. In the analysis, three-dimensional RBSM developed by Yamamoto et al. (2008) is used.

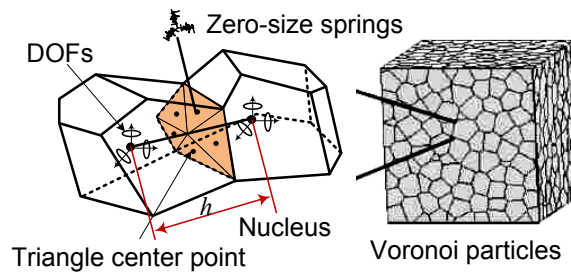


Figure 3.7 Voronoi particle definition of RBSM element

3.4.2 Material models

Figure 3.8 shows the material models of concrete used in the analysis. Tensile and compressive models are introduced into normal springs, where f_t represents tensile strength, h the distance between centers of the elements, G_F tensile fracture energy, f_c' compressive strength, G_{Fc} compressive fracture energy and E Young modulus. Shear model is introduced into shear springs, in which the shear strength is assumed to follow the Mohr-Coulomb type criterion with the tension and compression caps. Besides, the

shear transferring capacity at the cracked interface changes based on the crack opening. In order to take into consideration this effect, the shear stiffness G is reduced by using a function of the strain normal to the crack as shown in the shear-reduction model in Figure 3.8b. In the analysis, the material parameters of concrete were set in accordance with those obtained from the experiments.

Rebar is modeled as linear elastic with an elastic modulus of 200GPa.

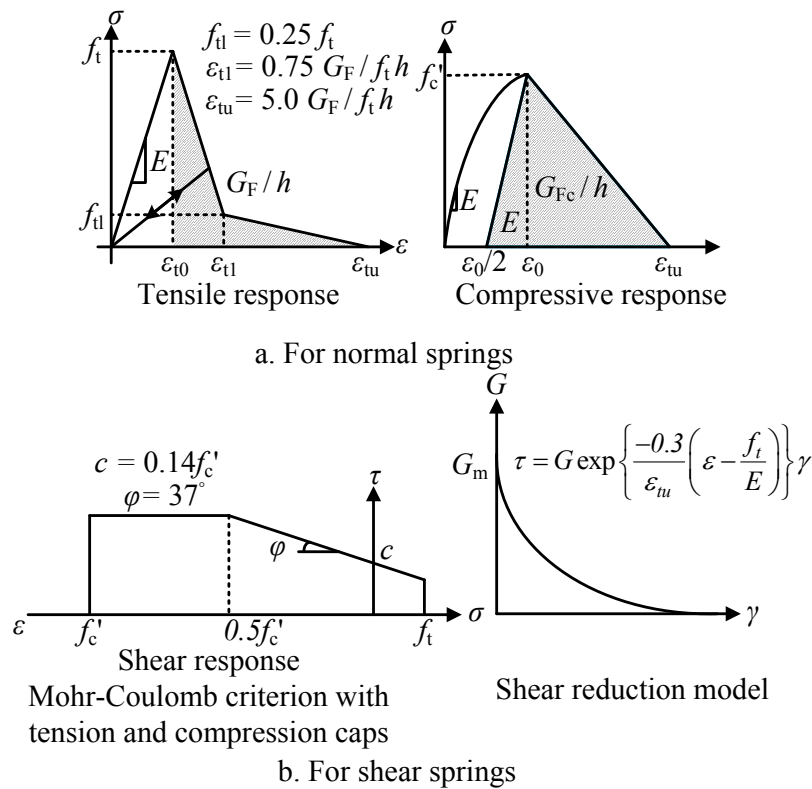


Figure 3.8 Concrete material model

3.4.3 Corrosion-expansion model

Based on the RBSM, the volume expansion of corrosion products is modeled by internal expansion pressure. A three-phase material model including rebar, corrosion products and concrete is established (see Figure 3.9). The corrosion products layer is modeled with an elastic material model and the thickness of this layer is assumed to be constant in the simulation. The previous work by Tran et al. (2011) suggests that when the corrosion products layer is set with a thickness of 1mm along with an elastic

modulus of 500MPa, the model enable a reasonable simulation of cracking behavior in comparison with the test results. These assumptions are also employed in this study.

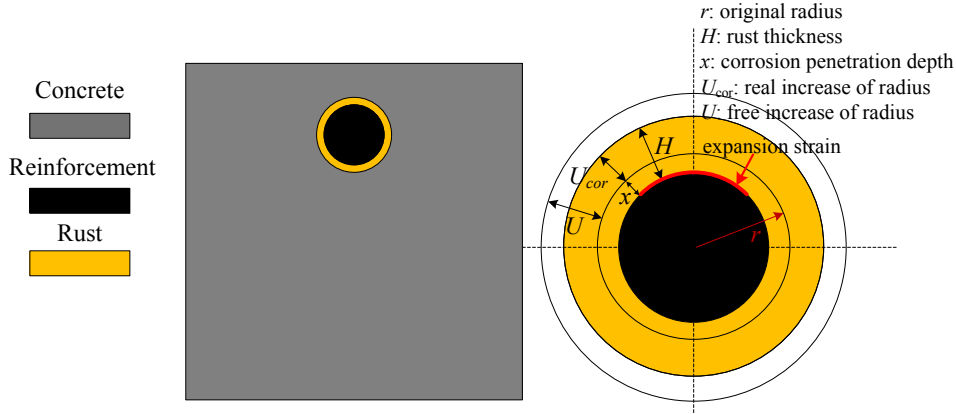


Figure 3.9 Corrosion-expansion model (Tran et al. 2011)

The increment of expansion stress at each analysis step is determined as:

$$\Delta\sigma_{cor} = E_r (\Delta\varepsilon - \Delta\varepsilon_0) = E_r \left(\frac{\Delta U_{cor}}{H} - \frac{\Delta U}{H} \right) \quad (3.2)$$

Where E_r is the elastic modulus of corrosion products layer, ΔU_{cor} an increment of real increase of rebar radius, ΔU the free increase of rebar radius, and H is the fictitious thickness of corrosion products layer.

Considering the nature of corrosion expansion, the internal expansion pressure is only activated in the normal direction. Hence, the expansion stress is employed only to the normal springs on the boundary between the corrosion products and the rebar layer. The shear stiffness for shear springs of the corrosion products layer is set nearly zero to model free sliding of corrosion products layer in the shear direction. In the analysis, the expansion stress is solved using the initial strain problem with increment of free increase of rebar radius ΔU in each step. The accumulative U should be satisfied with corrosion degree η :

$$U = \frac{\eta \cdot r \cdot (\alpha_{cor} - 1)}{2} \quad (3.3)$$

Where r is original rebar radius and α_{cor} is the volume-expansion ratio of corrosion products, which is assumed as 2.5. Since cracking is sensitive to the transient stress state, the applied ΔU in each step must be kept small enough to obtain a converged solution to simulate the crack propagation. In the simulation, increment of corrosion degree $\Delta\eta$ (%) as an input data is set as 0.02 to ensure a small ΔU .

3.4.4 Modeling for non-uniform corrosion around the rebar

The experimental study as shown in Chapter 2 suggested that a rebar could be more corroded at the part near cracked concrete than that surrounded by uncracked concrete and consequently corrosion would concentrate at the circumference facing the concrete cover. Considering the effect of cracks on the corrosion process, a non-uniform corrosion model is assumed as shown in Figure 3.10. Here the angle θ is used to represent the distribution of corrosion products around the rebar. When a vertical crack with a width greater than 0.1mm appears in the concrete cover, the corrosion products are only distributed in the upper part facing the concrete cover (see the shadow area) (Tran et al. 2011). Correspondingly, the expansion stress is only applied in this area.

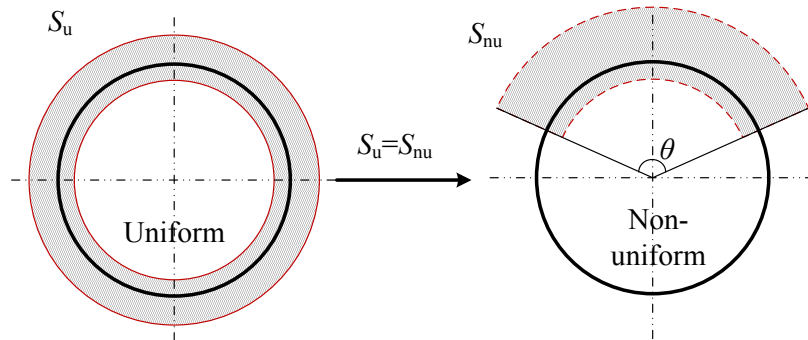


Figure 3.10 Non-uniform corrosion model

3.5 Analytical results in comparison to test data

The corrosion-expansion model is applied to analyze the cracking process of the specimens tested, where the internal crack pattern is focused. The created RBSM model

has the same dimension as the tested specimen (see Figure 3.11). The mesh size of the Voronoi particles near the rebar is 5 or 2mm for the cover thickness of 30 or 10mm respectively, while the mesh size in the outer area is 30mm. According to the observed corrosion states around the rebars (see Figure 3.5), θ is assumed to be 90° or 180° (quarter or half model). The concentrated corrosion along the rebar length that occurred in the RC10 was not considered in the study of 2D cracking behavior. Hence, the corrosion amounts along the rebar stay the same.

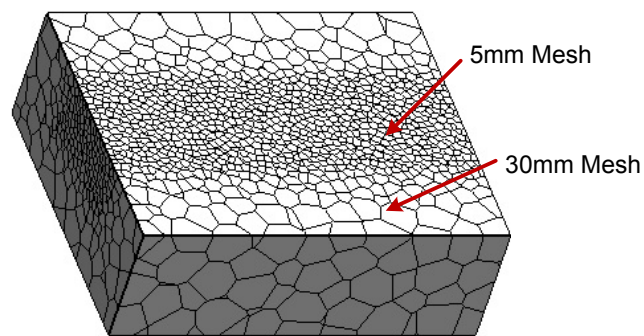


Figure 3.11 3D view of RBSM model

Figure 3.12 shows the simulated internal crack patterns under a corrosion degree of 3%. In the analysis, the crack is that with a width greater than 0.1mm, which is manifested with a color of yellow. Lateral crack length is the horizontal distance calculated from the side of the rebar to the tip of the crack. For 30mm cover, both quarter and half model show a similar crack pattern to that observed in the test, but the lengths of lateral cracks predicted by half model are much bigger. This difference will be discussed in the parametric studies. In comparison with the measured crack length, quarter model seems to be better for the case with 30mm cover. On the other hand, for 10mm cover, the internal crack pattern simulated by half model is similar to the test result.

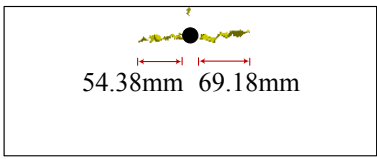
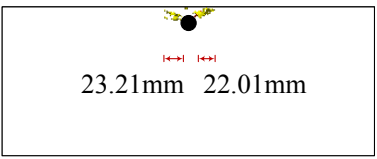
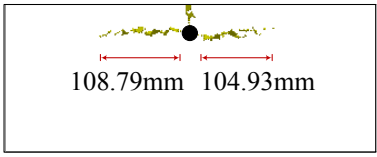
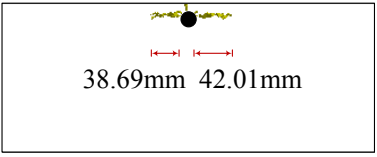
θ	RC30	RC10
90° (Quarter model)	 54.38mm 69.18mm	 23.21mm 22.01mm
180° (Half model)	 108.79mm 104.93mm	 38.69mm 42.01mm

Figure 3.12 Simulated internal crack patterns for RC10 and RC30

The analytical results show when corrosion distributes in the entire half circumference ($\theta=180^\circ$), the specimens with different cover thicknesses share the same internal crack pattern, which contradicts the concept of the theoretical models i.e. the internal crack pattern for a given rebar diameter is determined by the cover thickness. The corrosion distribution around the rebar appears to have a great influence on the internal crack pattern. Therefore the parametric study based on the value of θ is conducted. The angle θ is ranged from 360° to 45° , in which 360° represents a uniform corrosion process.

3.6 Effect of corrosion distribution around rebar

Figure 3.13 and Figure 3.14 show comparisons of simulated internal crack patterns for different corrosion distributions, in which the targeted corrosion degrees are 2.5% and 5% respectively. The cracks wider than 0.3mm are highlighted in red in this figure. Comparing the crack width and length, it appears that under the same level of corrosion, non-uniform corrosion causes more cracking in the concrete cover than uniform corrosion (see the red cracks in the non-uniform corrosion cases).

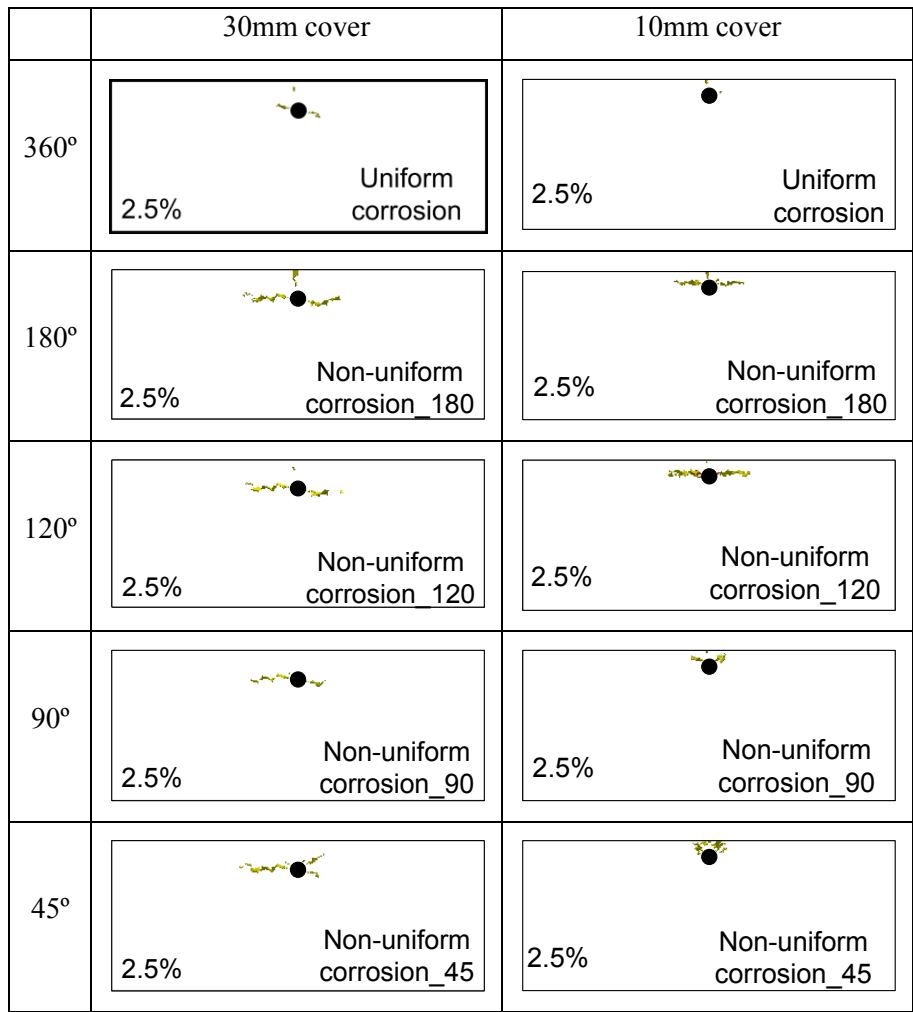


Figure 3.13 Comparison of internal crack patterns between different corrosion distributions (2.5% corrosion)

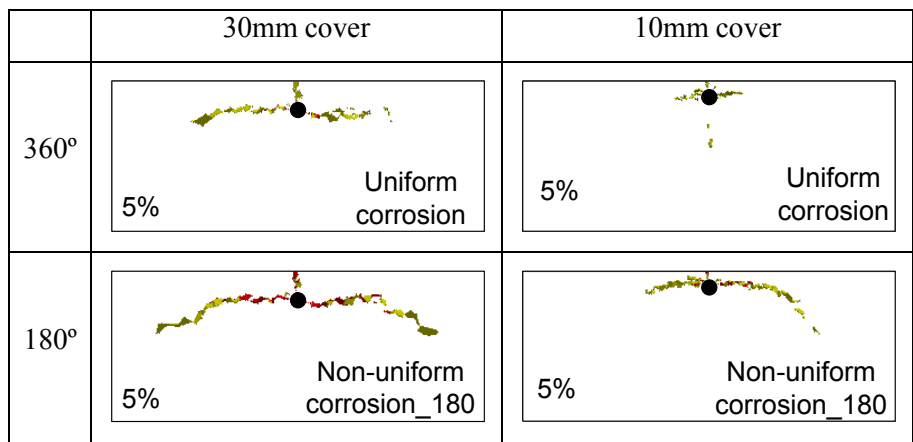


Figure 3.14 Comparison of internal crack patterns between different corrosion distributions (5% corrosion)

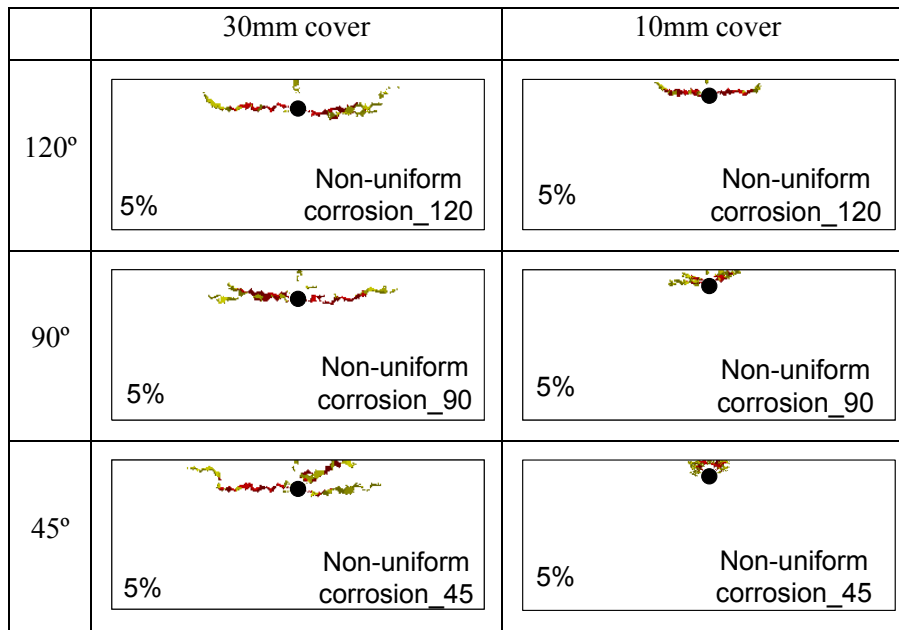


Figure 3.14 Cont.

Both series with different cover thicknesses demonstrate that internal crack pattern is in a strong relation to the corrosion distribution. For 30mm cover case, when θ equals 180° or 360°, lateral cracks grow to the concrete sides. Comparatively, if corrosion concentrates in a much smaller area of the rebar part facing the concrete cover ($\theta \leq 120^\circ$), the propagation of lateral cracks is firstly in the horizontal direction and then diagonal to the concrete surface. Besides, the small width of vertical crack indicates that lateral crack propagation dominates in the development of internal cracks. When θ equals 45°, a third later crack appears in addition to two horizontal cracks, which directly inclines to concrete surface as corrosion degree increases. For 10mm cover, the crack patterns are roughly the same as those with 30mm cover when corrosion distributes in a broad area around the rebar ($\theta \geq 120^\circ$). Only when corrosion is highly concentrated ($\theta \leq 90^\circ$) does the crack pattern consisting of two explicit inclined cracks appear as indicated by the theoretical models for the small concrete cover. It suggests that the corrosion states around the rebar should be firstly considered for the prediction of internal cracking situation.

Figure 3.15 presents the development of surface crack width against the corrosion degree. As can be seen, regardless of different cover thicknesses, the

analytical results both show when non-uniform corrosion occurs, at the same level of corrosion that can cause surface cracking, the surface crack width for the case of θ equal to 180° is greater than that of uniform corrosion case ($\theta = 360^\circ$) since for non-uniform corrosion the resulting expansion pressure only distributed at the circumference facing the concrete cover. However, when corrosion area further concentrates ($\theta \geq 120^\circ$), the evolution rate becomes smaller. It is in accordance with the change of internal crack pattern, i.e. the occurrence of inclined lateral crack. The experimental study carried out by Kawamura et al. (2010) has indicated that both surface crack opening and the propagation of lateral cracks are related to concrete surface deformation. With a decrease of θ , concrete surface deformation is confined within a small field because the rebar area that can produce expansion pressure is reduced. It results that lateral cracks gradually incline to the concrete surface instead of propagating to the sides. Accordingly, the surface crack width and the lateral crack length are relatively small.

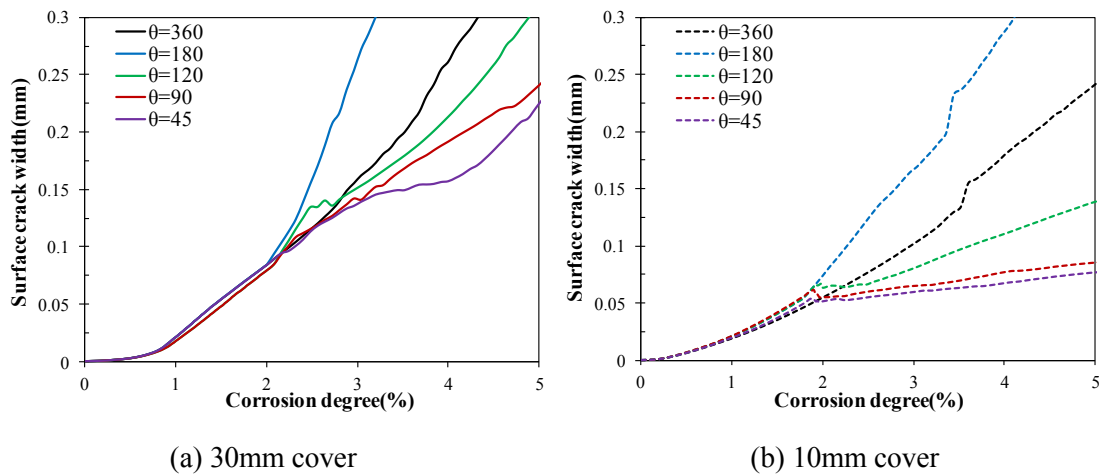


Figure 3.15 Surface crack evolution for different corrosion distributions (240.5mm side-cover)

The side-cover thickness affects the deformation ability of concrete surface and thereby influences the evolution of surface crack width, which is an important on-site survey item. Hence, the effects of side-cover thickness on the development of surface cracks and internal cracks are also discussed herein in a combination with corrosion distribution. In the analysis, the width of the specimen is reduced from 500 to 200mm.

Figure 3.16 shows the simulated internal crack patterns on the basis of various corrosion distributions around the rebar, which correspond to a corrosion degree of 5%. When θ is assumed to be 90° , the analytical results agree with the crack patterns observed by Kawamura et al. (2010) (see Figure 3.17). In the test, the single-rebar specimen with a similar section dimension of $150\text{mm} \times 150\text{mm}$ was studied. The analysis with a reduced cover thickness presents a similar trend with regard to the effect of corrosion distribution. The internal crack pattern for 10mm cover is the same as that for 30mm cover when corrosion appears in a large area around the rebar ($\theta \geq 120^\circ$). It indicates that corrosion distribution around the rebar may have a more influence on the internal crack propagation than concrete cover thickness.

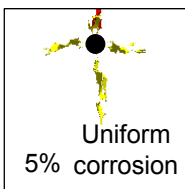
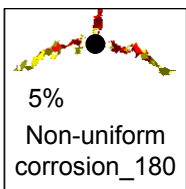
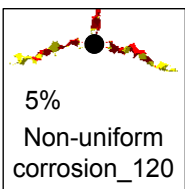
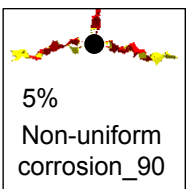
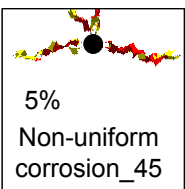
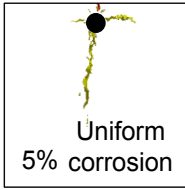
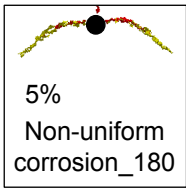
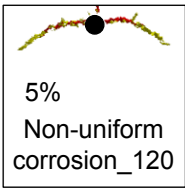
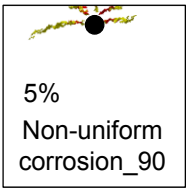
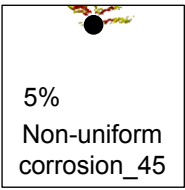
360°	180°	120°	90°	45°
30mm cover				
 Uniform 5% corrosion	 5% Non-uniform corrosion_180	 5% Non-uniform corrosion_120	 5% Non-uniform corrosion_90	 5% Non-uniform corrosion_45
10mm cover				
 Uniform 5% corrosion	 5% Non-uniform corrosion_180	 5% Non-uniform corrosion_120	 5% Non-uniform corrosion_90	 5% Non-uniform corrosion_45

Figure 3.16 Comparison of internal crack patterns between different corrosion distributions (90.5mm side-cover)

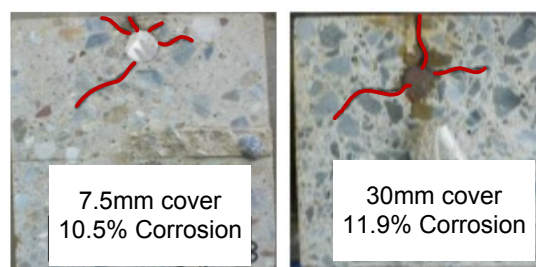


Figure 3.17 Internal crack patterns observed in test (Kawamura et al. 2010)

Figure 3.18 compares the development of surface crack width between different side-cover thicknesses. As can be seen, for a small side cover, the corrosion distribution hardly affects the evolution rate of surface crack width. In contrast, for a large side cover the more concentrated corrosion causes a smaller surface crack width. It can be contributed to the distribution of the concrete surface deformation. Figure 3.19 shows the surface deformation under a corrosion degree of 3%. When the side-cover thickness is as small as 90.5mm, vertical deformation can be generated along the whole 200mm long surface. On the other hand, for 240.5mm thick side-cover, the deformation distributes in the area with a length less than 500mm, which would further decrease for a concentrated corrosion (see $\theta = 90^\circ$).

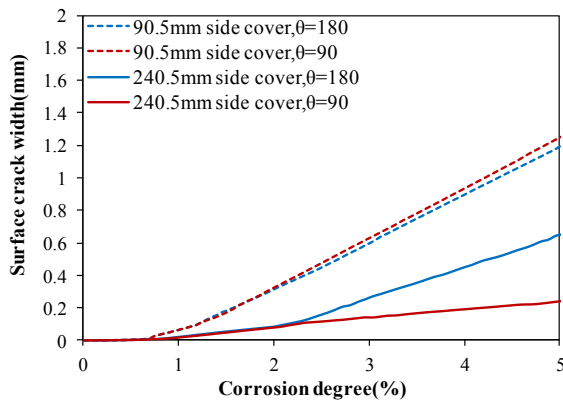


Figure 3.18 Surface crack evolution for different side-cover thicknesses

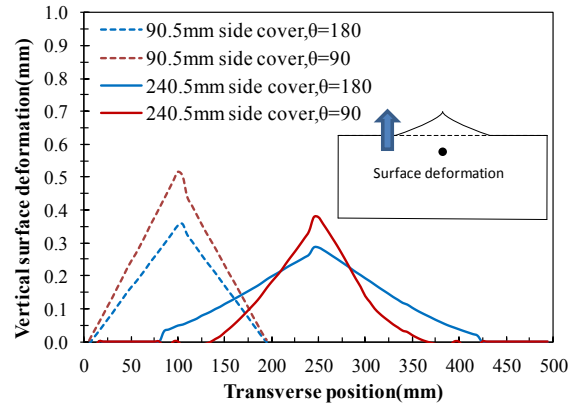


Figure 3.19 Concrete surface deformation for different side-cover thicknesses

3.7 Effect of concrete material properties

The effect of concrete material properties on the cracking behavior is also analyzed using the corrosion-expansion model. Experimental studies involved with material properties (Alonso et al. 1998, Vu et al. 2005) were to investigate the influence of water-cement ratio on crack development rather than fracture energy or tensile performance, since they can be hardly used as test variables. In comparison, one of the advantages of RBSM model is that different material properties can be modeled with

reasonable parameters (see Figure 3.20). Hence it is convenient to study the effect of material properties by the corrosion-expansion model. Moreover, the clarification of their influences will be beneficial to repair work, since it gives judgments on the efficiency of high strength material or high ductile material on cracks repairing.

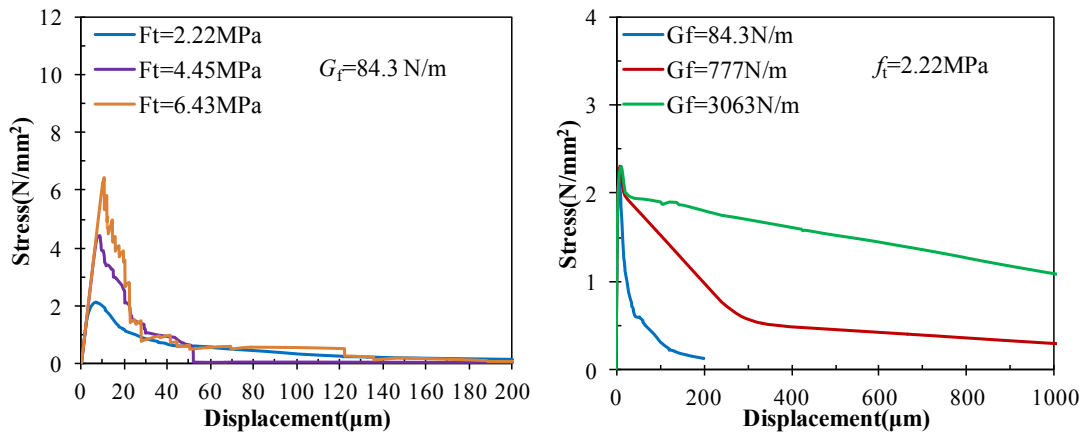
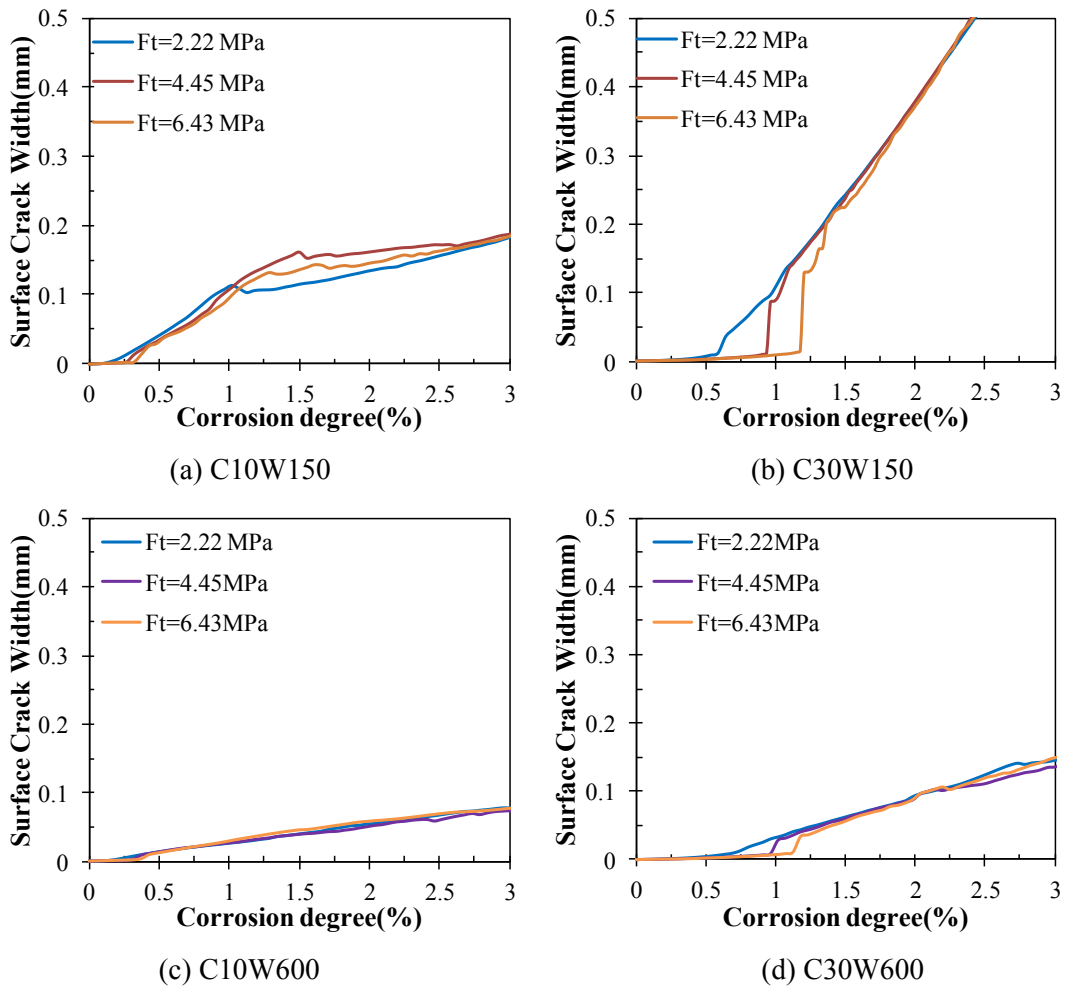


Figure 3.20 Stress-displacement relationships investigated for effects of concrete material properties

Two groups of material properties were obtained by tension simulation based on a mesh size of 5mm. In the first group, tensile strength has a range of 2.22 to 6.43MPa while fracture energy stays the same as 84.3N/m. In the other group, fracture energy is increased from 84.3 to 3063N/m while the tensile strength is kept as 2.22MPa. Various cross-sectional dimensions were also considered in the parametric study, including 150mm×150mm, 300mm×150mm, and 600mm×150mm (width × height). Cover thickness was varied from 10 to 30mm simultaneously. The quarter model ($\theta = 90^\circ$) was employed for considering non-uniform corrosion around the rebar.

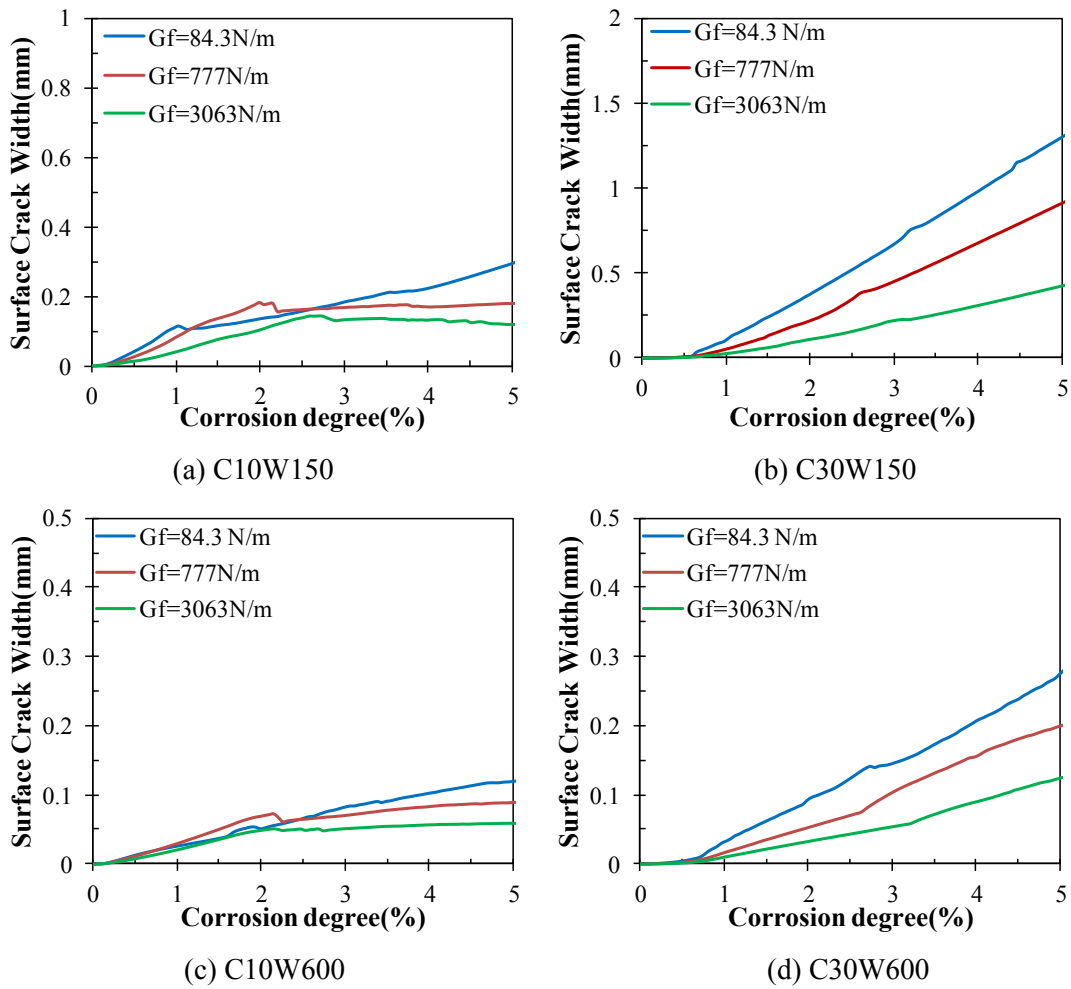
Figure 3.21 shows surface crack propagation for different tensile strengths. It is obvious that corrosion degree required for surface crack initiation increases with tensile strength. However surface crack width propagates following nearly the same route after initiation. Although surface crack generation is retarded by high tensile strength, a bigger crack opening seems to appear and then expand rapidly. It can be deduced that surface crack propagation is not related with tensile strength.



Noted: C : cover thickness; W specimen width

Figure 3.21 Surface crack development for various tensile strengths

Surface crack development for different fracture energies is presented in Figure 3.22. In general, it can be seen that regardless of various geometric features, surface crack width decrease clearly when fracture energy increases. Compared with effects of tensile strength, it seems that surface crack propagation is controlled by fracture energy while tensile strength is dominant in crack initiation. Thus, ductile materials with high fracture energies can be used to control surface crack development for maintenance of cracked concrete due to rebar corrosion.



Noted: C: cover thickness; W specimen width

Figure 3.22 Surface crack development for various fracture energies

It is also found that in the case of high fracture energy internal crack pattern becomes in relation with the specimen width. The internal crack patterns of the specimens with a cover thickness of 10mm were almost the same and irrelevant to specimen width even if fracture energy was increased. Therefore, only results with regard to 30mm cover thickness are discussed as follows.

Figure 3.23 displays internal crack patterns corresponding to corrosion degrees of 1.9%, 2.7% and 3.8% separately for a specimen width of 150mm, where red signs represent the crack with a width of 0.1mm and over. In this case, various fracture energies result in the same crack pattern, i.e. lateral cracks develop towards sides of the

specimen along with vertical crack propagating from surface to rebar. The influence of fracture energy is merely that crack propagation becomes slow.

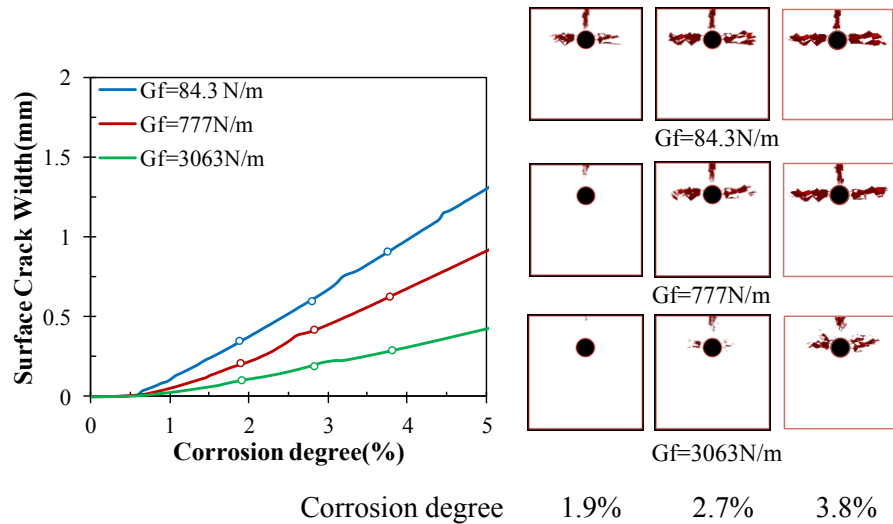


Figure 3.23 Internal crack pattern of specimen with a width of 150mm

Figure 3.24 presents internal crack patterns of specimen with a width of 600mm under the same corrosion levels as discussed previously. It is clear that high fracture energy leads to lateral cracks developing diagonally to the concrete surface. Besides, lateral crack length decreases evidently with an increase of fracture energy as shown in Figure 3.25. It is identified that ductile materials with high fracture energy used in repair can constrain cracked area and thereby reduce the spalling area of a slab specimen.

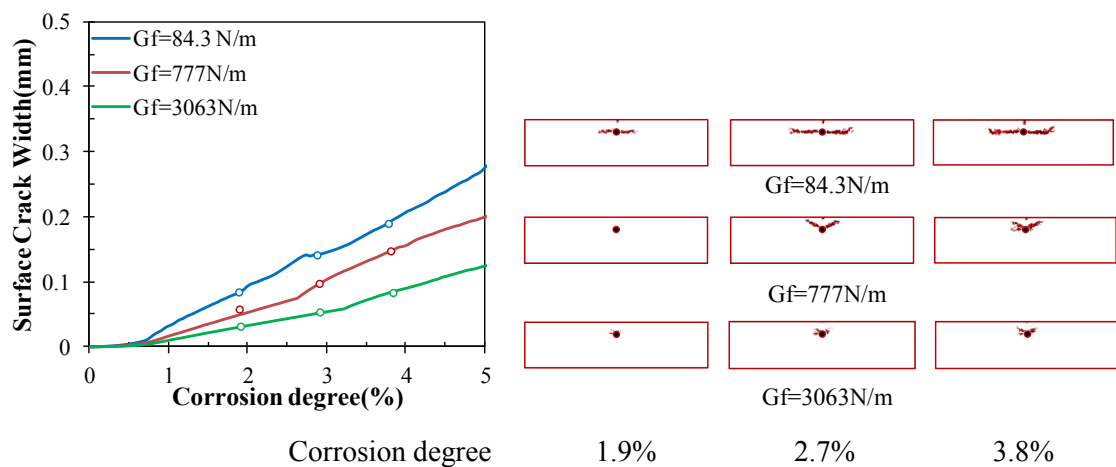


Figure 3.24 Internal crack pattern of specimen with a width of 600mm

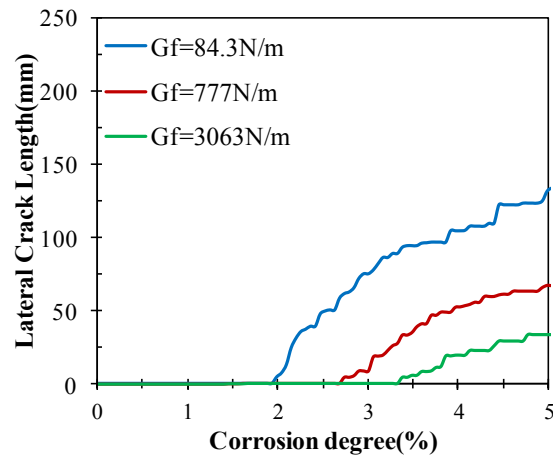


Figure 3.25 Lateral crack length of specimen with a width of 600mm varied in fracture energy

3.8 Summary and conclusions

The 2D cracking behavior of the single-rebar specimens with different cover thicknesses is examined experimentally and analytically, which is also compared with the prediction by the theoretical models. It is also identified that the corrosion-expansion model used in the analysis can simulate accurately internal crack pattern, if the corrosion distribution around the rebar is properly simulated. Through comparing to the internal crack patterns observed in the test, the key parameter θ of the model denoting the corrosion distribution is confirmed for 10 or 30mm cover depth, which is to be employed in the analysis of 3D cracking behavior.

Both experimental and analytical results demonstrate that internal crack pattern is highly dependent upon the corrosion distribution around the rebar rather than cover thickness as suggested by the theoretical models. When rebar is corroded broadly in the circumferential direction, the internal crack pattern for 10mm cover may be the same as that for 30mm cover, which consists of parallel cracks to the concrete surface. When corrosion concentrates significantly in the area facing the concrete cover, the internal cracks for 30mm cover may also incline to the concrete surface, if the side-cover thickness is sufficiently large. The analysis also offers an implication for the assessment of corrosion damage using surface crack width. When the side-cover thickness or the

spacing of rebars is comparatively large, the corrosion that distributes in a small area around the rebar may lead to a great development of internal cracks without a discernible sign in the surface crack width. Moreover, internal cracks can incline to the concrete surface, which may accelerate the corrosion process and also induce cover spalling. This phenomenon may even occur in a concrete cover as thick as 30mm, which is normally considered to be safe.

The parametric study regarding the effect of concrete material properties shows that surface crack initiation is determined by tensile strength, while fracture energy has a significant influence on surface crack propagation. For a wide RC specimen, an increase of fracture energy can reduce the cracking area in the concrete cover. It indicates that ductile materials with high fracture energy are efficient to limit the cracking damage caused by rebar corrosion.

4 Evaluation of 3D Concrete Cracking and Cover Spalling due to Local Corrosion

4.1 Introduction

In practical situations when RC structures exposed to chloride-laden environments, penetrated chloride ions cause localized breakdown of passive film of a rebar, especially in the presence of initial cracks due to creep and shrinkage (Bertolini et al. 2004). Consequently, corrosion is limited within a small region along the length of the rebar. A macro cell coupling can form between this region and other passive parts, thereby increasing the corrosion rate. Local corrosion may result in a fast development of concrete cracks as shown in a real case in Figure 4.1. In this case, a part of concrete detached from the concrete structure of an expressway in Japan, while no obvious surface cracks had been found in the previous maintenance. It is considered that the spalling is due to internal crack propagation and may be related to local corrosion. Hence, it is essential to study the damage caused by local corrosion.

However, at present, 3D cracking behavior affected by local corrosion along the rebar length is not clear. Studies concerned with this problem are rarely reported in literature. In this chapter, 3D crack propagation due to local corrosion is investigated in comparison with 2D cracking behavior. In the experimental study, a local corrosion state that is corrosion concentrates at the center part of rebar is simulated using salt-water pools of various sizes. This test method for controlling corrosion profile is confirmed by the measurement of distribution of corrosion degree along the rebar. The resulting crack patterns and their relation to cover spalling are examined. In addition, the corrosion-expansion model is used to simulate the crack pattern by assuming the

distribution of corrosion amounts on the basis of the test results. The cracking mechanism caused by local corrosion is also discussed.

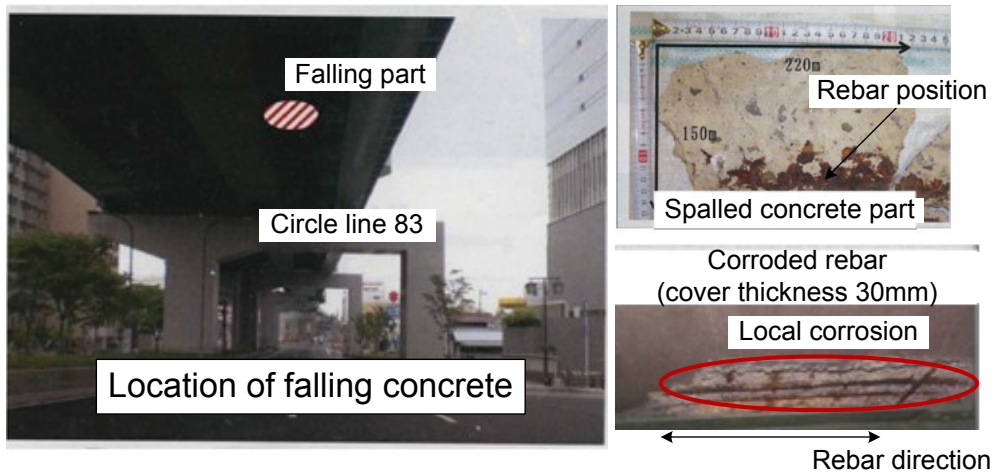


Figure 4.1 Practical case of local corrosion-induced concrete spalling

4.2 Experimental setup

In order to compare with the 2D crack propagation studied in Chapter 3, the same type of single-rebar specimen was used, in which varied cover thicknesses as 10 and 30mm were also considered. Before casting the specimens, the rebars embedded were measured for the initial weight and the length to obtain the unit mass. A total of eight specimens were casted using High Early Strength Portland Cement and coarse aggregates with a maximum diameter of 20mm. The mixture proportion is the same as indicated in Table 2.1. Although the specimens were casted separately at different dates, they showed a similar compressive strength of approximately 39MPa after 14 days curing.

The electric corrosion method using a salt-water pool on the concrete cover was used to induce corrosion of rebar. In order to obtain a varied corrosion distribution along the rebar length, the length of the salt-water pool used was shortened to 300 or 100mm (see Figure 4.2). It is considered that the changed distance from rebar portions to the cathode area tends to lead to varied corrosion amounts along the rebar. The test

based on bare rebar specimens has proved that the use of a small cathode can concentrate the resulting corrosion to a certain extent.

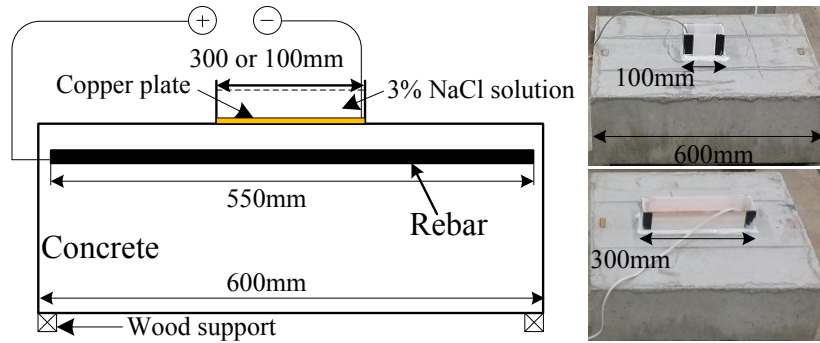


Figure 4.2 Electric corrosion test for 3D cracking behavior

Table 4.1 Test variables for study of 3D cracking behavior

Specimens	Cover thickness (mm)	Length of salt-water pool (mm)	Current flow (A*hr)
L300C30_1	30	300	102.91
L300C30_2			159.77
L100C30_1		100	35.38
L100C30_2			159.77
L300C10_1	10	300	79.89
L300C10_2			68.54
L100C10_1		100	79.89
L100C10_2			159.77

During the corrosion test, the nominal current density applied was $900\mu\text{A}/\text{cm}^2$. The test variables included the length of salt-water pool and current flow as described in Table 4.1. Different current flows were applied to obtain various corrosion levels. For validating the corrosion method applied, the tests of the specimens with small objective corrosion levels were conducted firstly and the current flows differed. The objective current flow of the specimen L300C10_2 was $159.77\text{A}\cdot\text{hr}$. However, in the test a part of concrete near salt-water pool detached and the corrosion testing was stopped, when the accumulated current flow reached $68.54\text{A}\cdot\text{hr}$.

After each corrosion test was completed, the surface crack pattern was observed and crack widths at different positions in the rebar length direction were measured using a crack width scale. Then the specimen was cut at the positions as shown in Figure 4.3 with an interval of 100 or 150mm to enable the observation of internal crack patterns and the measurements of the internal crack widths and lengths. At the end, the rebars were obtained and cleaned by firstly immersing the rebar samples in 10% diammonium hydrogen citrate for 24h and then using a steel brush. The collected rebars were further cut into small segments with a length of approximately 50mm. They were measured for the residual mass and the precise length to determine the corrosion distribution along the rebar according to the equation (3.1).

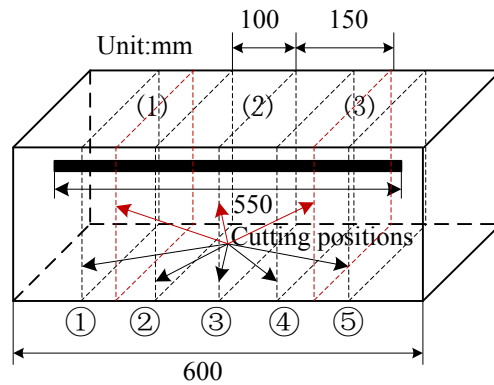


Figure 4.3 Cutting position for investigating internal crack pattern

4.3 Experimental results

4.3.1 Corrosion distribution along rebar

Figure 4.4 presents the corrosion degrees obtained at different positions along the rebar, in which each data represents the corrosion degree of a rebar portion with a length of about 50mm. The positions of salt-water pools are also indicated in the figures. As can be seen, all test series present that the corrosion level within the area under the salt-water pool is obviously greater than that locating outside the pool. The difference is at least 6 times as shown in the series with a concrete cover of 30mm (see L100C30_1 in Figure 4.4a) and this difference may be enlarged as an increase of current flow.

Regardless of cover thickness, the corrosion distribution along the rebar length appears to be a trapezoidal distribution when a 300mm long salt-water pool is applied. In the cases with 100mm long salt-water pool, the distribution exhibits a triangular form. These results again confirm that various corrosion distributions can be achieved by different arrangements of cathode in the electric corrosion test.

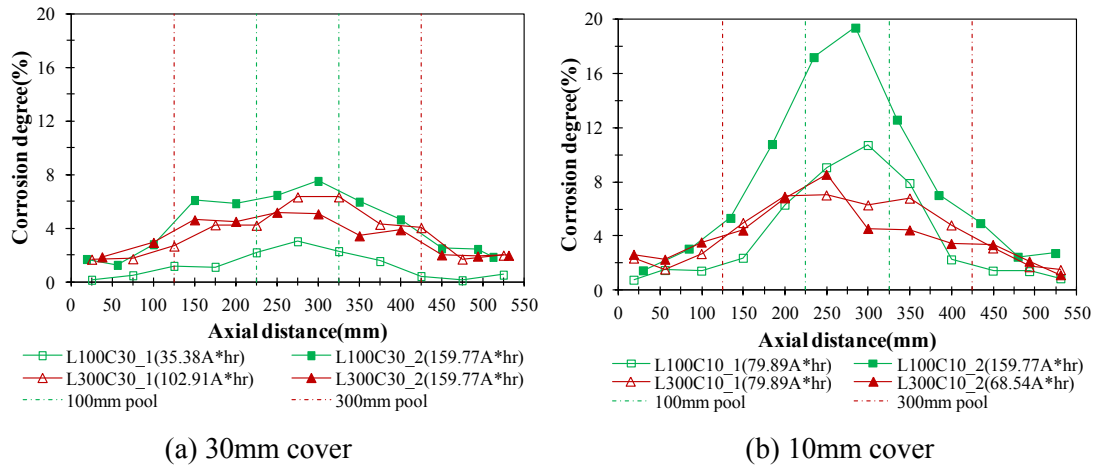


Figure 4.4 Measured distribution of corrosion degree

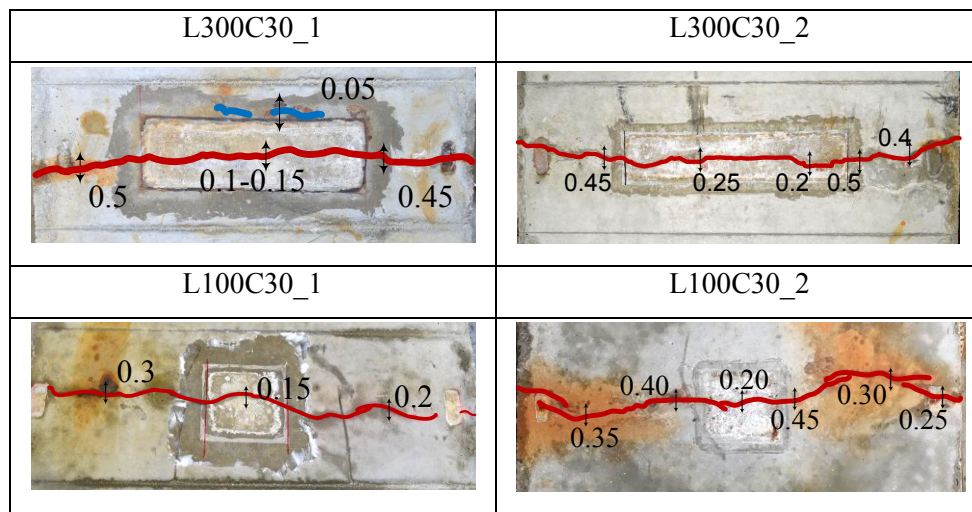
It is also noted that when applied with the same current flow, the corrosion level reached in the specimens with 10mm cover is greater than that with 30mm cover. Nossoni and Harichandran (2012) experimentally investigated the current efficiency of electric corrosion test and suggested that it might increase with an increase of chloride concentration in the system. The transport of water and chloride through a 10mm thick concrete cover is considered to be much faster than that through a 30mm cover, which may result in a bigger current efficiency and consequently a higher current level.

4.3.2 Concrete crack pattern

4.3.2.1 30mm cover case

Figure 4.5 shows a comparison of surface crack patterns between different test cases. A main crack in the rebar length direction (marked in red) appears on the concrete surface for all test specimens. The surface crack width increases as the current flow increases. However, comparing the crack widths at different positions, it seems

that the crack width within the area under salt-water pool is smaller than that at the external areas. Taking the specimen L300C30_2 as an example, the surface crack width is about 0.2-0.25mm at the center part and doubles at the sides. Moreover, the specimen L300C30_1 yields a crack parallel to the main crack (marked in blue), which has a width of 0.05mm and locates 60mm away from the main crack. Given that the corrosion amount at the center part is much larger, it may be deduced that internal crack propagation is dominant.



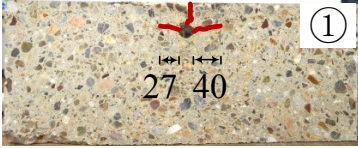
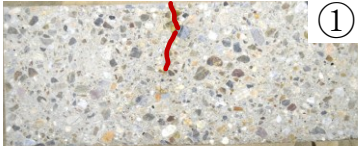
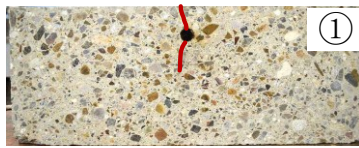
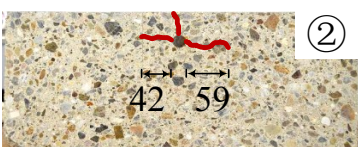
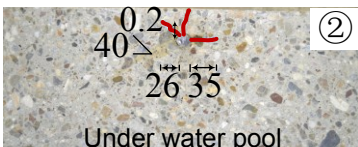
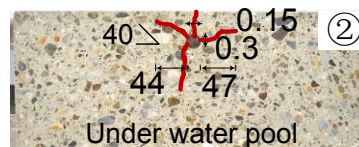
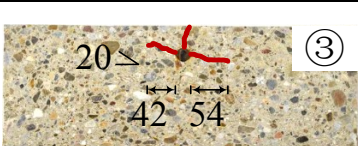
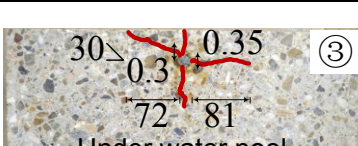
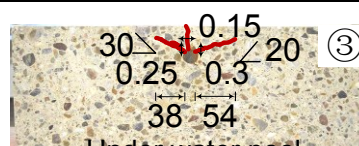
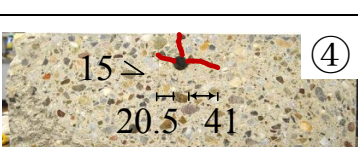
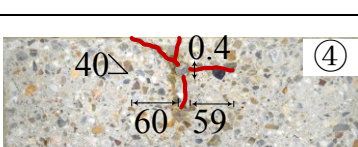
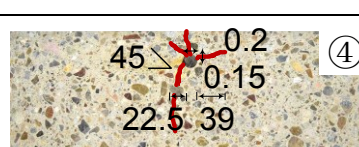


Unit: mm

Figure 4.5 Surface crack patterns of test specimens with 30mm cover

Figure 4.6 shows the internal crack patterns observed from each cut section between the test specimens, in which the internal crack pattern caused by uniform corrosion along the rebar length (RC30 presented in Chapter 3) are also shown for comparison. In the case of uniform corrosion, internal crack patterns on different cut sections stay the same. One vertical crack appears along with two lateral cracks propagating horizontally or inclining at a small angle less than 20°. When rebar is subjected to the varied corrosion distribution, a very interesting phenomenon of cracks propagation happens. In the cases of L300C30, only vertical cracks appear at the outside of salt-water pool where corrosion degree is relatively small, while within the area under salt-water pool two lateral cracks with large widths also appear. Moreover, the lateral crack directly inclines to the concrete surface at an angle of 30° - 45°, which

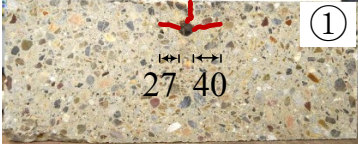
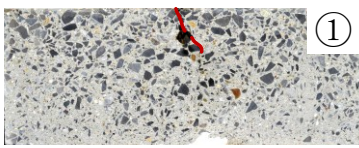


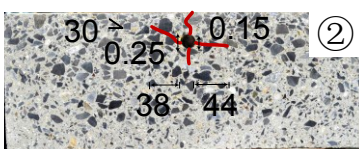
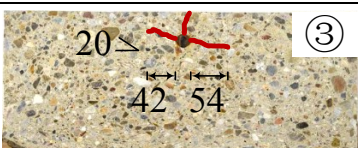
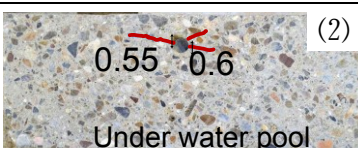
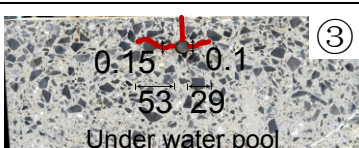
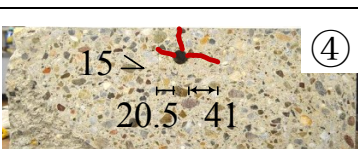
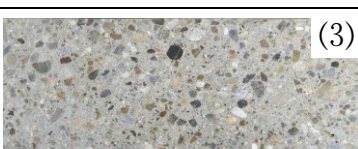
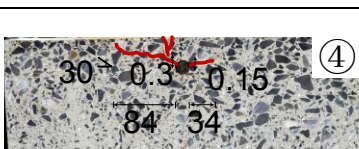

forms the parallel crack on the surface of L300C30_1 as shown in Figure 4.5. Provided that the corrosion level in concrete is sufficient, the vertical crack that connects the concrete surface to the rebar associate with the lateral crack that propagates diagonally to the concrete surface tend to form a fracture plane, which may be considered to represent cover spalling. Similarly, the cases of L100C30 also show varied internal crack patterns on different cut sections and the appearance of inclined lateral crack near salt-water pool, demonstrating a potential spalling.

Unit: mm

RC30 (uniform corrosion along the rebar)	L300C30	
		
		
		
		
		

(a) L300C30

Figure 4.6 Internal crack patterns of test specimens with 30mm cover

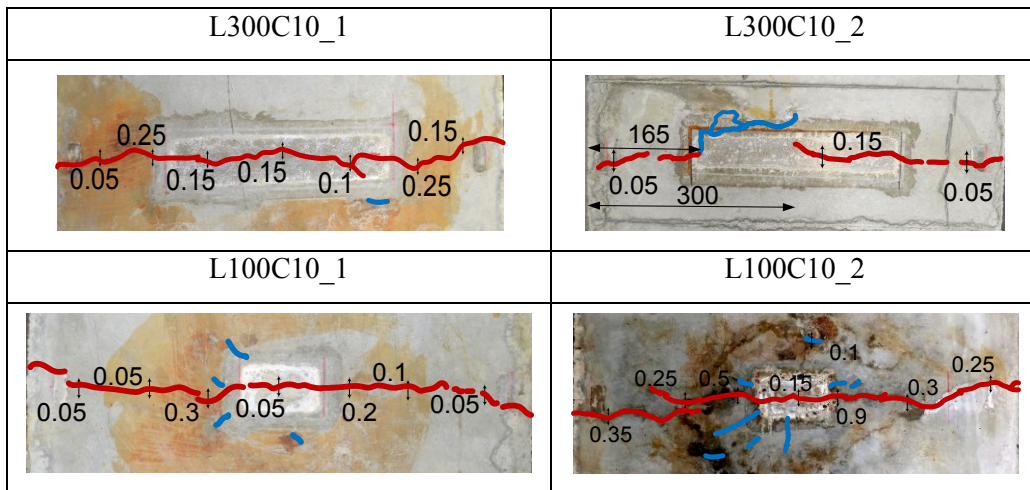
RC30 (uniform corrosion along the rebar)	L100C30	
		
		
		
		
		

(b) L100C30

Figure 4.6 Cont.

4.3.2.2 10mm cover case

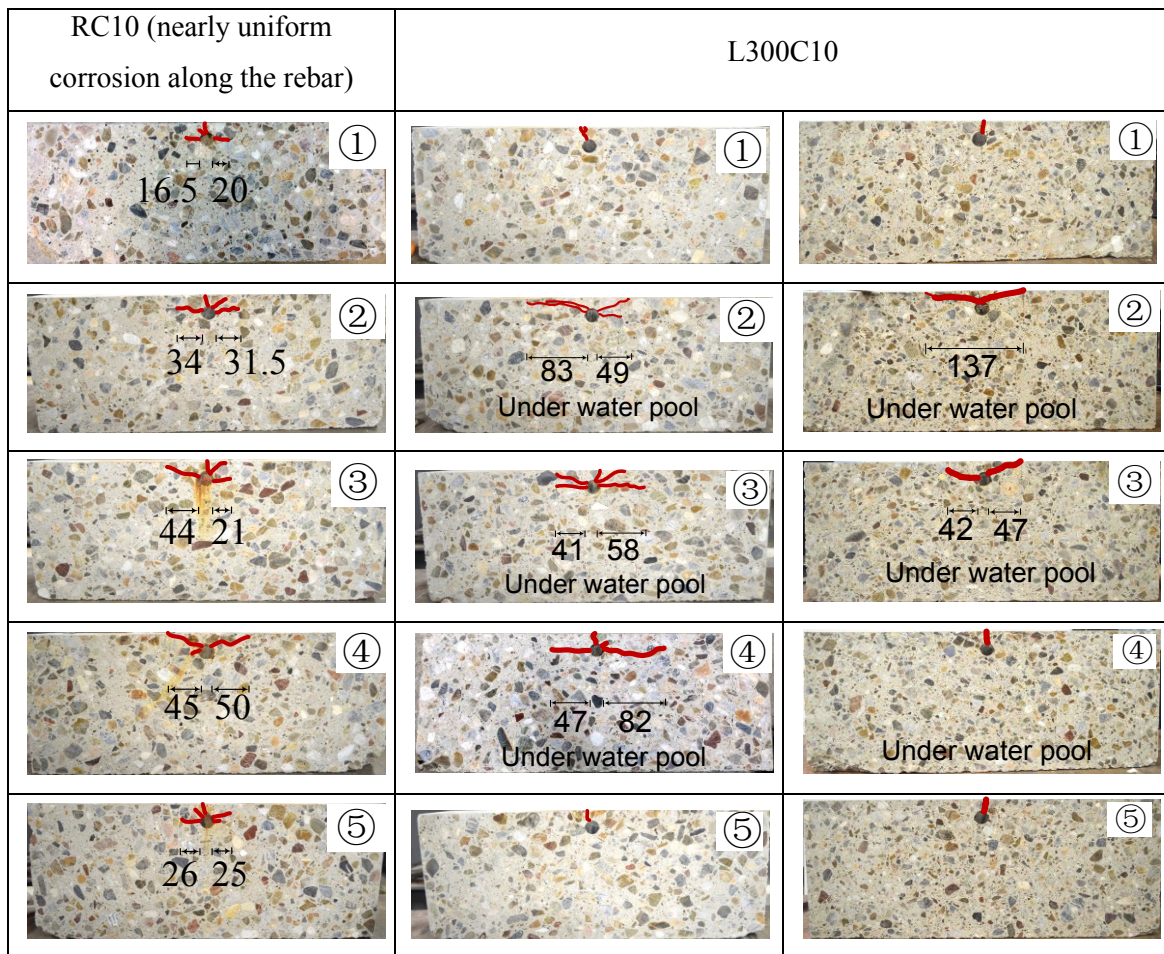
The surface crack patterns of the specimens with 10mm concrete cover are shown in Figure 4.7. In each specimen, a longitudinal crack can be found, suggesting a vertical crack occurring inside concrete. Similarly, the surface crack width at the center part is smaller than that at the area outside the salt-water pool. However, there are a number of cracks (marked in blue) appearing around the pool compared with the cases with 30mm cover. Moreover, a part of concrete is already detached from the bulk specimen of L300C10_2. It indicates that spalling may be more easily generated with a small concrete cover.



Unit: mm


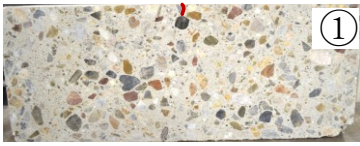

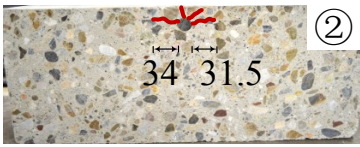
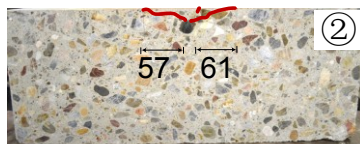
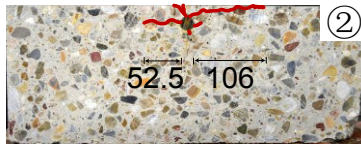

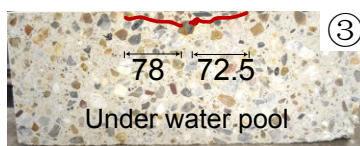
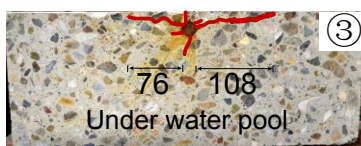


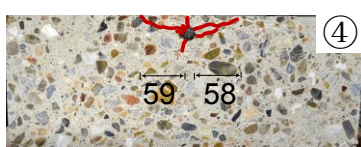


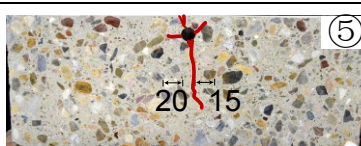
Figure 4.7 Surface crack patterns of test specimens with 10mm cover

Unit: mm



(a) L300C10

Figure 4.8 Internal crack patterns of test specimens with 10mm cover

RC10 (nearly uniform corrosion along the rebar)	L100C10	
		
		
		
		
		

(b) L100C10

Figure 4.8 Cont.

A comparison of internal crack patterns between the specimens with 10mm cover is shown in Figure 4.8. Concentrated corrosion at the center part causes a similar change of internal crack pattern to that occurred in the cases of 30mm cover. Vertical cracks appear in the area outside the salt-water pool alone, while lateral cracks are dominant in the part under the pool. The inclined lateral cracks can also be confirmed at the area with a high corrosion degree, demonstrating a possibility of cover spalling.

The experimental results suggest that when corrosion comparatively concentrates at the local area, internal crack pattern may vary along the rebar length. In the region where corrosion level is relatively high, the lateral crack inside concrete appears to incline to concrete surface, which would form cover spalling with a vertical crack or another lateral crack that propagates diagonally to the concrete surface. In order

to clarify such phenomenon, a numerical analysis based on the corrosion-expansion model is carried out on the same cases.

4.4 Analysis outlines

In the experiment, the rebars are corroded variably in the length direction. To simulate 3D cracks propagation caused by such uneven corrosion, the corrosion amounts along the rebar are predefined in the analysis based on the measured ones. A simple trapeziform corrosion pattern along the rebar length is assumed as shown in Figure 4.9, in which the flat part with a high corrosion level represents the area under salt-water pool. In the analysis, the expansion pressure due to rebar corrosion is simulated using the initial strain problem with an increment of free increase of rebar radius in each step. The accumulative radius increase for a rebar element is determined by predefined local corrosion degree using Equation (3.3), which is dependent on the position along the rebar.

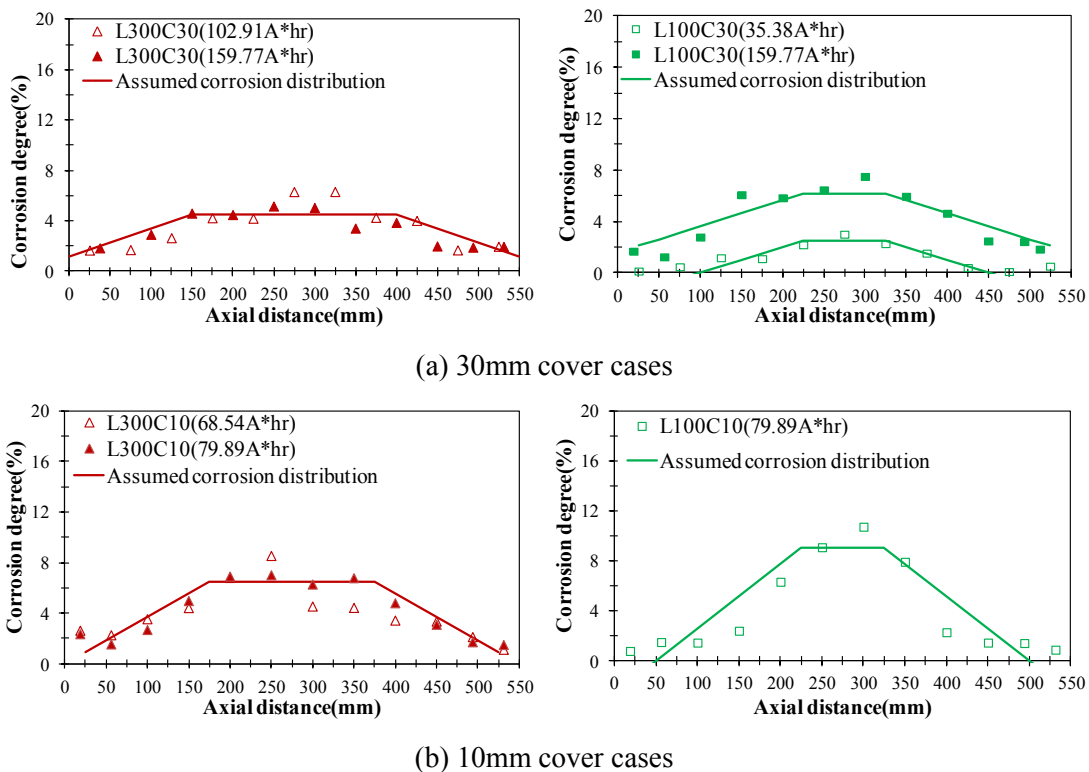


Figure 4.9 Assumed corrosion distributions for analysis

In the circumferential direction of rebar, non-uniform corrosion process is assumed that when a vertical crack with a width greater than 0.1mm appears near a rebar portion, corrosion only distributes on the upside of this portion facing the concrete cover. This assumption corresponds to the corrosion states observed at different positions in the test (see an example in Figure 4.10). The parameter θ of the corrosion-expansion model representing the corrosion distribution around the rebar is set as 90° and 180° for the cases with 30mm and 10mm cover respectively, which is based on the model verification presented in Chapter 3.

The RBSM models created as shown in Chapter 3 (see Figure 3.11) are employed in the analysis.

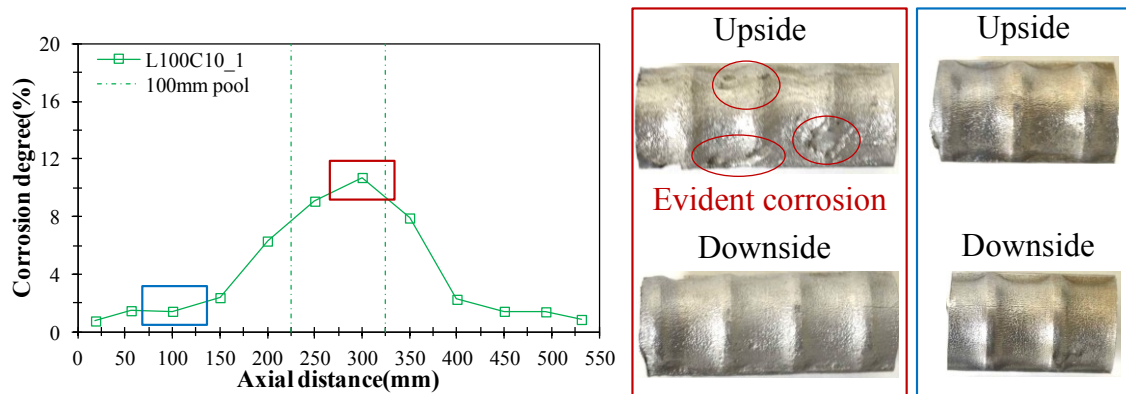
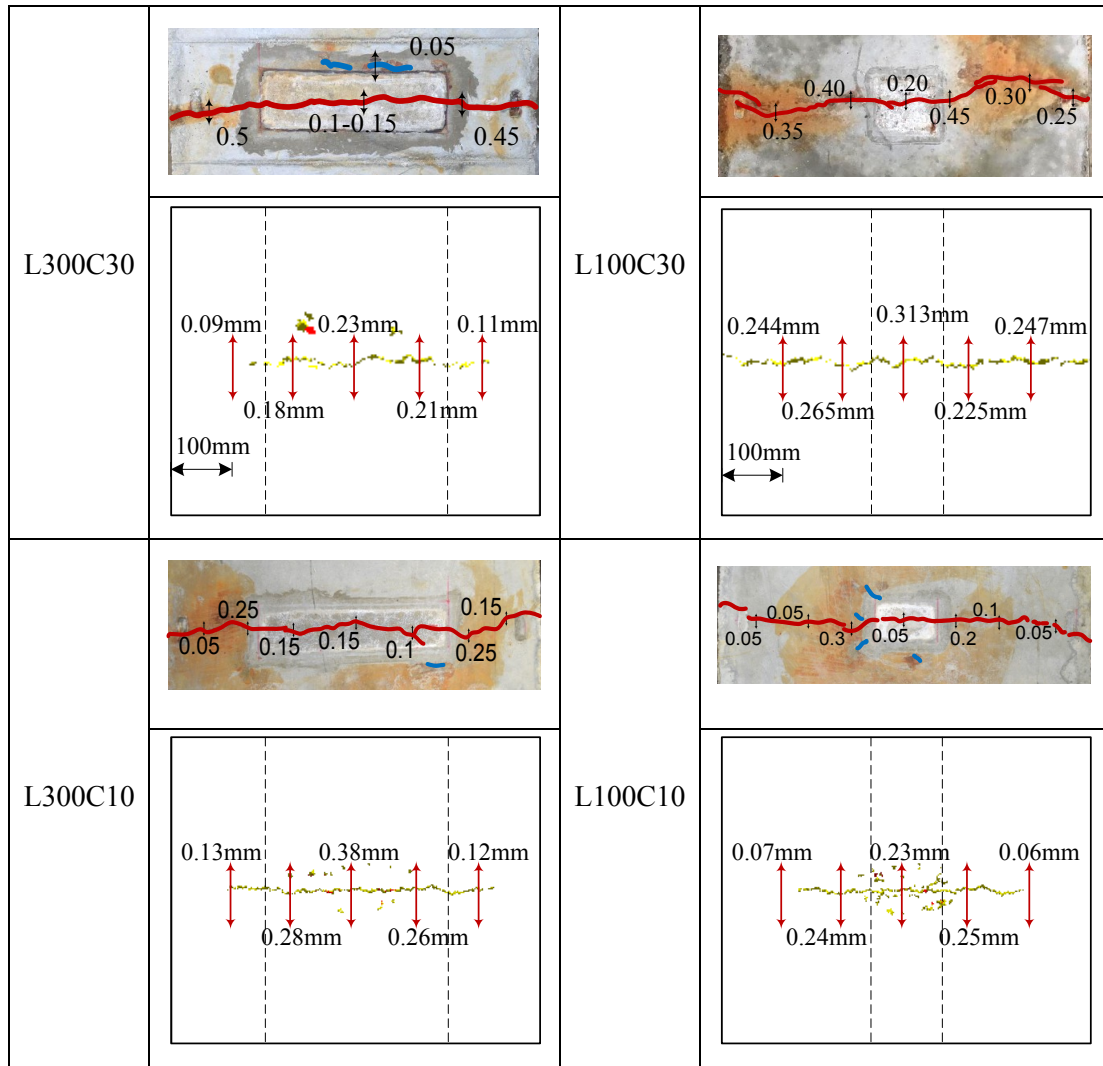


Figure 4.10 Corrosion states around rebar at different positions in test

4.5 Analytical results and discussions

The surface crack patterns of different cases under the predefined corrosion distributions are shown in Figure 4.11. Different colors are used to indicate the crack width value, i.e. the green, yellow and red ones represent the cracks with widths greater than 0.05, 0.1 and 0.3mm respectively. The simulated surface crack patterns are similar to the test results. A longitudinal crack with varied crack widths at different positions can be confirmed in the analysis. For 10mm cover cases, there are also a number of small cracks appearing in the area where salt-water pool locates, apart from the main crack. However, it seems that in both cases with different cover thicknesses the width

values of cracks locating outside the region with the pool are rather smaller than those of cracks at the center part. The reason for this difference with the test results is not clear and needs to be investigated in the future works.



Noted: -----Position of salt-water pool

Figure 4.11 Simulated surface crack patterns for local corrosion

Figure 4.12 shows a comparison of the internal crack patterns between different simulated cases, in which five cross sections with a distance of 100mm are examined, corresponding to the observed sections as shown in Figure 4.3. Lateral crack length is measured from the side of the rebar to the tip of a visible lateral crack wider than 0.1mm. Similar to the test results, the modeled internal crack patterns change with the observed

sections. For both cases with different cover thicknesses, only in the area near the salt-water pool do the lateral cracks have a great evolution. Furthermore, the cases with 30mm cover show that a lateral crack propagates in a diagonal way and almost reaches the concrete surface. In the cases with 10mm cover, two wide inclined cracks appear. The inclined cracks together with the vertical crack can form a fracture plane causing concrete spalling. These results agree with the experimental results, which can prove that a concentrated corrosion along the rebar may lead to cover spalling due to the occurrence of inclined internal crack.

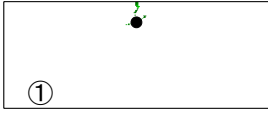
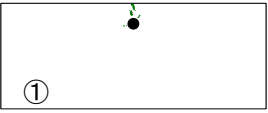
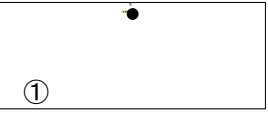
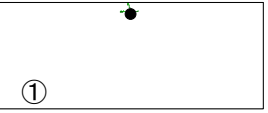
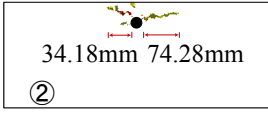
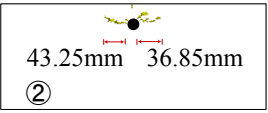
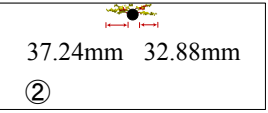
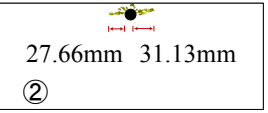
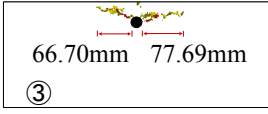
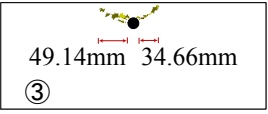
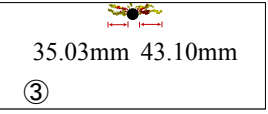
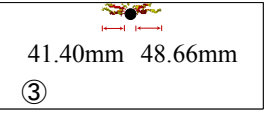
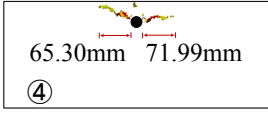
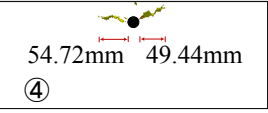
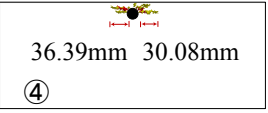
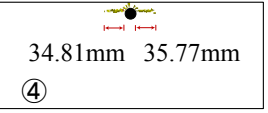
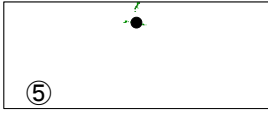
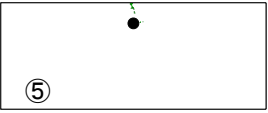
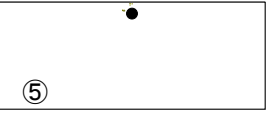
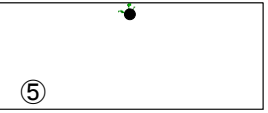
L300C30	L100C30	L300C10	L100C10
 ①	 ①	 ①	 ①
 34.18mm 74.28mm ②	 43.25mm 36.85mm ②	 37.24mm 32.88mm ②	 27.66mm 31.13mm ②
 66.70mm 77.69mm ③	 49.14mm 34.66mm ③	 35.03mm 43.10mm ③	 41.40mm 48.66mm ③
 65.30mm 71.99mm ④	 54.72mm 49.44mm ④	 36.39mm 30.08mm ④	 34.81mm 35.77mm ④
 ⑤	 ⑤	 ⑤	 ⑤

Figure 4.12 Simulated internal crack patterns for local corrosion

The study of 2D cracking behavior has demonstrated that internal crack propagation is related to concrete surface deformation. Hence, the situations of surface deformation under the assumed corrosion distribution as shown in Figure 4.9 are examined to clarify the mechanism of inclined internal crack. Figure 4.13 compares the surface deformations between different analytical cases on the basis of a corrosion level

of 3%. The cases considering uniform corrosion along the rebar length are also included for comparison. A similar phenomenon can be found in the analysis despite of different cover thickness. When local corrosion occurs, under the same level of corrosion, surface deformation area becomes smaller than that of uniform corrosion. The distributions of surface deformation at three different places corresponding to the cut sections of ①, ② and ③ (see Figure 4.13) are investigated in detail as shown in Figure 4.14.

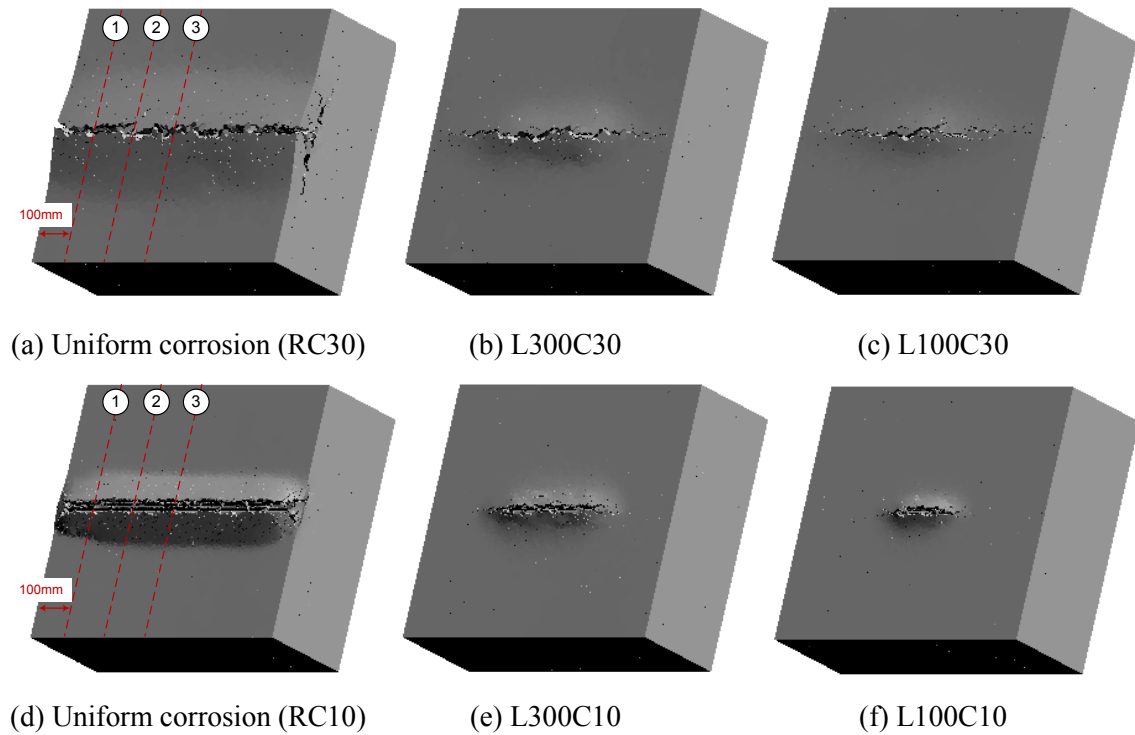
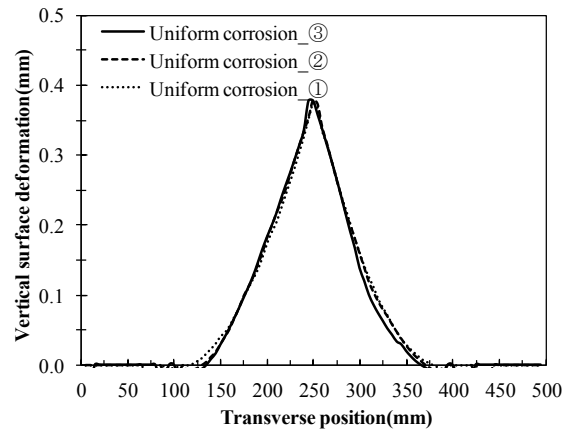


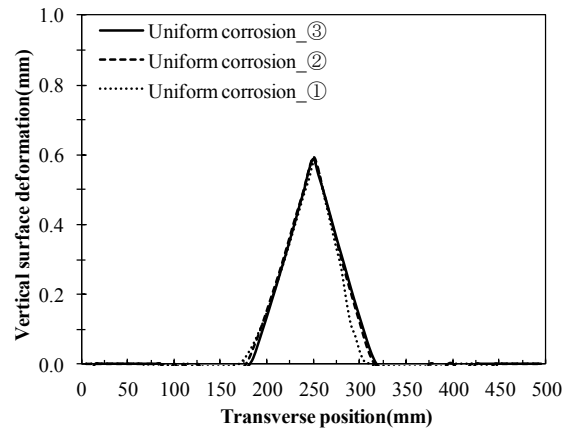
Figure 4.13 Deformation under various corrosion distributions (magnification $\times 50$) 3% corrosion

As can be seen, under uniform corrosion along the rebar length the concrete surface deformation at three different places is consistent with each other, while in the case of local corrosion the surface deformation at the area where rebar corrosion degree is lower (section ①) is significantly smaller than that with a higher corrosion extent (section ③). This inconsistency results in a confinement of deformation at the center part of the concrete specimen, which is shown by a decrease of deformation area in the transverse direction as well as a reduction of maximum value compared with those in

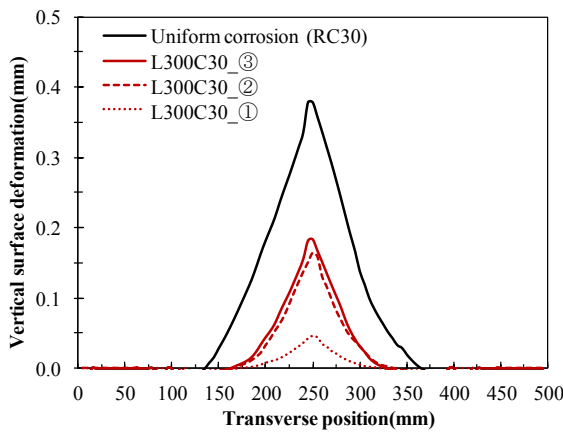
uniform corrosion case. Consequently, lateral cracks become inclining to the concrete surface.



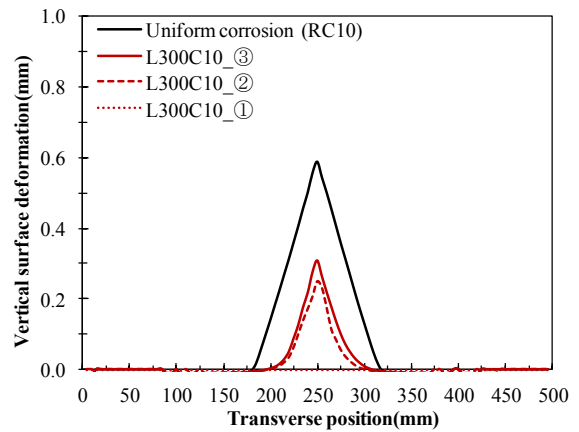
(a) Uniform corrosion RC30



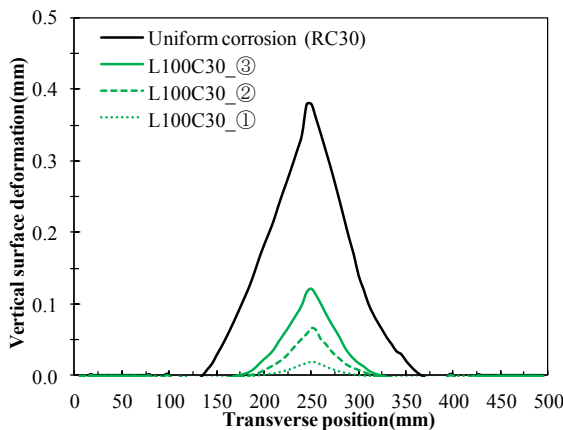
(d) Uniform corrosion RC10



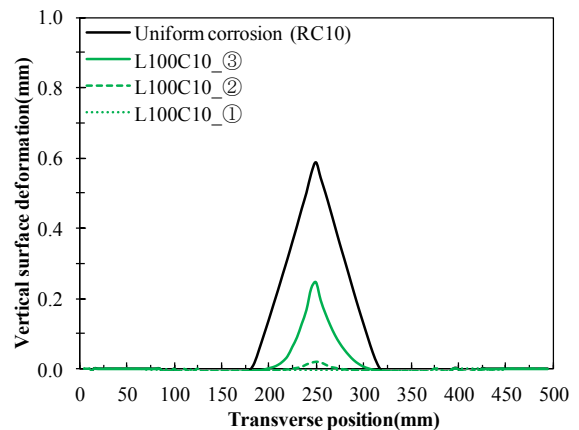
(b) L300C30



(e) L300C10



(c) L100C30



(f) L100C10

Figure 4.14 Concrete surface deformation caused by various corrosion distribution

The corrosion-expansion model can simulate reasonable three-dimensional cracking behavior in terms of surface crack and internal crack patterns in comparison with the experimental results. The model is further employed to evaluate the spalling area. In the analysis, the same corrosion distribution as the one described in Figure 4.9 is assumed and the corrosion level of the part under salt-water pool is increased to 7.5%.

Figure 4.15 shows the surface crack and internal crack patterns for different study cases, in which internal crack patterns are those observed on the cutting sections illustrated by dash lines in the same figure. As can be seen, provided with more corrosion products, the widths of inclined lateral cracks within the area under salt-water pool become much larger (see the red cracks with a width greater than 0.3mm). Accordingly, on the concrete surface the small cracks formed due to development of inclined lateral cracks appear to be wider, which may eventually lead to cover spalling. Comparing the spalling area between different cases, it seems that spalling area is related to the length of the local corrosion region along rebar and affected by cover thicknesses. The two cases with different cover thicknesses both show that a longer salt-water pool (300mm) leads to a larger spalling area, suggesting that when rebar corrosion concentrates at the local area, at the same level of corrosion that is sufficient for cover spalling, the longer corroded area tends to induce a larger spalling area. On the other hand, spalling may be more severe in a thick concrete cover (30mm), since the inclined lateral cracks would be longer.

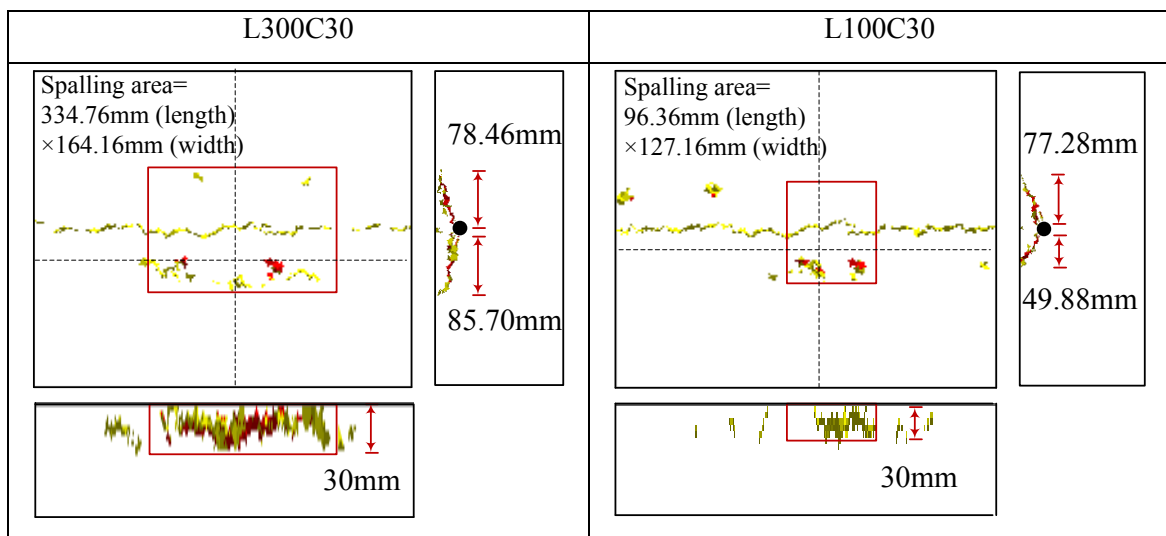


Figure 4.15 Evaluation of spalling area

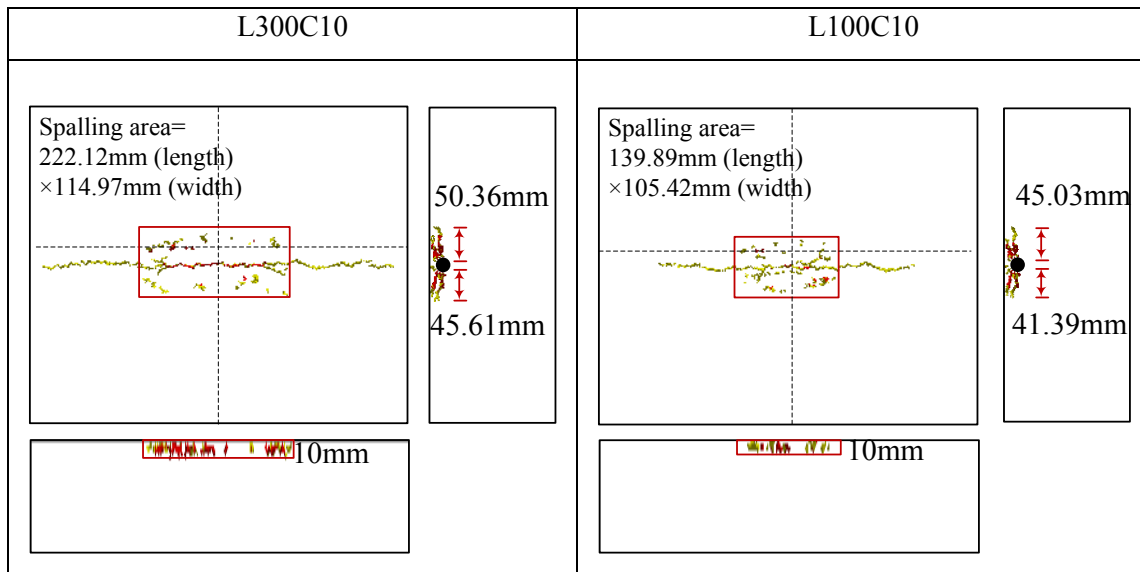


Figure 4.15 Cont.

4.6 Summary and conclusions

The objective of this chapter was to study 3D crack propagation and cover spalling caused by local corrosion along the rebar. To achieve that, local corrosion was simulated in the experiment by electric corrosion method, in which salt-water pools of various sizes were used. The distribution of corrosion degrees measured in the test has confirmed that using a small pool can concentrate corrosion within the rebar part under the pool. Both study cases with varied cover thicknesses of 10 and 30mm demonstrate that the internal crack patterns resulting from such local corrosion vary along the rebar length. At the area with concentrated corrosion, lateral crack inclines to the concrete surface rather than propagate horizontally as shown by 2D cracking behavior, triggering cover spalling. Outside this area, vertical cracks dominate in the internal crack pattern.

The corrosion-expansion model was applied to analyze crack development by using the fit curves of measured corrosion distribution. A satisfied agreement with the test results has been obtained in internal crack patterns. The analysis indicates that the inclined lateral crack is possibly due to the confinement of concrete surface deformation by the other part of concrete with less rebar corrosion.

An evaluation of spalling area suggests that local corrosion distributing within a longer range of rebar potentially causes a bigger spalling area in the slab concrete cover and the spalling damage may be more severe in a thick concrete cover.

5 Experimental Investigation of Tensile Behavior of Corroded Rebars

5.1 Introduction

Corrosion of reinforcement not only causes concrete cracking and spalling, but also leads to a decrease of tensile capacity of rebar due to a loss of bar section. From Chapter 5, the latter form of corrosion-induced damage is investigated. With regard to this problem, there are a number of experimental studies reported in literature. In the studies, although the rebar specimens tested had been exposed to different kinds of corrosion, including natural corrosion (Papadopoulos et al. 2011, Zhang et al. 2012), accelerated electric corrosion (Almusallam 2001, Cairns et al. 2005, Du et al. 2005) and artificial corrosion by salt spray (Papadopoulos et al. 2007, Lee and Cho 2009), a common conclusion could be drawn that corrosion might result in a relatively modest decrease of yield and ultimate strengths but a significant loss of ductility. In order to estimate the residual tensile capacity of corroded rebars, some empirical equations with a similar form based on average corrosion degree or average section loss have been proposed (see Equation (1.1)). However, the empirical coefficient α , which is determined in the experimental studies for residual tensile capacity, varies with each other. It is likely to be influenced by varied corrosion topographies resulting from different corrosion methods. Natural chloride-induced corrosion characterized by localized corrosion along the rebar length tends to cause a greater loss of rebar tensile performance than accelerated electric corrosion that is more uniform (Zhang et al. 2012). Hence, a better method on the basis of corrosion topography is keenly required for an accurate evaluation of tensile behavior of corroded rebars.

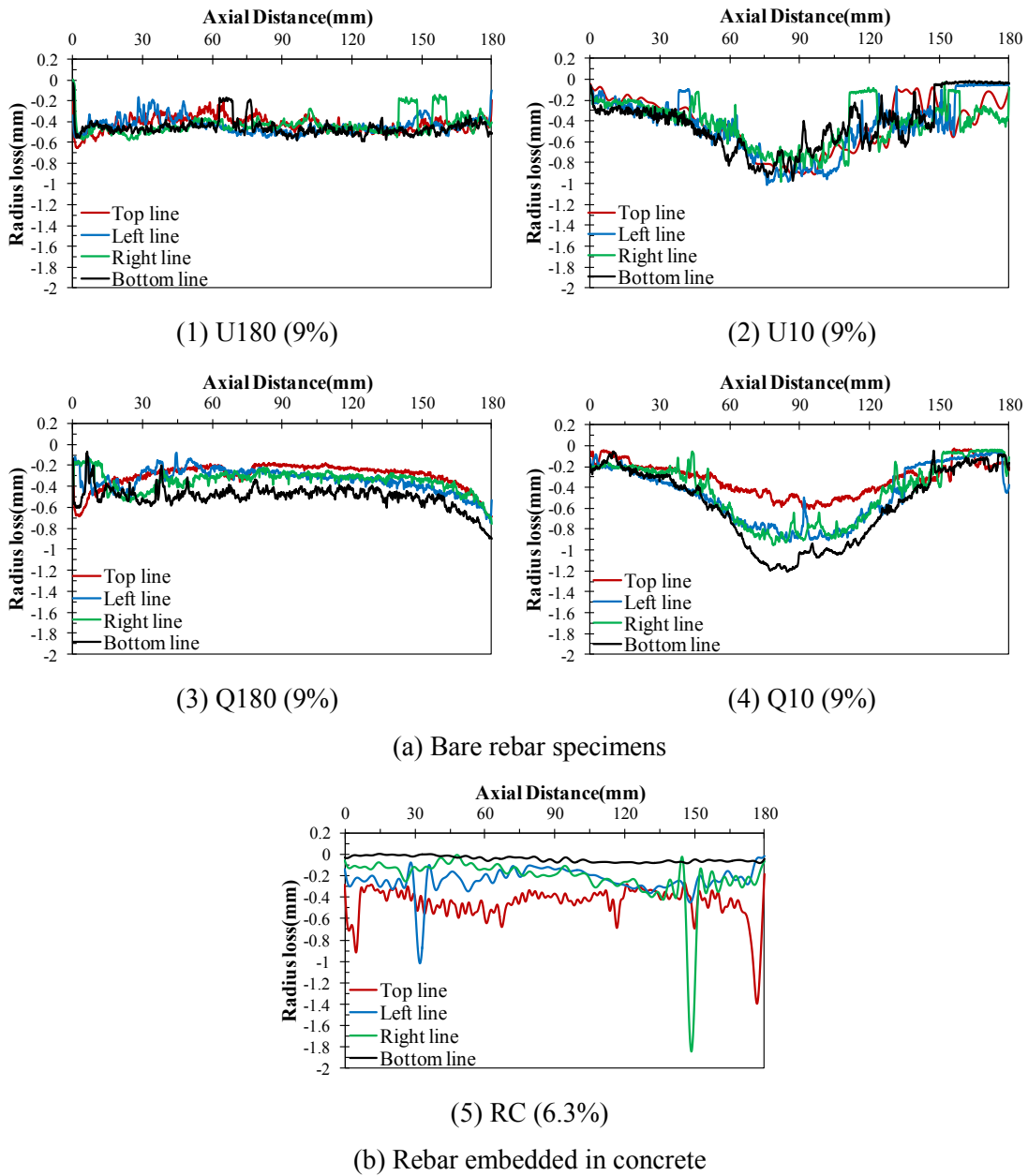
This chapter presents an experimental study into the relation between corrosion topography and residual tensile capacity of corroded rebars, where a type of plain round rebar is used. Various corrosion profiles represented by radius losses along the rebar were considered by the proposed corrosion method, including circumferentially uniform and non-uniform corrosion and local corrosion along the length of the rebar. The rebar specimens tested were prepared with the electric corrosion method as introduced in Chapter 2. Both bare rebar specimens and those corroded in concrete were tested under a static tensile loading, in which a digital image processing method was used to obtain the strain history. The experimental results presented herein provide essential data for the establishment of a quantified evaluation method that is to be shown in Chapter 6.

5.2 Test series

The rebar specimens used in the test belong to the same type of plain round rebar SR235 (JIS 2010) with yield strength greater than 235MPa and ultimate strength greater than 380MP. The specimens all have a length of 600mm and an initial diameter of 16mm. For a corroded specimen, the corroded area only distributes at the center part of the rebar with a length of 180mm. The conditions of rebar specimens are summarized in Table 5.1 in which average corrosion degree is calculated over 180mm long corroded area. For each test series, three samples were used.

Table 5.1 Test series for tensile performance of corroded rebars

		Test series	Corrosion pattern	Average corrosion degree
Bare rebar	Uniform case	U180	Uniform	3%, 9%, 15%
		U100, U40, U10	Longitudinally localized	3%, 9%, 15%
	Quarter case	Q180	Circumferentially non-uniform	9%
		Q10	Non-uniform + localized	9%
Rebar in concrete		RC	Circumferentially non-uniform	0.65%, 1.82%, 3.2%, 5.2%, 6.3%



Noted: corrosion degree shown in parentheses

Figure 5.1 Typical corrosion profiles of rebar specimens in tensile testing

The corrosion patterns listed in Table 5.1 are explained by typical corrosion profiles of rebar specimens as shown in Figure 5.1. In the case of U180, corrosion distributes uniformly in both circumferential and longitudinal direction, while for the specimens of Q180 and RC non-uniform corrosion occurs around the rebar. In the case

of U10 and Q10, corrosion concentrates at the center part of the rebar, which is considered as a representation of local corrosion.

5.3 Uniaxial tensile tests and digital image processing

Tensile tests of non-corroded and corroded specimens were carried out with a universal testing machine. The tensile testing length from the upper chucked point of a test specimen to the lower one was 400mm, within which the 180mm long corroded zone was included. Five strain gauges with a length of 2mm were attached to the corroded zone with a spacing of 40mm along the length of the specimen to investigate the developments of local strains. The applied load with a speed of 250N/s and the corresponding strains were automatically recorded with a data collecting and processing system. However, using this technique, it is difficult to obtain a complete strain history up to specimen fracture due to the limited measurement range of strain gauges. The strain gauges are also likely to be debonded from the specimens because the corroded surface is not smooth. Thus, a digital image processing method was also used in the tensile tests.

The image processing method usually used in such cases, called the digital correlation method (Sutton et al. 1983, Wang et al. 2010), provides data on the in-plane deformation of an object. In this method, images are continuously recorded during deformation and are correlated with the initial image by matching intensity patterns. A speckle pattern is painted on the surface being studied and, using bilinear interpolation, displacements as small as 0.10 pixels can be measured (Sutton et al. 1983). However, a different image processing method was used in this case, whereby the correlation is established using distinguishable marks instead of an interpolated intensity distribution. Since no complicated algorithm is involved in this proposed method, processing time and memory can be saved.

To make the distinguishable marks, the side of the specimen opposite the one with strain gauges was fitted with eight round red spots of diameter 5mm. Two additional spots located at the bottom were used to compensate for extra displacements caused by vibrations. During the tensile tests, a digital camera aimed perpendicularly at the face with spots were used to capture sequential images with a resolution of $4000 \times$

6016 pixels at an interval of 5 seconds, resulting in about three hundred images for each test specimen. The experimental setup is shown Figure 5.2.

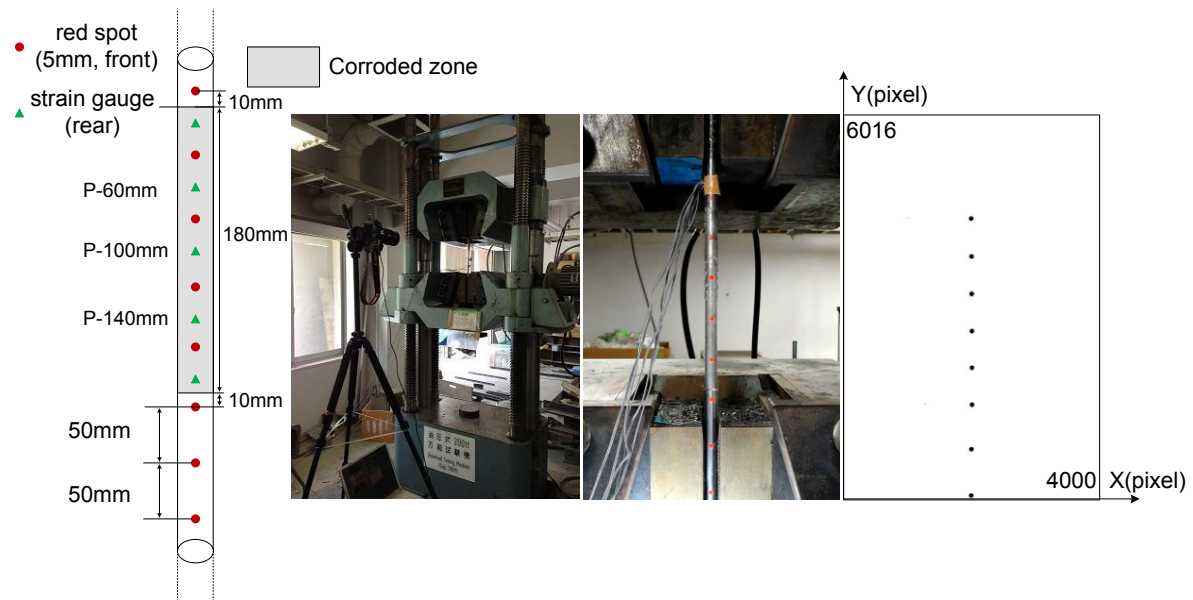


Figure 5.2 Tensile test setup

The proposed digital image processing method was used to acquire displacements of the red spots and thereby calculate engineering strains. This process is explained in detail below.

Firstly, the captured images were transformed into binary images to identify all the spots: i.e. the color value of pixels composing the spots was set to 0 and other pixels to 255 (see Figure 5.2). Then a plane coordinate system based on a pixel scale was defined for the binary images, where the bottom left was set as the origin. By comparing the coordinates of the spot centers in each binary image, displacements of the spots can be determined. Finally, the engineering strain can be calculated as the ratio of the extension between two adjacent spots to the initial spacing.

The precision of this image processing method depends on the pixel size (the length represented by a pixel in practice), which varies with the area of the image occupied by the object under study. The spot diameter of 5mm and the spacing of 40mm were confirmed in the experiment to be able to obtain an accurate strain distribution, by which the detectable displacement can be as small as 0.068mm. The stress-strain

relationships obtained separately by the strain gauges and the image processing method are compared in Figure 5.3, in which the U10-9% series is taken as an example and the measuring positions are explained in Figure 5.2. The stress was derived through dividing the tensile load by the nominal cross-sectional area. As can be seen, the results from the image processing method are similar to those from strain gauges. The image processing method is able to provide a complete strain history until specimen fracture.

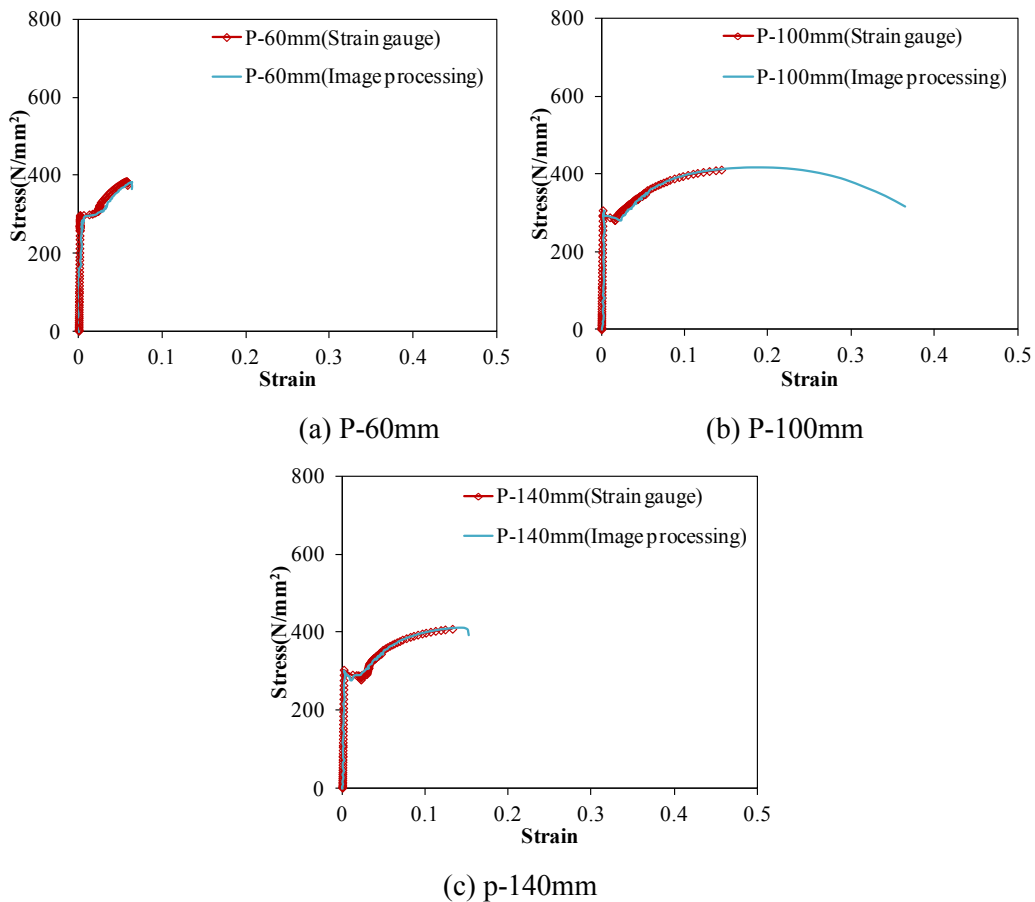


Figure 5.3 Comparison of local stress-strain relationships obtained by strain gauges and image processing method (U10-9%)

5.4 Tensile test results

The stress-strain relationships for non-corroded and corroded specimens show the same pattern. The ultimate strains corresponding to the rebar specimen fracture at

three different measuring positions as shown in Figure 5.2 are 0.12, 0.5 and 0.19 respectively for non-corroded specimen, while their values are 0.1, 0.37 and 0.14 respectively for the corroded specimen U10-15%. They both show that the strain differs along the rebar length and only at the center that is the fracture part does the strain continue to increase in the post-peak stage, as shown in Figure 5.3. It appears that the properties of the steel may not be affected by corrosion, which is in agreement with the views of Palsson and Mirza (2002) as well as Cairns et al. (2005). However, the ultimate strain at the specimen center decreases significantly. For the U10 series, its value falls from 0.44 to 0.37 as the average corrosion degree increases from 3% to 15%.

In order to evaluate the effects of different corrosion profiles on the degradation of tensile performance, the yield and ultimate load were investigated in detail. The residual tensile capacity of corroded specimens, in terms of the yield and ultimate loads, and their elongation were determined as a ratio by dividing the test results by the results for the non-corroded specimens. Elongation was calculated based on deformation of the fracture zone, which had an original length of 128mm, i.e. 8 times the diameter of the non-corroded specimen (JIS, 2011).

For clarification of the effect of various corrosion states in the rebar circumferential direction, a comparison was made between the test series of RC, Q180 and U180 (see Figure 5.4). In these specimens, corrosion occurs consistently along the 180mm long corroded area, i.e. the corrosion amounts at different positions along the rebar length are similar. As can be seen, the tensile performance of these specimens decreases nearly in a linear way with an increase of corrosion degree. When average corrosion degree reaches 9%, the yield and ultimate load may be reduced by 7.2% and 11.9% respectively. It appears that different radius losses in the circumferential direction presented in RC and Q180 (see Figure 5.1) hardly change the residual tensile capacity when compared with that of U180. This can be ascribed to the similar residual cross-sectional areas along the length of the specimens. However, when concentrated corrosion occurs in the rebar length direction (see U10 and Q10 in Figure 5.4), there is an obvious larger reduction of tensile performance. It suggests that residual tensile capacity of corroded rebars may be affected by variability of corrosion along the rebar length rather than that in circumferential direction.

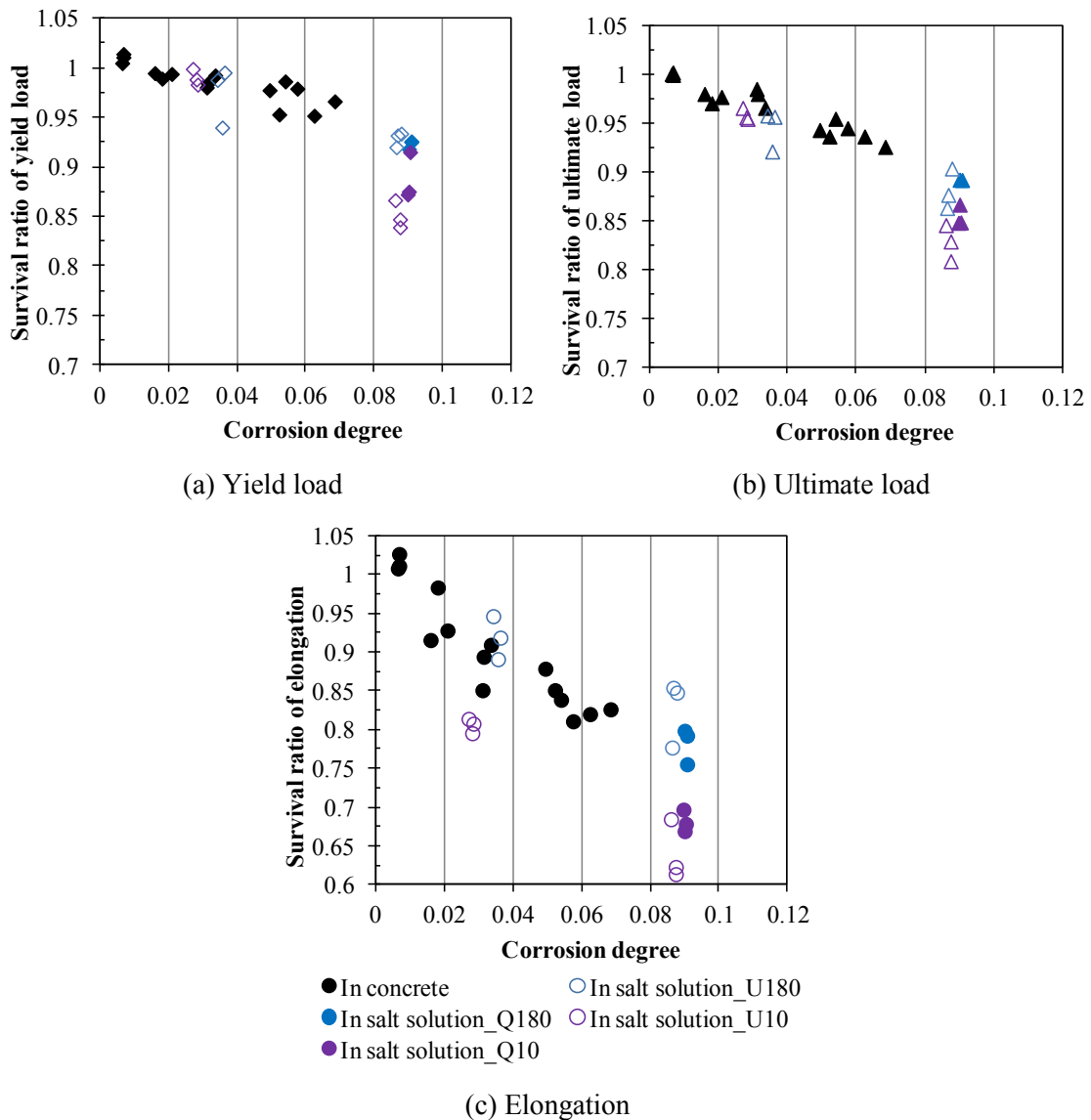


Figure 5.4 Effect of circumferential corrosion state on tensile performance

A comparison of the series with various radius losses along the length of the rebar is shown in Figure 5.5. It is clear that when corrosion is concentrated on the center part (see U10) performance degradation becomes more severe even for the same corrosion degree. In the case of 15% corrosion, the yield and ultimate load may be reduced up to 18% and 23.5% respectively when corrosion distributes within a small area. Empirical equations that are recommended based on average corrosion degree in other experimental studies (Lee and Cho 2009; Zhang et al. 2012) are employed to predict the residual strengths of the studied specimens, as also shown in Figure 5.5. It

appears that the empirical equations only work well with specimens corroded more uniformly in the length direction (U180 and U100), which implies that the accuracy of the empirical equations is sensitive to coefficient α as expressed in Equation (1.1). The corrosion profile needs to be considered when evaluating the tensile behavior of corroded rebars.

The test results also indicate that the ultimate load decreases at a higher rate than the yield load, and elongation is the most affected property. This may result in a higher risk of brittle failure.

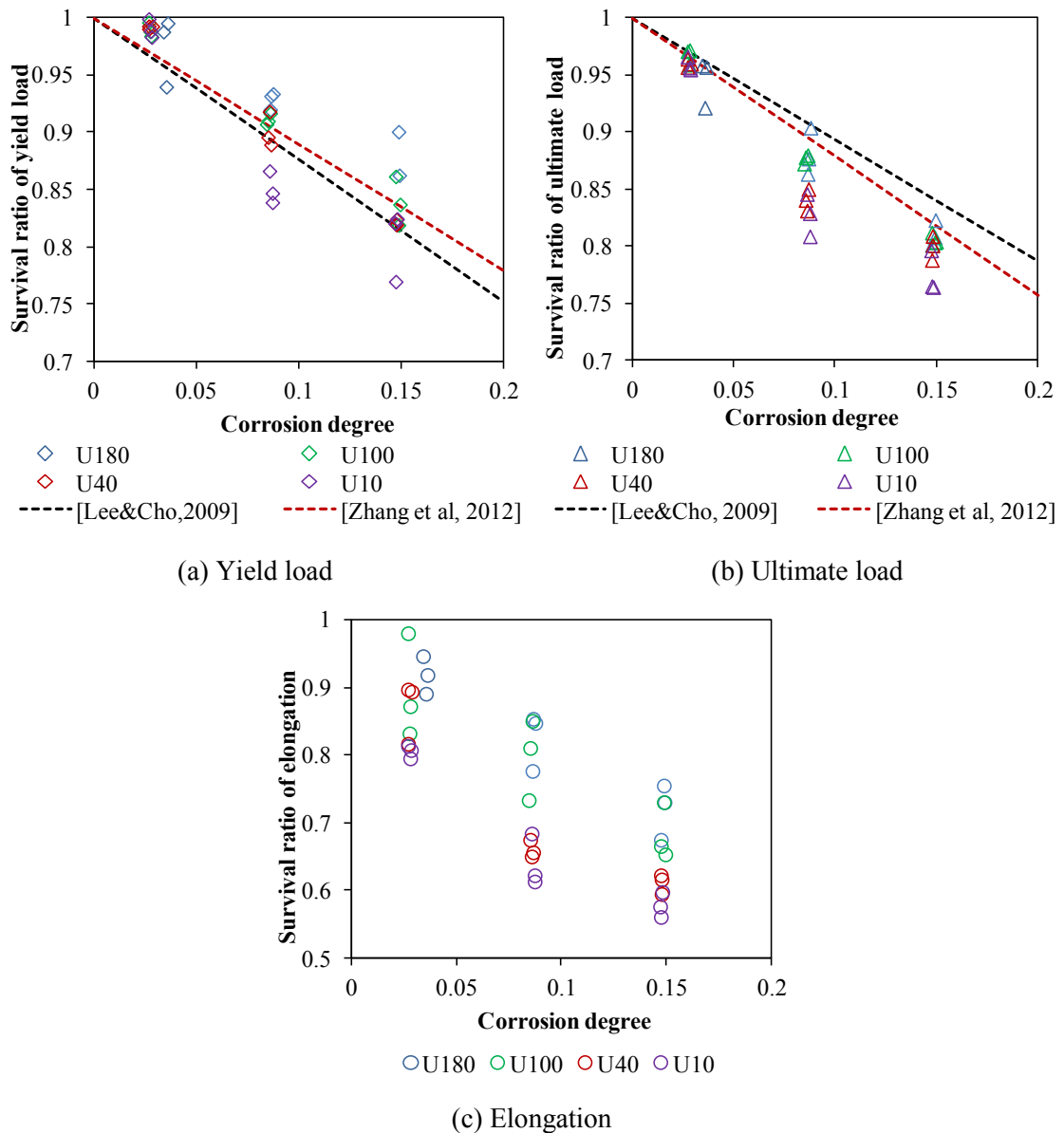


Figure 5.5 Effect of longitudinal corrosion state on tensile performance

5.5 Summary and conclusions

The tensile behavior of plain round reinforcing bars corroded with various corrosion profiles is investigated experimentally to study the effects of different corrosion profiles on tensile degradation and to obtain data with which to build a quantified evaluation method. In the tensile test, a digital image processing method is applied to record the development of local strain and to obtain a complete strain history, which yields satisfactory accuracy. The test results show that with corrosion the ultimate load of a rebar specimen decreases more than the yield load and elongation is most affected, which may increase the risk of brittle failure in the case with a high corrosion level. The residual tensile capacity of corroded rebars is closely related to variability of radius loss along the length of the rebar. Concentrated corrosion would lead to a more tensile degradation. On the other hand, varied corrosion patterns in the rebar circumferential direction seem to have less influence on the rebar tensile performance.

6 Evaluation Method of Tensile Performance of Corroded Rebars

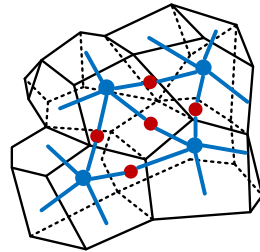
6.1 Introduction

For estimating the residual tensile capacity of corroded rebars, the empirical equations based on average corrosion degree or average section loss (Cairns et al 2005, Du et al. 2005, Lee and Cho 2009, Zhang et al. 2012) are often used. However, the experimental study carried out in Chapter 5 suggests that the residual tensile performance is largely related to the corrosion profile that is to radius losses along the length of the rebar. The applicability of these equations is limited to the rebar with specific corrosion topography similar to that of the tested one. Comparatively, a numerical model taking into consideration corrosion profile may be a better option. Moreover, since the expansion pressure caused by corrosion products in concrete can be predicted well from rebar radius loss (Lundgren 2002), the numerical model can be integrated into the corrosion-expansion model (Tran et al. 2011), by which both concrete crack propagation and the loss of rebar tensile capacity can be considered. Such a model would be contributable to the assessment of RC structures damaged by corrosion.

In this chapter, the numerical model that accounts for corrosion profile is developed to accurately evaluate the tensile degradation. The RBSM is combined with a truss network to compute the radius losses of corroded rebars using the Laplace equation and Faraday's law, and then evaluate their tensile behavior. The applicability of the proposed model is verified by comparisons to the experimental results of bare rebar specimens (see Table 5.1) since they demonstrate a clear relationship between rebar tensile degradation and corrosion profile in the test.

6.2 Truss Network

Field-type problems and mass transfer situations that are governed by partial differential equations are usually analyzed with a continuum model, whereas the RBSM as a discrete approach does not require continuity. Hence a truss network (Nakamura et al. 2006) is combined with RBSM to cope with the Laplace equation for the analysis of radius losses along the rebar. The rigid particle elements are linked by truss elements with a node at each nucleus and at intermediate points on each particle boundary (see Figure 6.1). A simplified one-dimensional partial differential equation is applied to the truss elements to carry the potential flow or mass transfer.



Internal truss network

Figure 6.1 Truss network

6.3 Rebar material model

Figure 6.2 shows the stress-strain relationship (Kato 1979) applied for non-corroded rebars. Since the mesh model of the rebar specimen developed for the analysis consists of regular hexahedral elements, shear behavior was neglected in the tensile analysis. The stress-strain relationship is introduced into normal springs to model the tensile behavior, where σ represents tensile stress, E is elastic modulus, ε is strain, ε_y is strain until the yield stage, ε_{sh} is strain until the hardening stage, f_y is yield strength, f_u is ultimate tensile strength and k is a constant dependent on the yield strength.

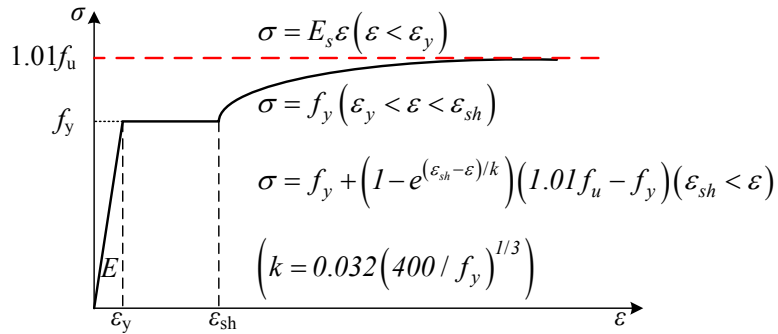


Figure 6.2 Stress-strain relationship of sound rebars (Kato 1979)

The stress-strain relationships used by Cairns et al. (2005), and Lee and Cho (2009) are simply bilinear models. Although their models can approximate actual rebar tensile behavior, it is difficult to accurately calculate the yield and tensile strengths. In this study, the stress-strain relationship described previously is used. The rebar elastic modulus, yield and ultimate strength were set as 218GPa, 318.47MPa and 463.52MPa respectively. The simulated result for a non-corroded specimen is compared to the experimental results in Figure 6.3. As can be seen, the rebar material model shows good agreement with test data.

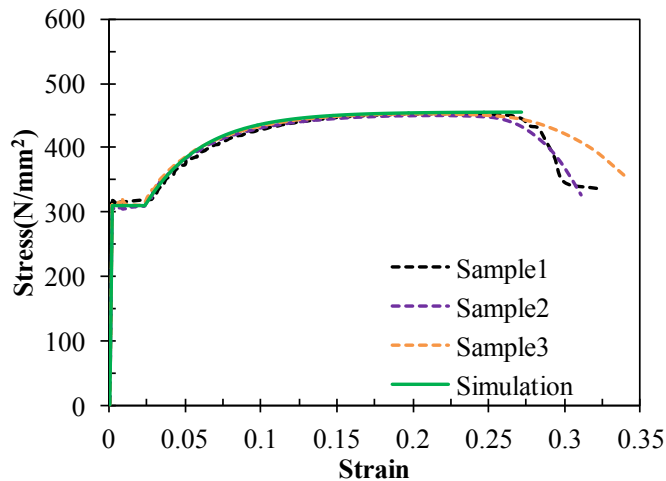


Figure 6.3 Applicability of stress-strain relationship in simulations

6.4 Analytical procedures

Figure 6.4 shows the analytical process flow of the developed numerical model, which is composed of potential distribution analysis using a truss network and tensile simulation by the RBSM. In the first part of the analysis, a three-phase material model consisting of salty water, corrosion products and the rebar is set up with an average element size of 5mm, as shown in Figure 6.5. This model has the same dimensions as the experimental units. In the simulation, considering the regular corrosion profile along the rebar length and the computation efficiency, the length of a divided rebar element was set as 5mm, which is reduced for a more complex corrosion profile, such as that of pitting corrosion. During the corrosion tests, it was observed that the potential difference between the anode and cathode was about 1V. Hence, in the simulation, the potential of the red node (representing the anode) is simply assumed to be 1V, while the boundaries marked in green that represent the cathode are fixed as zero. A zero influx condition is applied on the other boundaries. In the analysis, the current flows calculated are ensured to be consistent with those implemented in the experiment (see Table 2.3).

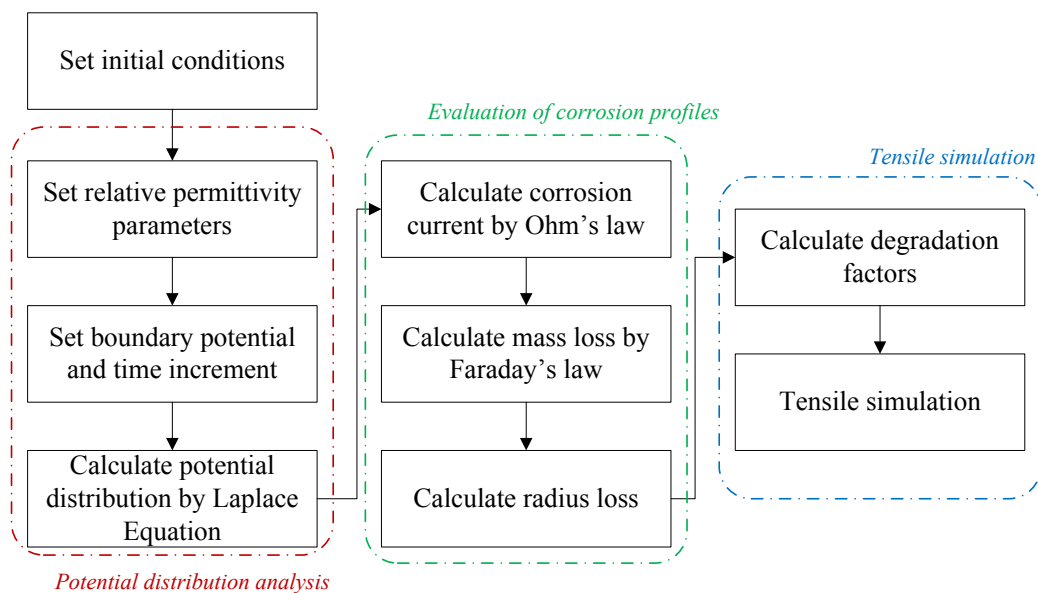


Figure 6.4 Analytical process flow for evaluating tensile behavior of corroded rebars

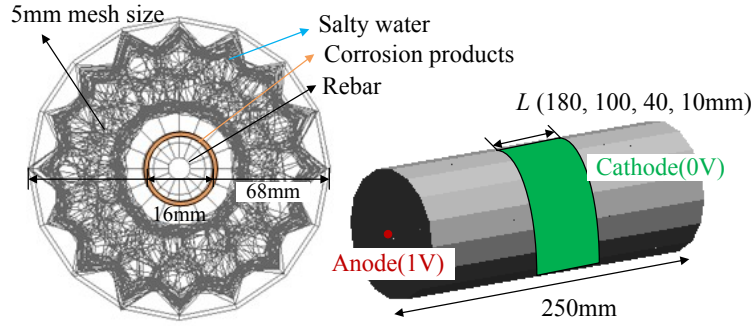


Figure 6.5 Analytical model for analysis of potential distribution

The potential distribution inside the pipe is calculated based on the Laplace equation (Moliton 2007), which is expressed as a matrix (Segerlind 1984):

$$\frac{\partial}{\partial x} \left(\varepsilon_r \cdot \frac{\partial \phi}{\partial x} \right) = 0 \quad (6.1)$$

$$\begin{bmatrix} I_1 \\ I_2 \end{bmatrix} + \frac{A\varepsilon_r}{l} \begin{bmatrix} 1 & -1 \\ -1 & 1 \end{bmatrix} \begin{Bmatrix} \phi_1 \\ \phi_2 \end{Bmatrix} = \begin{Bmatrix} 0 \\ 0 \end{Bmatrix} \quad (6.2)$$

Where Φ_1 and Φ_2 represent the potential at each node of a truss element, respectively, A is the cross-sectional area of the truss element (and is equal to the area of the corresponding facet of a rigid particle element), l is the length of the truss element, ε_r is relative electric permittivity, and I_1 and I_2 are the interelement terms that are depleted in the calculation unless derivative boundary conditions are specified at these nodes (Segerlind 1984). The parameters of relative electric permittivity used in the simulation are listed in Table 6.1. The relative permittivity of rebar is infinite as a conductor, which is accordingly set with a sufficient large value. Regarding corrosion products since no available data could be found, it was obtained by examining several values in the simulation, considering that soluble corrosion products could easily polarize in response to an applied electric field.

Table 6.1 Parameters used in potential distribution analysis (Conyers 2013)

	Salt water	Corrosion products	Rebar
Relative permittivity	88	264	1^{50}

Since only a micro-cell corrosion circuit is involved in the corrosion method used, the corrosion current I_j flowing through each truss element connecting the rebar layer and corrosion products layer can be simply determined with Ohm's law:

$$I_j = \frac{|\Delta\phi| \cdot A}{\rho l} \quad (6.3)$$

Where $\Delta\Phi$ is the potential difference between the two nodes of the truss element and ρ is the electrical resistivity.

Accordingly, the mass loss m_i for each corroded rebar element i is calculated using Faraday's law:

$$m_i = \frac{I_j t M}{n F} \quad (6.4)$$

Where t represents conduction time, M is the molar mass of iron, n is the valency, and F is Faraday's constant.

The local radius loss is determined as a height reduction h_i in the cross-section of each corroded rebar element:

$$h_i = \frac{m_i}{\rho_s A_s} \quad (6.5)$$

Where ρ_s is the density of iron and A_s is the area of the corroded surface of the rebar element, as illustrated in Figure 6.6.

As geometric reductions of the mesh model are not allowed in the simulation, degradation factors derived from local radius losses are introduced into the rebar material model, which is calculated as follows:

$$\alpha_i = \frac{A_{s,tcrr}}{A_{s,t}} = \frac{(h - h_i) \cdot (l_2 + l_3)}{h \cdot (l_1 + l_2)} \quad (6.6)$$

Where $A_{s,t}$ is the original cross-sectional area of each corroded rebar element, $A_{s,tcrr}$ is the residual cross-sectional area, h is the original height of the rebar element (2mm), l_1 is the initial length of the corroded surface (3.14mm), l_2 is the length of the inner surface

(2.36mm), and l_3 is the residual length of corroded surface. An illustration of the method used to calculate degradation factors is presented in Figure 6.6.

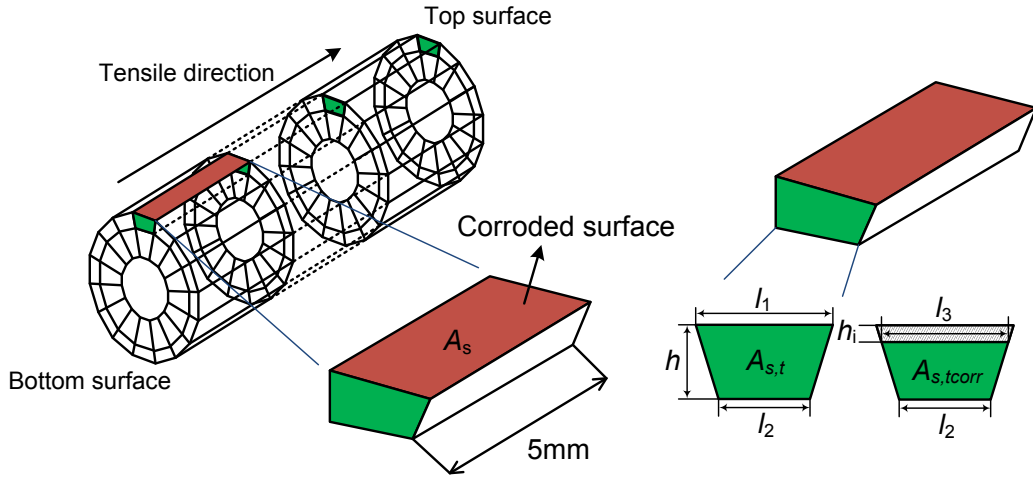


Figure 6.6 Calculation of degradation factors

In the tensile simulation, the material properties of the corroded rebar elements are reduced based on degradation factors:

$$E_{i,corr} = E_i \cdot \alpha_i, \quad f_{y_i,corr} = f_{y_i} \cdot \alpha_i, \quad f_{u_i,corr} = f_{u_i} \cdot \alpha_i \quad (6.7)$$

Where $E_{i,corr}$, $f_{y_i,corr}$ and $f_{u_i,corr}$ are the residual elastic modulus, yield strength and ultimate strength for each corroded rebar element, respectively.

Regarding the boundary conditions for the tensile simulation, the bottom surface is constrained, while the top surface is applied with a fixed vertical displacement in each analysis step.

6.5 Analytical results compared with test data

6.5.1 Corrosion profiles

6.5.1.1 Uniform cases

In the corrosion test of bare rebar specimens as shown in Chapter 2, when corrosion degree reached 15%, some corrosion products adhered to the rebar surface,

possibly affecting the distribution of corrosion current along the rebar (see Figure 2.18). To account for this in the simulation, a simple varied distribution of relative permittivity in the corrosion products layer was assumed in the case of 15% corrosion, instead of the constant value used in the 3% and 9% cases. From the right end of the 180mm long corroded part, a section with a length of 72.5mm was assumed to have a relative permittivity of 264 to represent adhered corrosion products, while the relative permittivity of the left part falls linearly to 88 to represent direct contact with the salty water. The potential distributions in the corrosion products layer under this assumption are compared to those in the case of a constant relative permittivity in Figure 6.7. This makes clear that the potential difference between the rebar layer and the corrosion products layer becomes larger at the left part, which results in a larger corrosion current.

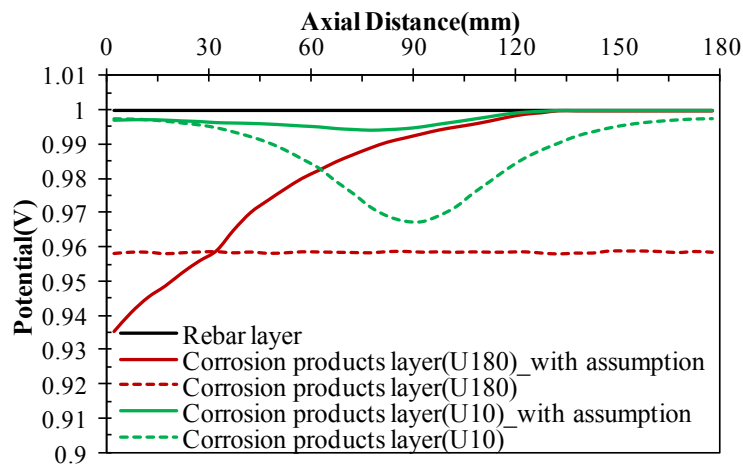
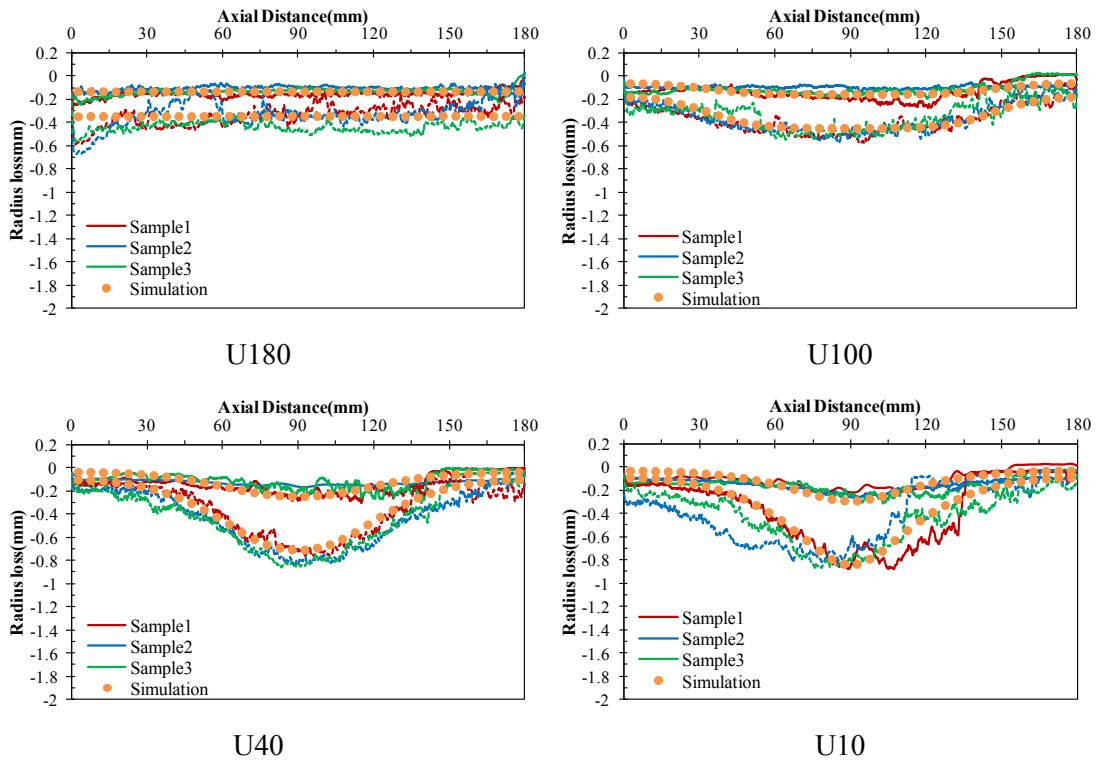
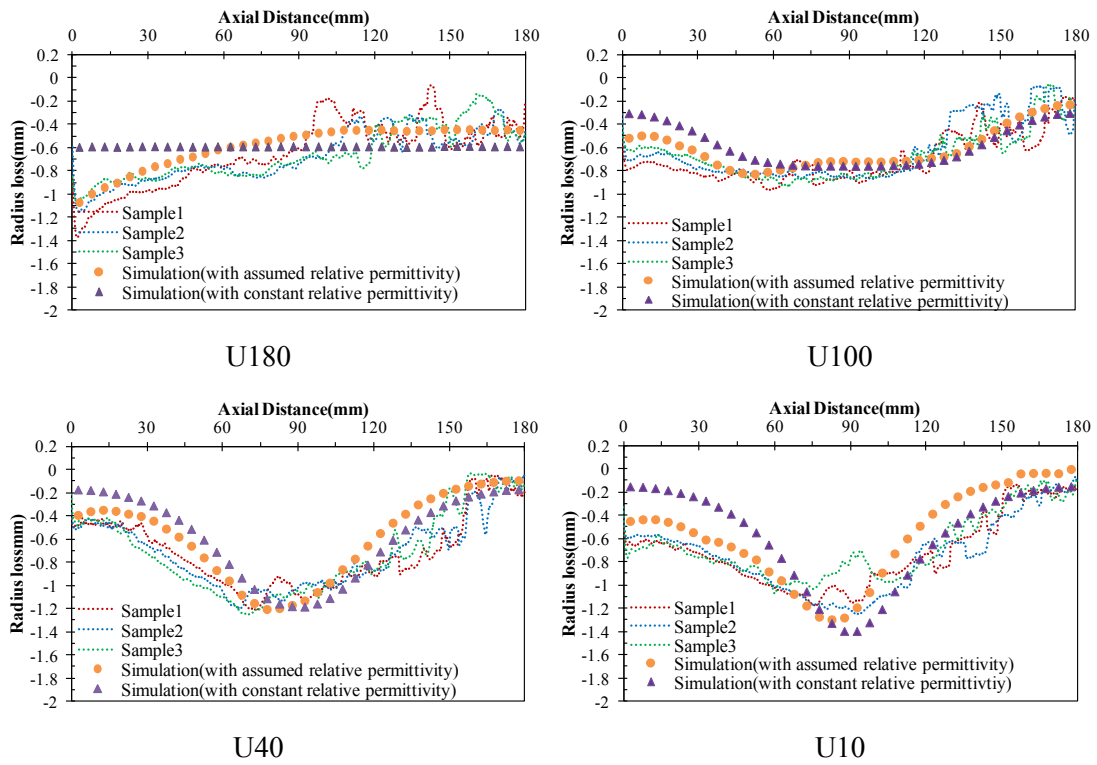


Figure 6.7 Influence of adhered corrosion products on the potential distribution

The simulated corrosion profiles for corrosion levels of 3% and 9% are compared to the experimental results in Figure 6.8(a). Since most of the tested specimens are uniformly corroded in the circumferential direction, the averaged radius loss based on the four measurement lines for each specimen is used in the comparison. The simulated results show good agreement with the test results, not only in the shape of the distribution but also in absolute values. When corrosion reaches 15%, corrosion profiles based on the assumed relative permittivity distribution are closer to the test results, as shown by the yellow dot lines in Figure 6.8(b).



(a) 3% and 9% corrosion

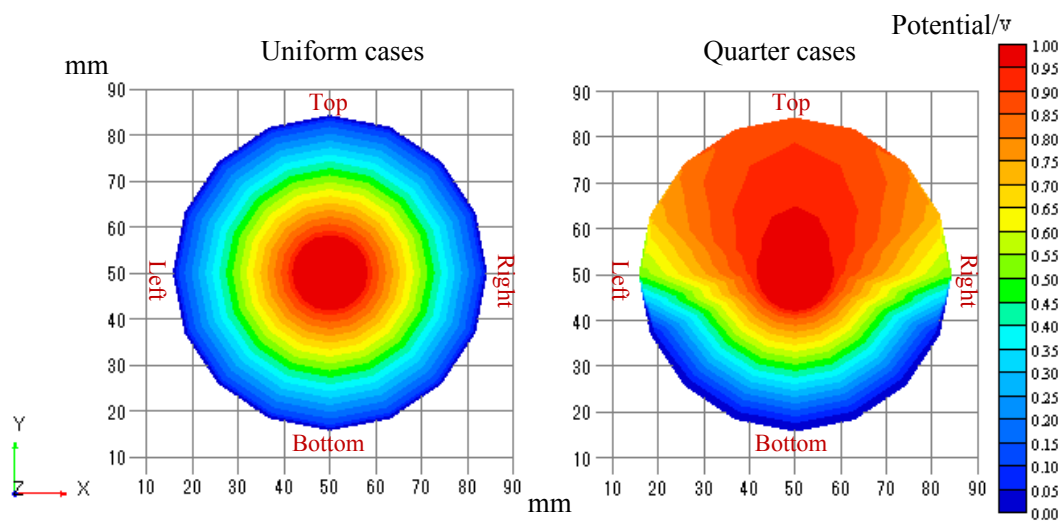


(b) 15% corrosion

Figure 6.8 Comparison of simulated corrosion profiles to test results (uniform cases)

6.5.1.2 Quarter cases

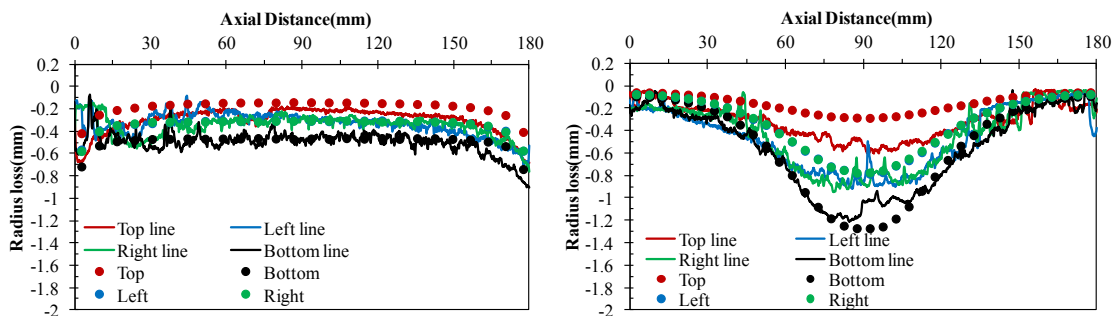
Figure 6.9 compares the modeled potential distributions at the center section of the experimental units between the uniform and quarter cases. It shows that the potential gradient for uniform cases is the same for all points in the circumferential direction, according with uniform corrosion, whereas for quarter cases the potential gradient at the bottom, i.e. the side nearest to the cathode is greater than that on the other sides, representing circumferentially non-uniform corrosion.



(a) Uniform cases

(b) Quarter cases

Figure 6.9 Comparison of potential distribution between uniform and quarter cases



(a) Q180-9%

(b) Q10-9%

Figure 6.10 Comparison of simulated corrosion profiles to test results (quarter cases)

The calculated corrosion profiles for the quarter cases are compared to the test results in Figure 6.10. These simulations are also consistent with the measured results, indicating that the truss network model used for analysis is effective for predicting the corrosion profiles of rebars exposed to a micro-cell corrosion circuit.

6.5.2 Evaluation of tensile performance

Following the successful prediction of radius losses, the load-deformation relationships of corroded specimens with various corrosion profiles were simulated, which are compared to the test results (obtained as explained by the digital image processing method) in Figure 6.11. The numerical predictions agree well with the test results, which confirm the applicability of the proposed numerical model to the evaluation of tensile performance of corroded rebars.

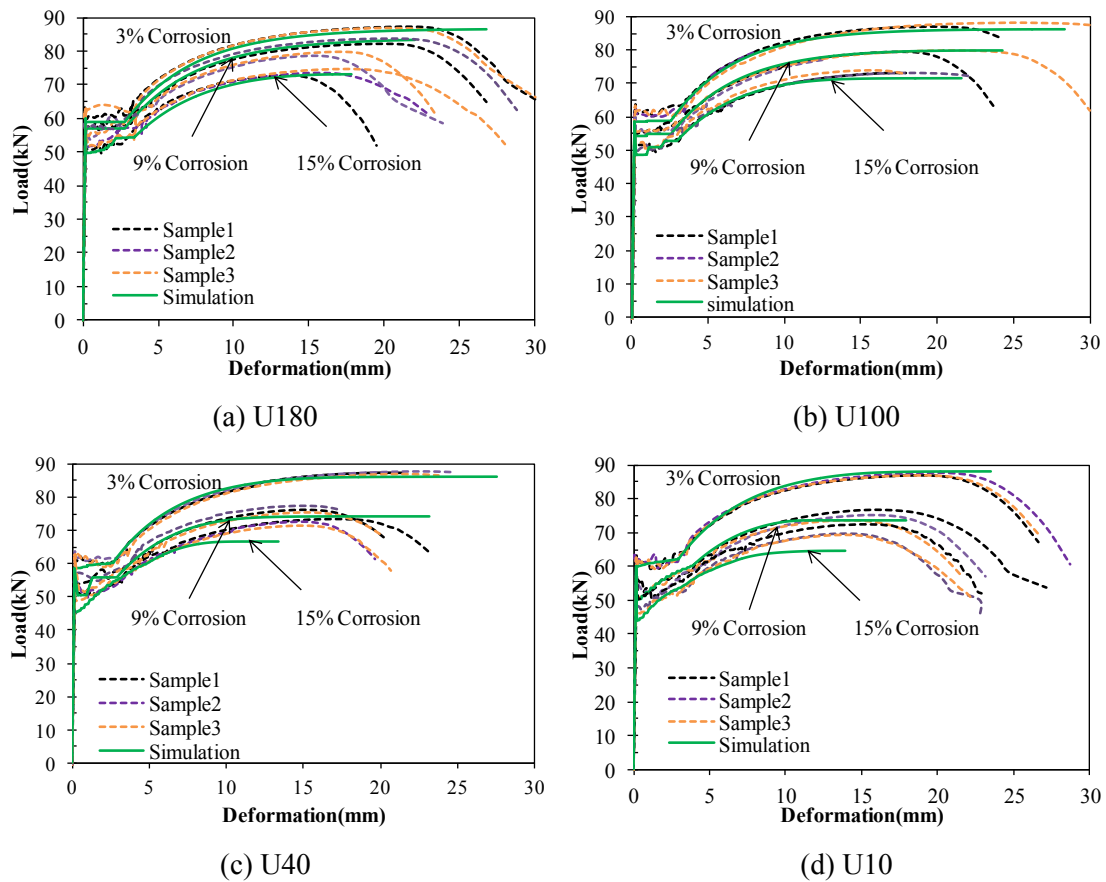


Figure 6.11 Comparison of simulated load-deformation relationships to test results

The estimated residual tensile strengths and elongations are compared to the test data in Figure 6.12. For clarity, the U180 and U10 series are shown as examples. It demonstrates that the proposed model, which considers the varying radius losses along the length of corroded rebars, can successfully deal with the effects of different corrosion states on rebar tensile strength. Since the rebar material model described in section 6.3 does not include the necking behavior that occurs before rebar fracture, the elongations computed by the numerical model are smaller than the test results. However, the degradation trend can be properly evaluated. The establishment of a complete tensile stress-strain relationship is a task for the future.

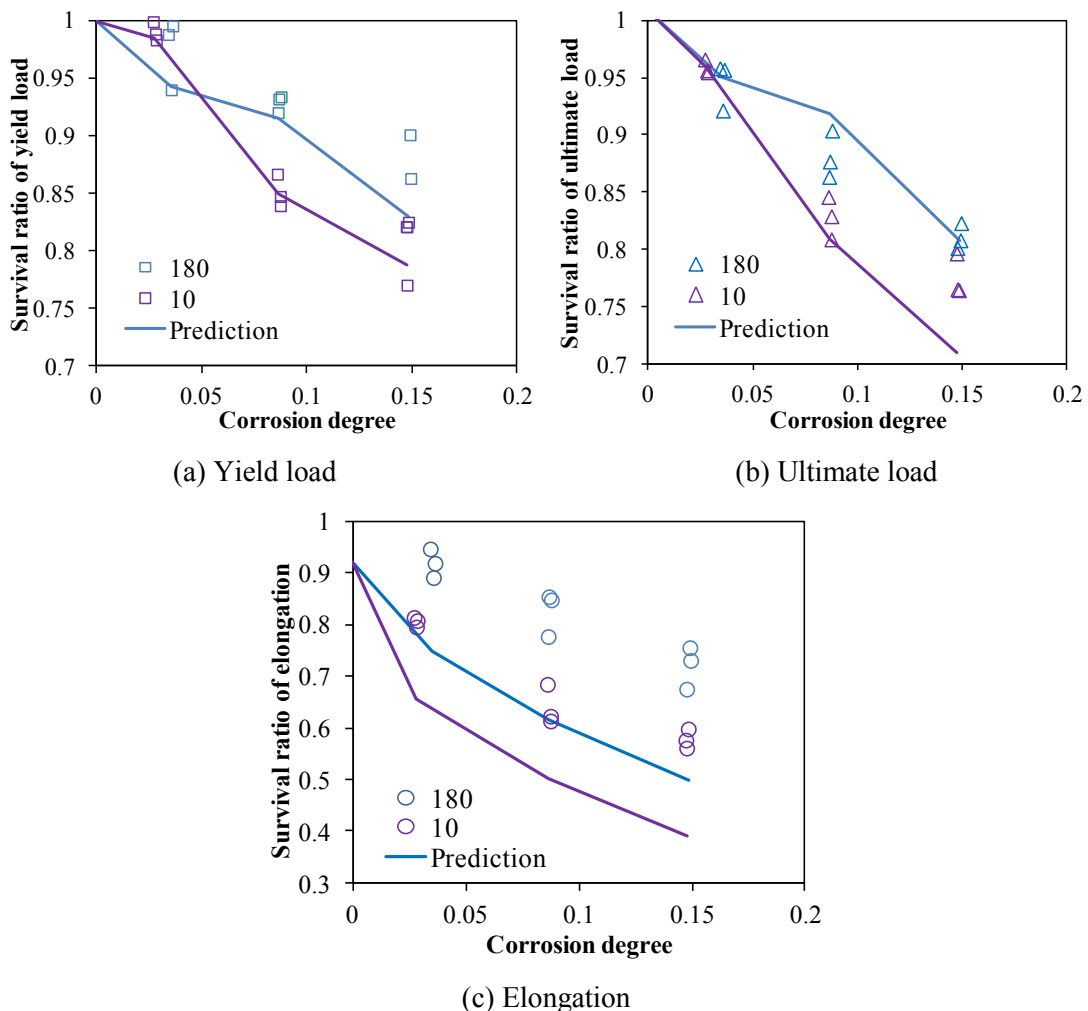
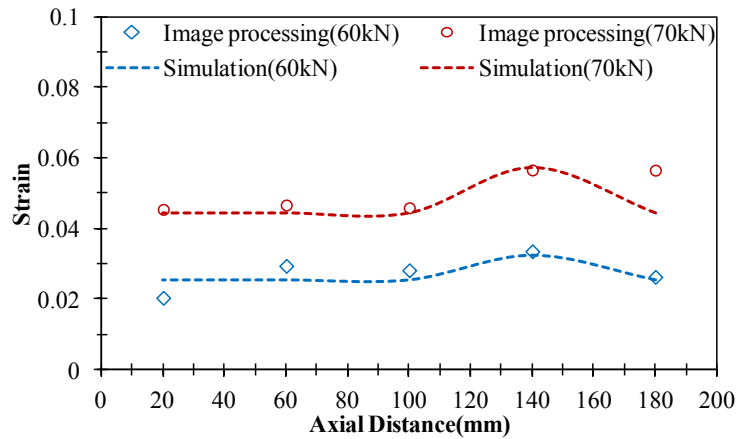
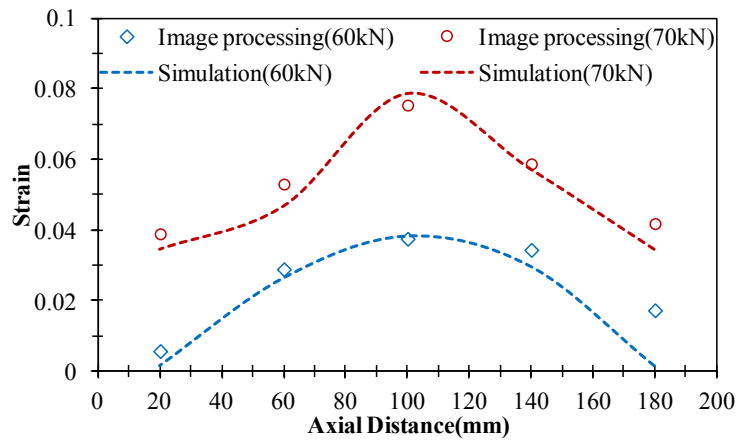


Figure 6.12 Estimates of residual tensile strength and elongation of corroded rebars

The proposed numerical model is also able to simulate local strains well. Taking U10-9% and U180-9% as examples, local strains corresponding to two different load states in the strain hardening stage are compared to the test data in Figure 6.13. The predicted strain distributions are similar to those obtained in the tensile tests, which indicates that the numerical model can be beneficial to the assessment of the deformation of corroded RC structures.



(a) U180 (9%)



(b) U10 (9%)

Figure 6.13 Comparison of simulated local strain profiles to test results

The generally excellent conformity with the results of tensile tests in terms of the load-deformation relationship, residual tensile strengths and local strain profiles confirms that the proposed numerical method can accurately predict the tensile behavior of corroded rebars. The use of a truss network in this study to calculate radius losses

along the rebar ensures that model integrity will be retained in the study of electric corrosion of rebar embedded in concrete, which is to be shown in Chapter 7. The proposed model can also make the use of corrosion profiles measured in laboratory tests or from field observations.

6.6 Summary and conclusions

A numerical model based on the RBSM and a truss network is developed in this chapter for evaluating the tensile behavior of corroded rebars and to accurately estimate residual tensile capacity. The feature of this model is taking into consideration corrosion topography. This model is verified with the test results of bare rebar specimens corroded with various corrosion profiles.

In the proposed model, the truss network model is applied to calculate the radius losses along the rebar using the Laplace equation and Faraday's law, which demonstrates a good prediction for the micro-cell corrosion circuit. The tensile behavior of corroded rebars can be well simulated by this model, in which degradation factors based on corrosion profiles are introduced into the rebar material model. Residual tensile strengths can also be accurately estimated with the proposed model.

7 Development of Electro-mechanical Model for Combined Analysis of Corrosion-caused Damage

7.1 Introduction

An accurate assessment of the damage level of RC structures that are exposed to rebar corrosion is crucial to efficient maintenance works, which requires a reliable model to evaluate the residual strength and crack development of the affected structures. In literature there is however no model available, which is able to evaluate both corrosion-induced concrete cracking and rebar tensile degradation. It is possibly due to the difficulty to simulate the corrosion process quantitatively. The experimental study on single-rebar specimens presented in Chapter 2 has demonstrated that a mutual effect may exist between corrosion and cracking, i.e. cracks enable quicker transport of chloride and water, thereby accelerating corrosion and causing more cracks. Moreover, in Chapter 6, it was found that corrosion profile i.e. radius losses along rebar surface is strongly related to the tensile behavior of corroded rebars. Hence, the coupling between corrosion and crack evolution needs to be considered in the model for a reasonable prediction of rebar radius loss, with which concrete cracking situations caused by expansion pressure of corrosion products can be analyzed (Tran et al. 2011) and residual tensile performance of corroded rebars can also be estimated (Qiao et al. 2015a).

On the other hand, electric corrosion method that is the application of direct current to the rebar embedded in concrete is often used to study corrosion related problems (Poursaee and Hansson 2009). Although this method has an advantage of obtaining a high corrosion level within a relatively short time comparing with other techniques, such as exposing the specimens to wetting-drying cycles, it is difficult to

control the electric corrosion process accurately due to the influence of cracks. Both surface crack width and mass loss predicted by Faraday's law might be inappropriate as parameters to indicate corrosion damage (Malumbela et al. 2012). Therefore, a numerical model that can analyze electric corrosion process and the caused damage is wanted.

In this chapter, a time-dependent electro-mechanical model based on the RBSM combined with a truss network is proposed to evaluate the electric corrosion process of rebar embedded in concrete and associated concrete crack development. In the analysis, concentrated corrosion near cracks is considered by assuming the relation between crack width and local current efficiency owing to the merit of the RBSM that crack width can be directly calculated in the simulation. With the proposed model, tensile behavior of corroded rebars with various corrosion levels is also analyzed. The applicability of this model is verified by comparisons to the test results of the basic study using single-rebar specimens as presented in Chapter 2. In addition, an attempt is made with the proposed model to analyze crack propagation caused by local corrosion along the rebar length.

7.2 Analytical process flow

The series of electric corrosion tests of single-rebar specimens studied in Chapter 2 are analyzed. Table 7.1 lists the test conditions. In the analysis, a three-phase material model including concrete, corrosion products and rebar is set up based on the RBSM (see Figure 7.1). This model has a dimension of 200mm × 500mm × 200mm (length × width × height), the same as that of the specimens tested in the basic experimental study (see Figure 2.4), although without the extended rebar part. The mesh sizes of the Voronoi particles in the cover area near rebar are 5mm, while the mesh size in the outer area is 20mm.

Table 7.1 Test conditions of single-rebar specimens carried out

Study series	Current flow (A*hr)	Corrosion degree (%)
T86, T205, T341, T500, T625	6.89, 16.36, 27.27, 40.0, 50.0	0.66, 1.82, 3.19, 5.17, 6.26

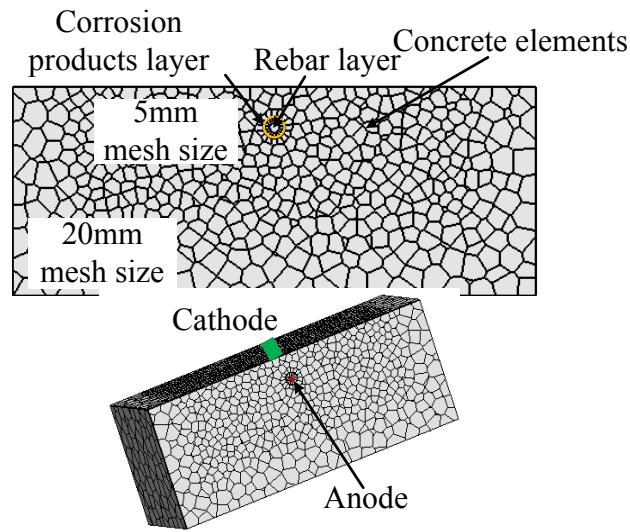


Figure 7.1 Three-phase material model

The electro-mechanical model developed consists of corrosion current analysis by truss network model, corrosion expansion analysis and tensile simulation by the RBSM (see Figure 7.2). In the corrosion current analysis, the potential distribution under an external applied electric field is calculated based on the Laplace equation (Moliton, 2007). The parameters of relative permittivity for rebar and corrosion products are set according to Table 6.1, while the value for concrete is set as 6 (Conyers 2013). For the boundary conditions, the potential of the anode is simply assumed to be 10V, while the boundaries representing the cathode are fixed as zero (see Figure 7.1). The potential difference between the anode and cathode has the same order of magnitude as that observed in the corrosion test. A zero influx condition is applied on the other boundaries. Assuming only micro-cell corrosion circuit is involved in the electric corrosion process, the corrosion current I_i flowing through each truss element connecting the rebar layer and corrosion products layer can be easily determined with Ohm's law. In the analysis the targeted current flows are consistent with those applied in the test (see Table 7.1). The increment of mass loss Δm_i for each corroded rebar element i is calculated using Faraday's law, into which the current efficiency N_i related to the crack width w nearby is introduced.

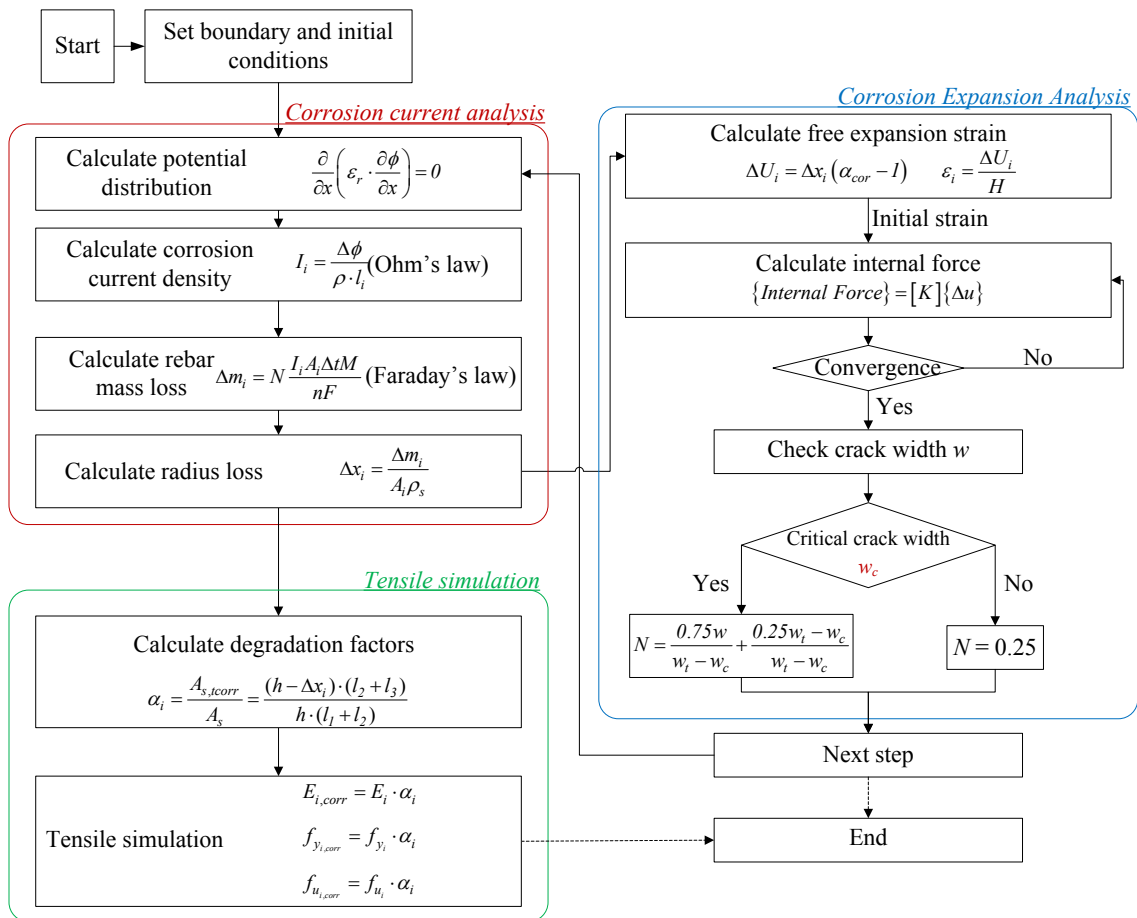


Figure 7.2 Coupled electro-mechanical model

Under an electric field with a potential drop greater than 10V, transport of chloride ions is mainly due to ions migration and the transport speed is related to diffusion coefficient of concrete (Andrade 1993a). Djerbi et al. (2008) carried out a steady-state migration test to study the effect of crack on chloride diffusion into concrete. Their results indicated that the diffusion coefficient of chloride ions through the crack might increase as the crack width increased and almost became constant when the crack width was greater than 80 μ m. Considering that the current efficiency rises with an increase of chloride concentration in concrete (Nossoni and Harichandran, 2012), it can be assumed that the current efficiency for a rebar element may increase if a crack with sufficient crack width occurs at the neighboring concrete element. Thus, their relations are assumed in Figure 7.3. The current efficiency N is initially kept as 0.25. This value is in agreement with those found in other reported studies with a low content of chloride in concrete, 0.23 by Kawamura et al. (2009) and 0.30 by Nossoni and

Harichandran (2012). When a small crack with a width w_c appears, the local current efficiency increases linearly to 1 corresponding to a large crack width w_t . The values of w_c and w_t are estimated by comparing the simulations to the test results, which is shown in the following analytical results.

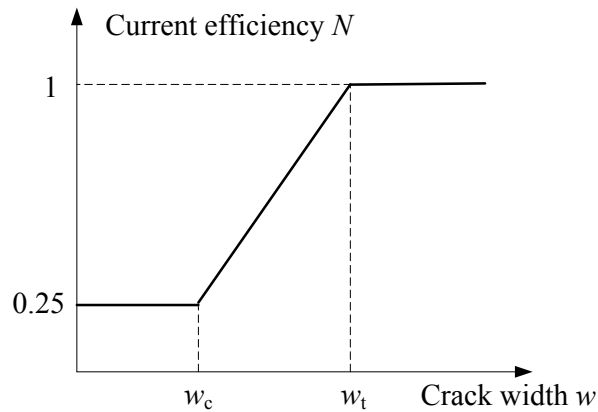


Figure 7.3 Relation of current efficiency to crack width

In the corrosion expansion analysis (see Figure 7.2), the internal expansion pressure is exerted on the elastic corrosion products layer, which has a constant thickness H . The thickness is set as 1mm and the elastic modulus of corrosion products layer is assumed as 500MPa (Tran et al. 2011). The expansion pressure is simulated based on the initial strain problem with increment of free increase of rebar radius ΔU_i in each analysis step. ΔU_i is calculated based on the increment of radius loss Δx_i and the volume-expansion ratio α_{cor} of corrosion products that is assumed as 2.5. Thereby, the expansion pressure distributed non-uniformly over the rebar surface can be automatically obtained from the corrosion current analysis. In consideration of the nature of corrosion expansion, the initial strain is only applied to the normal springs located on the boundary between the corrosion products layer and the rebar layer. The cracking conditions obtained in the present step are used to determine the new series of current efficiencies N and to calculate the increment of initial strains around the rebar for the next step. The feature of this model is that the corrosion and cracking process is controlled only by the time increment Δt , which can contribute to the evaluation of time dependent behavior of concrete structures.

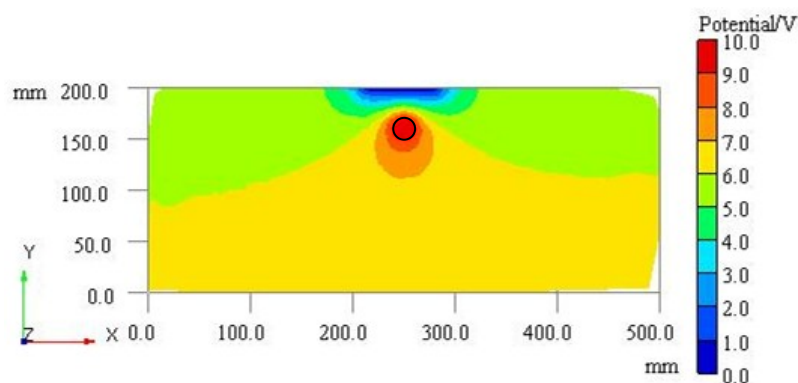
In the tensile simulation (see Figure 7.2), the radius losses along the rebar for a targeted corrosion extent are obtained from the corrosion current analysis, with which degradation factors are calculated and introduced into the rebar material model. Then the residual tensile capacity of the rebar corroded in concrete is evaluated.

The developed electro-mechanical model has several advantages. The simulation by this model is the function of time. It can predict time-dependent corrosion process. The corrosion distribution along and around rebar can be automatically obtained. The expansion pressure of corrosion products is automatically determined as well. Therefore the concrete crack pattern and rebar tensile behavior can be properly evaluated.

7.3 Analytical results

7.3.1 Electric corrosion process

To clarify the effect of cracks on the electric corrosion process, a case without considering the variation of current efficiency with crack width is carried out firstly. In this way, the corrosion current analysis and corrosion expansion analysis are independent with each other. The radius losses around the rebar are only determined by the potential distribution resulting from the applied electric field, which is shown in Figure 7.4.



Noted: rebar is indicated with a black circle

Figure 7.4 Potential distribution at the center section of the specimen

The red area with a potential of 10V represents the rebar, while the blue area at the top surface shows the region with salt-water pool. As can be seen, the potential drop for the upper circumference of rebar is approximately two times that for the lower circumference, which can be attributed to the varied distances to the salt-water pool. Accordingly, the upper part is more corroded.

Figure 7.5 shows the simulated residual sections of rebars subjected to varied current flows, where the current efficiency is kept as a constant of 0.25. Although in the simulation corrosion appears to concentrate at the upper circumference, the predicted radius losses for this part are clearly smaller than those in tests, especially in the cases with large cracks (see T500 and T625). Comparing the ratio of the average radius loss at the top quarter side RL_U to that at the bottom side RL_D (see Figure 7.6), it yields a constant value of 2.47 in the analysis, whereas the ratio measured in the test gradually rises when corrosion degree is over 2%. It proves that cracks have a strong effect on the corrosion pattern around the rebar.

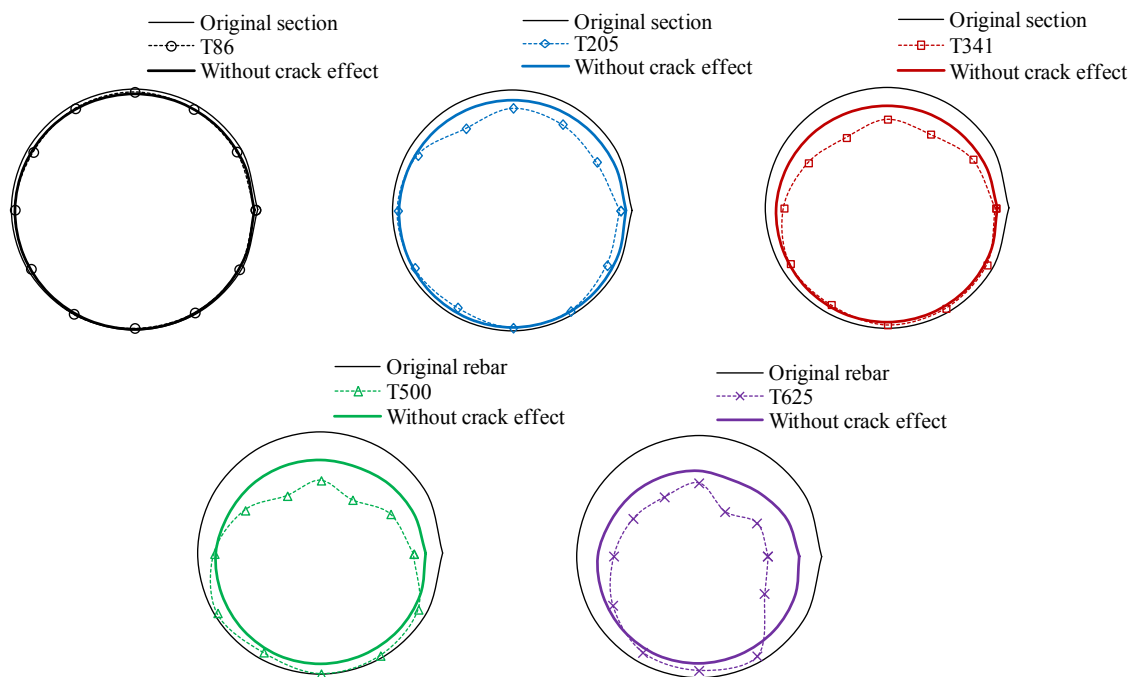


Figure 7.5 Simulated rebar section without crack effect

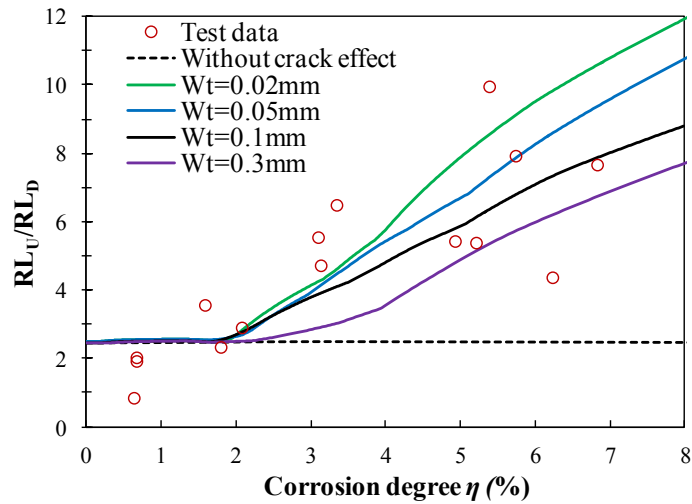


Figure 7.6 Modeled ratio of radius losses between top and bottom sides

In the second case, the assumed relationship between local current efficiency and crack width is applied in the electro-mechanical model. In order to verify the model, several values for w_c and w_t were examined (see Figure 7.7). The w_c is related to the initiation of the influence of crack. It was firstly checked, in which w_t was assumed to be equal to w_c . Considering that when corrosion degree exceeds 2%, crack may already affect the corrosion pattern (see Figure 7.6), it seems that a crack width of 0.01mm is suitable for starting accounting for the crack effect. Then w_t ranged from 0.02mm to 0.3mm was analyzed. As can be seen, if w_t is set as 0.1mm, the corrosion process simulated shows a good agreement with the test data. Corrosion rate starts to increase when current flow reaches 20.5A*hr. In the analysis a visible surface crack with a width of 0.05mm also appears. The radius losses in the circumferential and longitudinal directions modeled with this assumption are shown in Figure 7.8 and Figure 7.9 respectively. The predicted residual cross sections are similar to those measured in the test. The calculated values of radius losses are within a reasonable range for various corrosion degrees. Moreover, the simulation also demonstrates that generated cracks can enlarge the difference of corrosion rates between the top and bottom sides (see Figure 7.6).

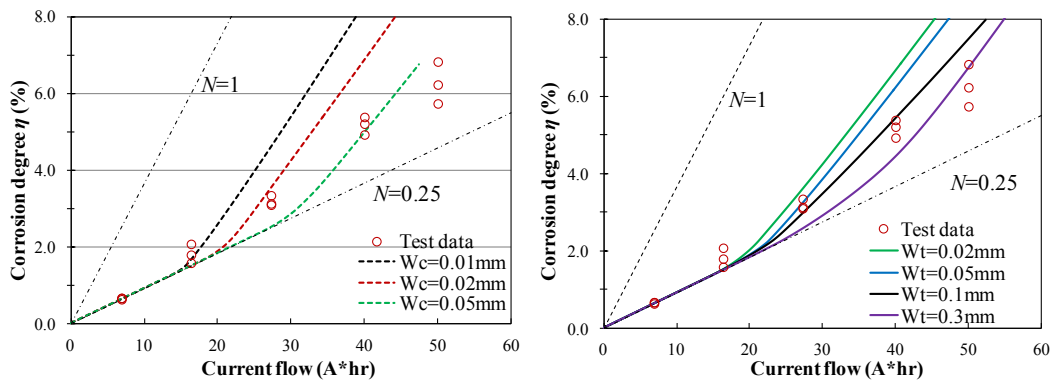


Figure 7.7 Verification of relationship between crack width and current efficiency

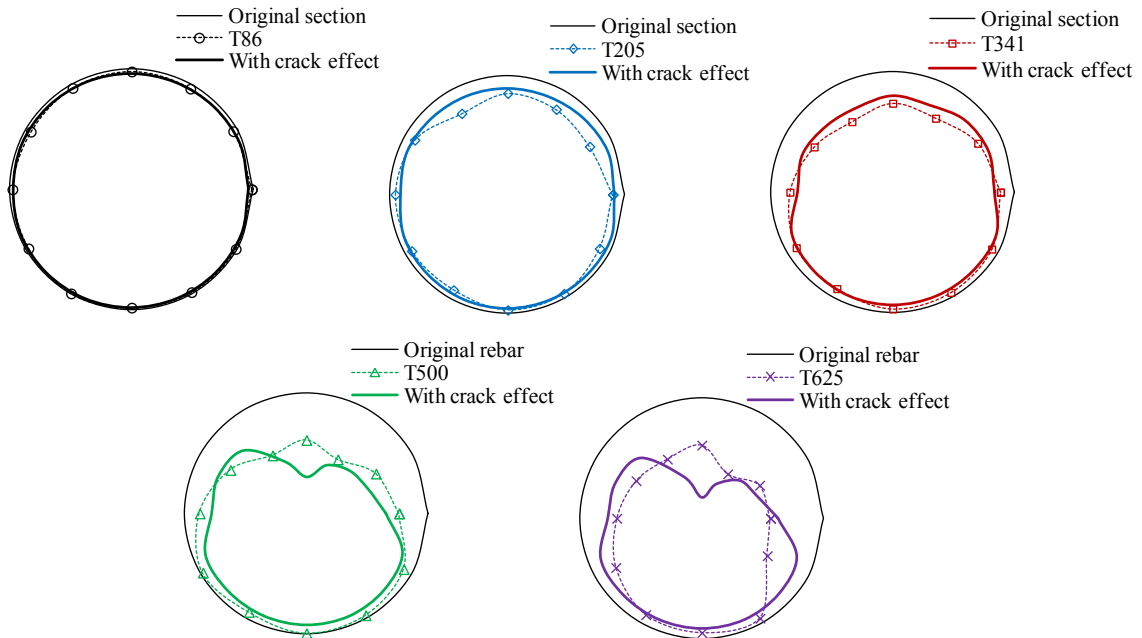


Figure 7.8 Simulated rebar section with crack effect

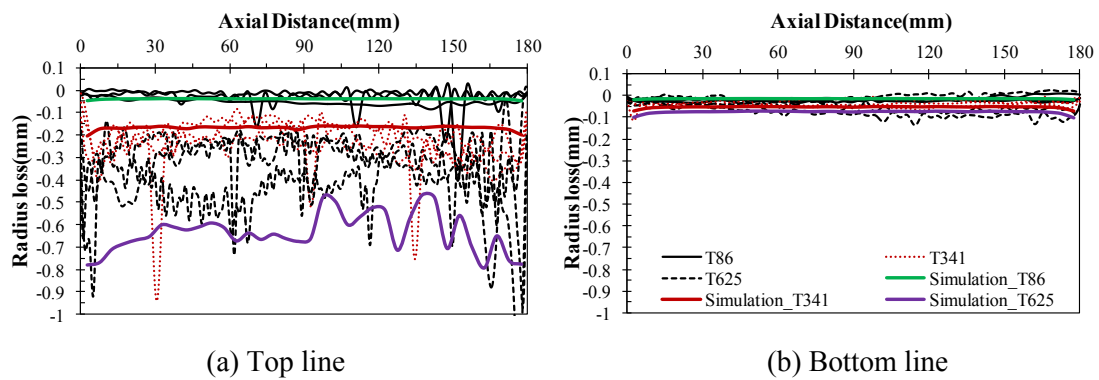


Figure 7.9 Modeled radius losses along rebar

The analysis shows a valid prediction on the electric corrosion process when rebar is corroded continuously along the length direction. It suggests that cracks with a width of 0.1mm and more generated in the concrete cover may greatly increase the corrosion rate of the adjacent rebar part.

7.3.2 Internal crack pattern

Figure 7.10 shows the simulated internal crack patterns, in which the analytical results with and without crack effect are compared with test results. With the same amount of current flow, the simulation case considering the influence of crack on corrosion process shows a more severe cracking situation. It is because that the increase of corrosion rate at the rebar upper part due to crack may result in a larger expansion pressure, thereby causing more cracks. Compared with test results, it seems that under a relatively lower corrosion degree than 3.19% (T341), the crack conditions modeled with crack effect agree well with the test results, not only in the pattern but also in the crack width and length. However, with a further increase of corrosion amounts, the cracks predicted develop faster than those observed in the test, although the crack patterns are still similar. Even in the case without crack effect where the expansion pressure is relatively small, the calculate crack lengths are greater than those of test results. During the test, for the series of T500 and T625, a few corrosion products exuded from the sides of the concrete specimens where the rebars extended, which might reduce the expansion pressure and delay the propagation of cracks. This difference suggests that at T341 crack width is sufficiently large and current efficiency reaches a maximum value. Thereby the corrosion develops with a nearly constant speed (see Figure 7.7).

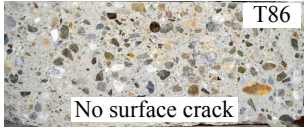
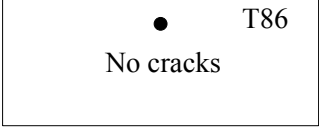
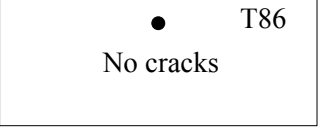
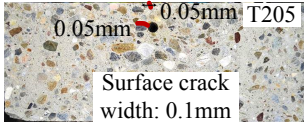
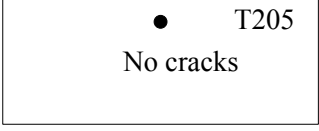
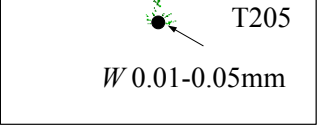
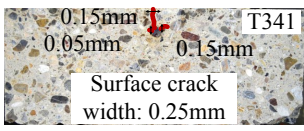
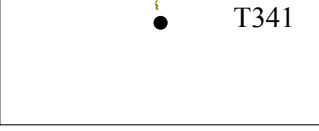
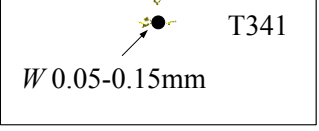
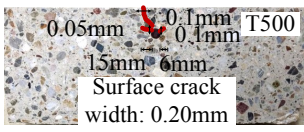
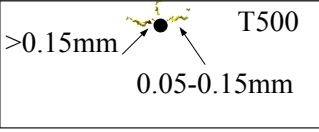
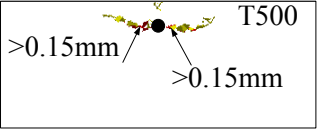
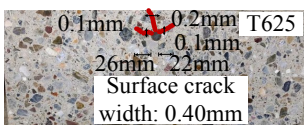
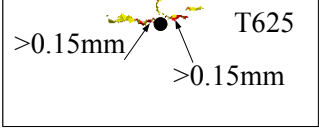
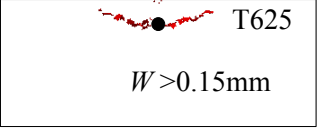
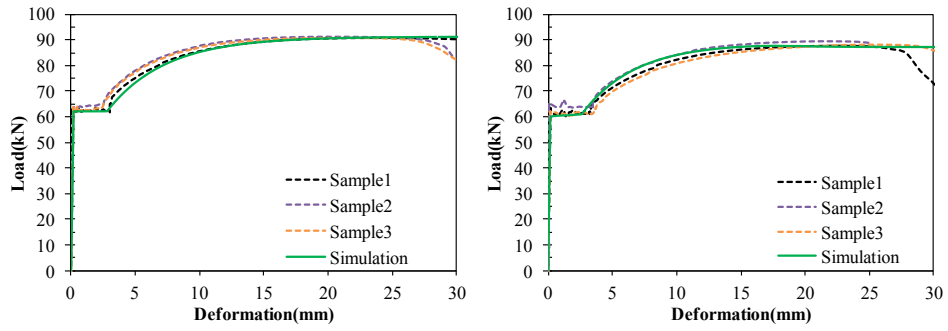
Test results	Without crack effect	With crack effect
 <p>T86 No surface crack</p>	 <p>T86 No cracks</p>	 <p>T86 No cracks</p>
 <p>T205 Surface crack width: 0.1mm</p>	 <p>T205 No cracks</p>	 <p>T205 W 0.01-0.05mm</p>
 <p>T341 Surface crack width: 0.25mm</p>	 <p>T341</p>	 <p>T341 W 0.05-0.15mm</p>
 <p>T500 Surface crack width: 0.20mm</p>	 <p>T500 >0.15mm 0.05-0.15mm</p>	 <p>T500 >0.15mm >0.15mm</p>
 <p>T625 Surface crack width: 0.40mm</p>	 <p>T625 >0.15mm >0.15mm</p>	 <p>T625 W >0.15mm</p>

Figure 7.10 Simulated internal crack patterns

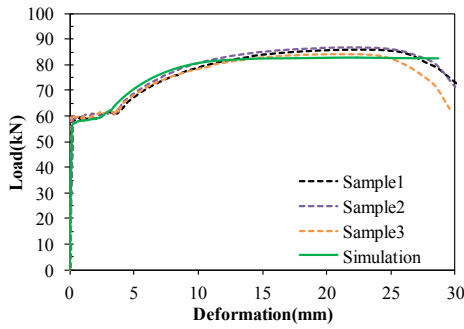
7.3.3 Tensile behavior of corroded rebars

The proposed electro-mechanical model presents a reasonable prediction of radius losses, which are used to evaluate tensile behavior of corroded rebars with different corrosion degrees. The simulation results for three series including T86, T341 and T625 are compared to the test results to show the applicability of the proposed model. The load-deformation relationships of corroded rebars are presented in Figure 7.11, in which a good agreement can be found. Both simulation and test results show that with an increase of corrosion degree (approximately 3%), yield load slightly decreases and ultimate load reduces by 2.8kN. The local strains under two different loads in the strain hardening stage are compared to the test data obtained by image processing method, which is shown in Figure 7.12. As can be seen, the predicted strain distributions for various corrosion levels are also in accordance with the test data. These results confirm that the proposed model can accurately evaluate the tensile performance of rebars affected by corrosion.



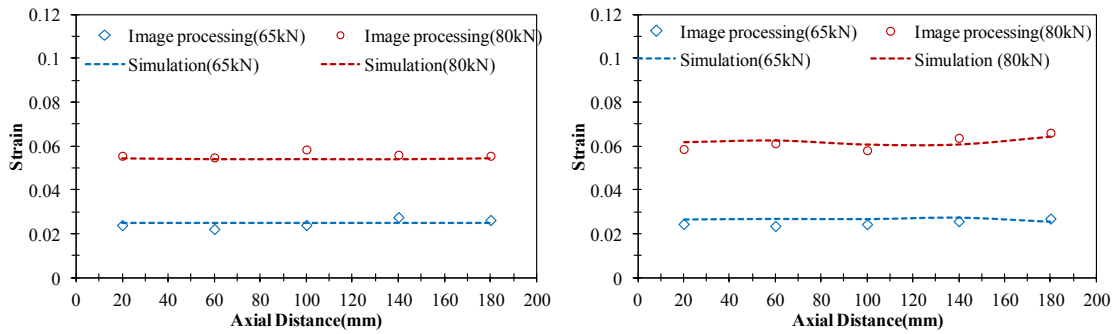
(a) T86

(b) T341



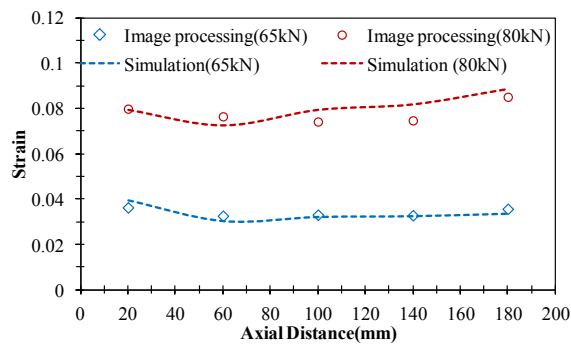
(c) T625

Figure 7.11 Simulated load-deformation relationships of corroded rebars



(a) T86

(b) T341



(c) T625

Figure 7.12 Simulated local strain profiles

7.4 Application in local corrosion case

The electro-mechanical model verified previously can successfully deal with crack propagation caused by uniform corrosion along the rebar length. This model is applied in the local corrosion case studied in Chapter 4. The specimens with 30mm cover are targeted. In the analysis, a RBSM model having the same dimension as that of test specimens is created. For corrosion current analysis, a region at the top surface of the model is set as the cathode corresponding to the area with salt-water pool in the test, which is given with a fixed potential of 0V, while a rebar node is treated as the anode with a potential of 10V (see Figure 7.13).

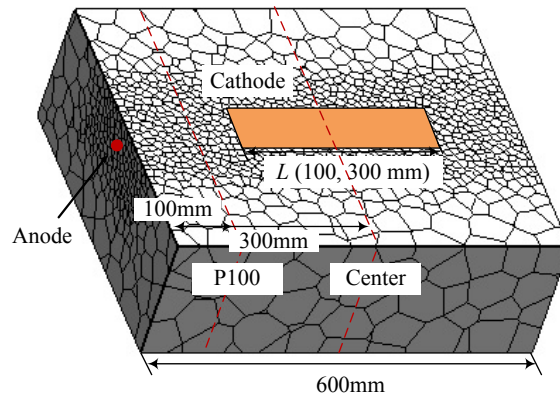
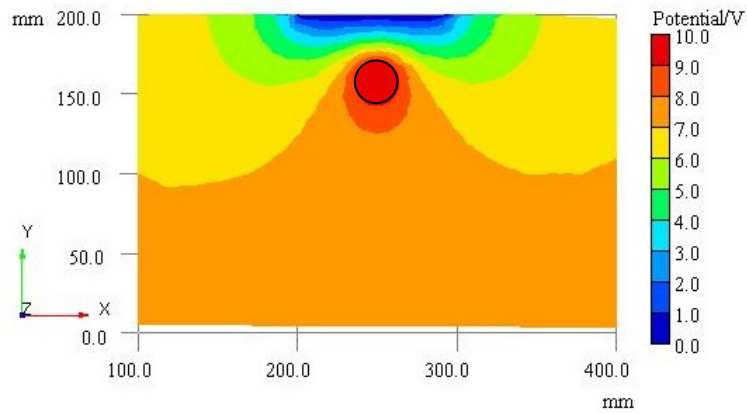
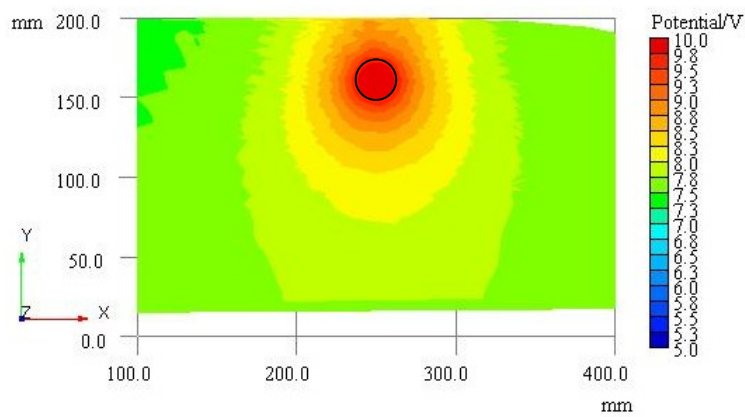


Figure 7.13 Electric boundary conditions for local corrosion case

The potential distributions at two different sections, the center section under the salt-water pool and the P100 section distant from the pool (see Figure 7.13), are calculated for the study cases with 300 and 100mm long salt-water pool respectively, which are shown in Figure 7.14 and Figure 7.15. In both cases, it is shown that at the center section the potential drop at the rebar upper part that almost reaches 2V is greater than that at the lower part, while at the P100 section the potential drop is nearly the same around the rebar, which is less than 0.7V. Consequently, as the applied current flow increases, corrosion may concentrate within the region under the salt-water pool. In the case of L100C30, the potential drop at the P100 section is merely 0.2V, which is smaller than that of L300C30. Hence it can be expected that for L100C30 corrosion would be further localized.



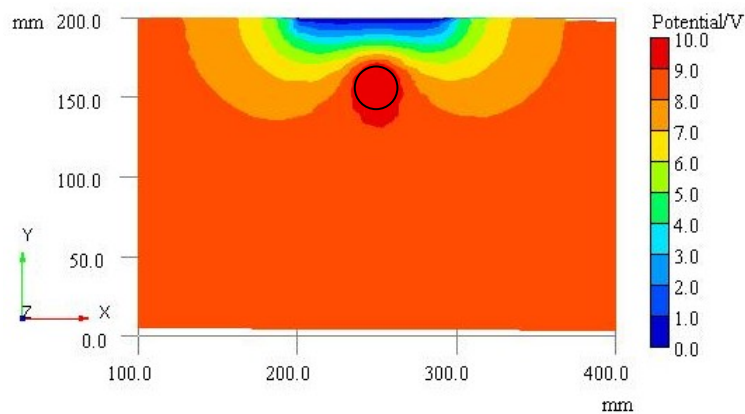
(a) Center



(b) P100

Noted: rebar is indicated with a black circle

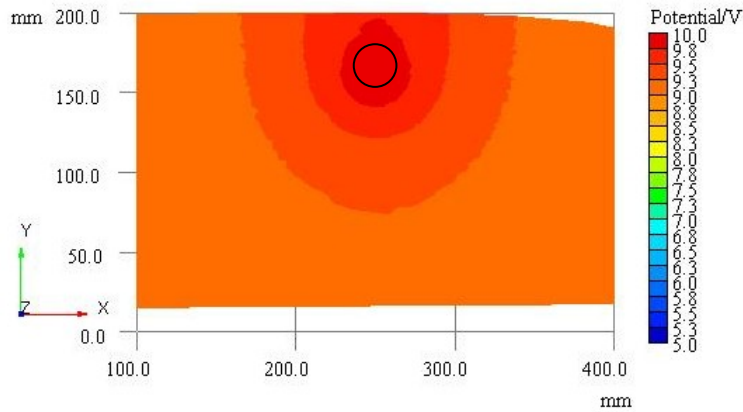
Figure 7.14 Potential distributions at different sections for L300C30



(a) Center

Noted: rebar is indicated with a black circle

Figure 7.15 Potential distributions at different sections for L100C30



(b) P100

Noted: rebar is indicated with a black circle

Figure 7.15 Cont.

Figure 7.16 shows simulated distributions of corrosion degree along the rebar, in which the position of salt-water pool is indicated by dash line. For each case, the analysis without considering crack effect is also carried out for comparison. In the case with 300mm long salt-water pool, the corrosion distribution modeled with crack effect is similar to that measured in the test at a close current flow (103.93A*hr). The analysis also indicates that cracks generated in the area under the salt-water pool greatly promote the corrosion process at the center part of the specimen. However, for 100mm long salt-water pool, the model only yields a good prediction within a short corrosion time. When current flow increases to 55A*hr, the simulation shows a significant high corrosion degree at the rebar part under the salt-water pool, while the corrosion extent of the rebar ends distant from the pool barely increases, which is caused by a relatively lower potential drop as shown in Figure 7.15b. The difference between the analysis and experimental results suggest that when a short cathode (100mm) is used in the test, the corrosion process of the rebar ends may be affected by other factors, possibly the action with oxygen.

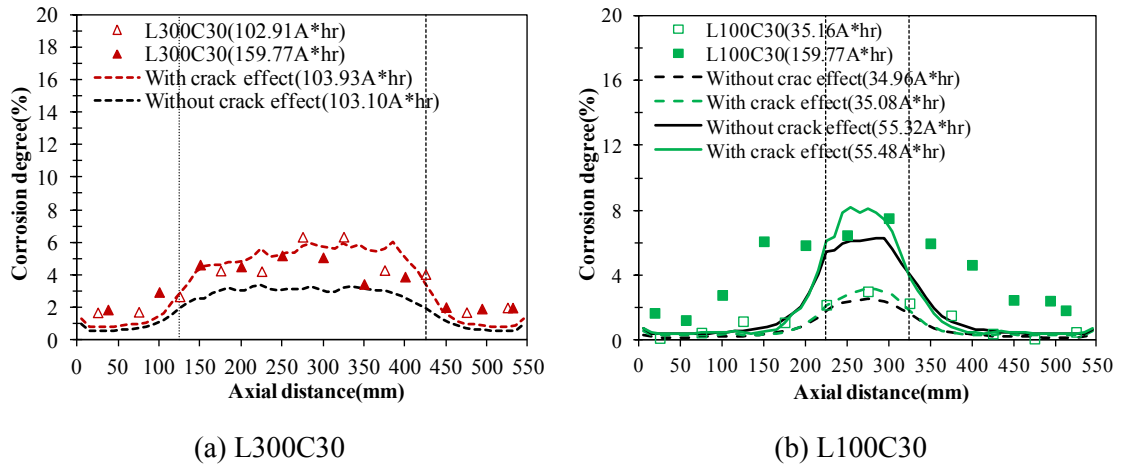


Figure 7.16 Simulated corrosion distributions along rebar

The modeled surface crack patterns for L300C30 and L100C30 are shown in Figure 7.17 and the corresponding internal crack patterns at different sections along the rebar length are presented in Figure 7.18. The yellow and red cracks represent the ones with widths of 0.1mm and 0.3mm separately. As can be seen, in the case with 300mm long salt-water pool, the simulated surface crack pattern is similar to the test result. A longitudinal crack along with some short cracks appears on the concrete surface. Inside concrete, the crack pattern varies between the area under salt-water pool and the external areas. The inclined lateral cracks can be confirmed at the center part of the specimen. On the other hand, for 100mm long pool, a spalling occurs on the concrete surface, which is different from the surface crack condition demonstrated in the test. It is due to a faster increase of corrosion level at the rebar part under the pool compared with that in the test (see Figure 7.16b). However, this result still indicates that when concentrated corrosion occurs, lateral cracks may incline to the concrete surface rather than develop horizontally as shown by 2D cracking behavior (see section ③ in the case of L100C30).

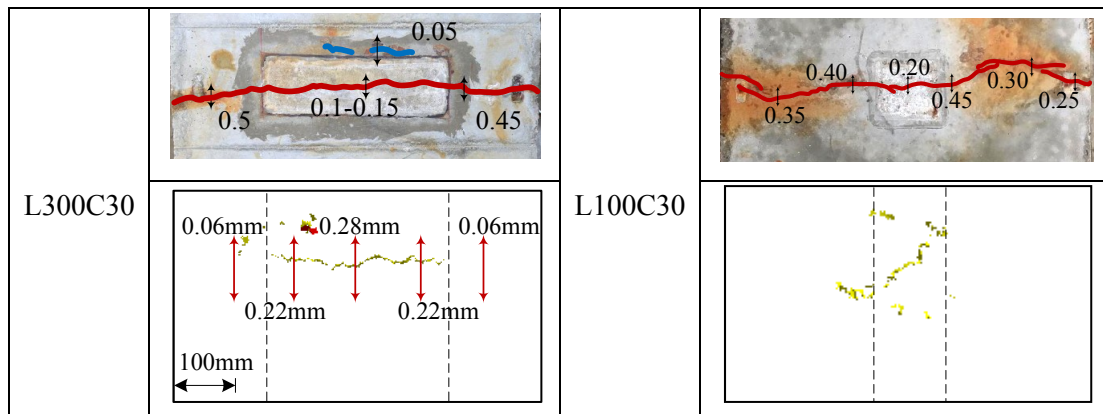


Figure 7.17 Simulated surface crack patterns by electro-mechanical model

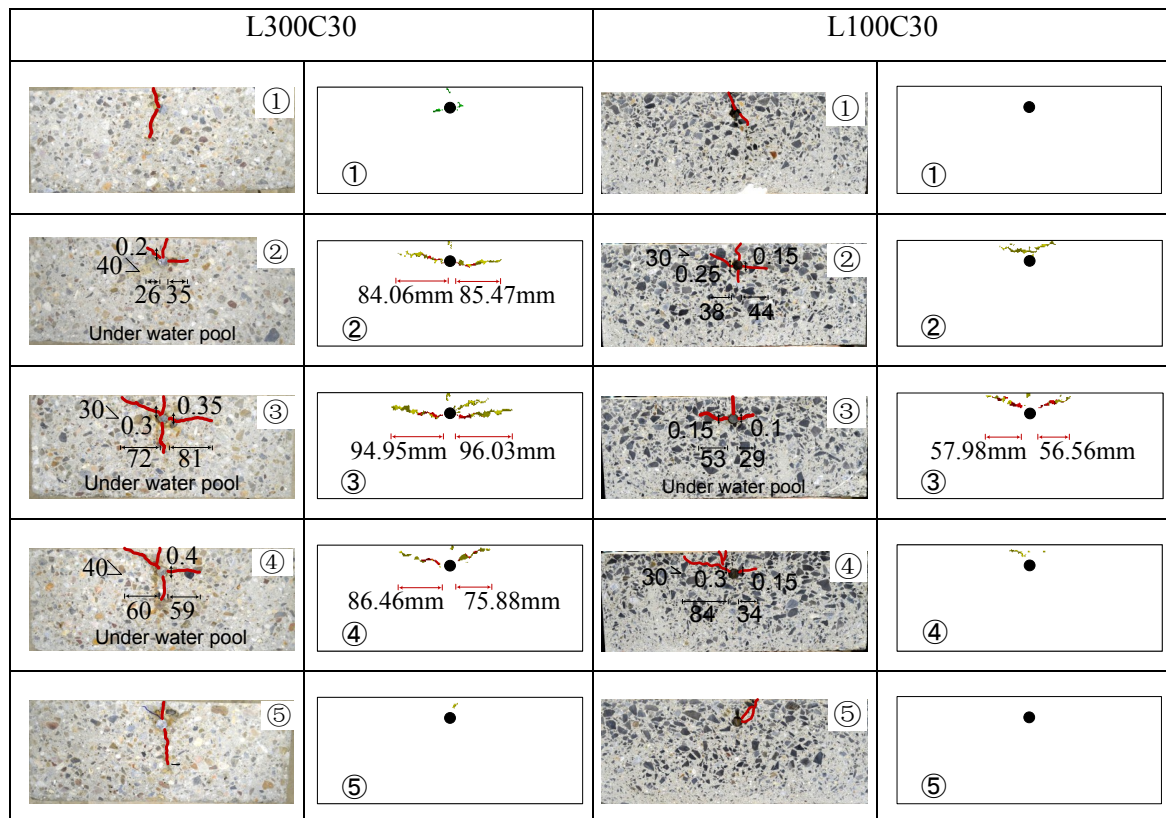


Figure 7.18 Simulated internal crack patterns by electro-mechanical model

The analytical results discussed herein show that the proposed electro-mechanical model is limited to the case in which electric corrosion process of rebar is primarily controlled by the applied electric field. The corrosion process implemented by

a salt-water pool with a length of 100mm is more complex and thereby the resulting corrosion distribution is not as concentrated as the ideal one as predicted by the electro-mechanical model. For such a case, the transport of oxygen through concrete cover and the consumption of oxygen need to be considered in the model.

7.5 Summary and conclusions

In this chapter, the evaluation method for the residual tensile performance of corroded rebars that is proposed in Chapter 6 is integrated into the corrosion-expansion model (Tran et al. 2011) for the combined analysis of concrete crack propagation and rebar tensile degradation. The time-dependent electro-mechanical model developed is based on an accurate prediction of the electric corrosion process of rebar, in which the interaction between cracks and corrosion is considered with an assumption that local current efficiency varies with the width of the crack nearby. The model is verified with the test results of the basic experimental study as presented in Chapter 2. The simulations agree well with the test results in terms of radius losses along the rebar surface, internal crack patterns and tensile behavior of rebars with various corrosion degrees. It confirms the applicability of the proposed model to assess the corrosion-caused damage for a targeted corrosion level, if corrosion distributes consistently along the rebar length. The analysis also shows that, under electric corrosion, when a crack with a width greater than 0.1mm is generated, the rebar part nearby may be highly corroded.

On the other hand, the proposed model was also employed on the local corrosion case studied in Chapter 4. The predictions of corrosion distribution and cracking condition for the case with 300mm long salt-water pool are acceptable, while in the case with 100mm long pool the simulation overestimates the extent of concentrated corrosion. It is because that in the current model only the micro-cell corrosion circuit resulting from the applied electric field is taken into account. The model needs to be improved by considering consumption of oxygen in the future work to better assist in the application of the electric corrosion method that uses a salt-water pool on the concrete cover to study the structural behavior of corroded RC members.

8 Summary and Conclusions

8.1 Conclusions

The objective of this study is to evaluate the corrosion-caused damages characterized by concrete cracking and rebar tensile degradation in three-dimensional level, which are studied both experimentally and analytically. In order to simulate the natural chloride-induced corrosion pattern in the experiment, an electric corrosion method using a salt-water pool on the concrete cover is proposed, with which the cracking behavior of single-rebar specimens resulting from non-uniform corrosion around the rebar as well as local corrosion along the rebar length is investigated. Besides, a fast and simple method of simulating various corrosion profiles of rebars by using different cathode arrangements is introduced. The prepared rebar specimens are used in the tensile tests to clarify the effect of corrosion distribution on the tensile behavior of corroded rebars. In the analytical study, the corrosion-expansion model based on the RBSM is applied to simulate crack patterns by assuming corrosion distribution on the basis of the measured results. For evaluating the residual tensile performance of corroded rebars, a numerical model using a truss network incorporated with the RBSM is proposed, which takes into consideration corrosion profile. This model is also combined with the corrosion-expansion model for a comprehensive analysis of corrosion-induced damages on reinforced concrete. The conclusions derived from this study are made as follows.

- (1) The corrosion process implemented by the proposed electric corrosion method is investigated in terms of corrosion degree by weight loss and corrosion profile by radius losses, which confirms that this method can simulate the natural corrosion pattern caused by chloride ions that is corrosion concentrates at the

circumference facing the concrete cover. It is also found that the cracks generated in the concrete cover may increase the corrosion rate of the rebar part nearby.

- (2) The electric corrosion test using bare rebar specimens demonstrates that with a small cathode the resulting corrosion can concentrate at the rebar part close to the cathode to a certain extent. Similarly, in the corrosion test of single-rebar slab specimen, the use of a short salt-water pool can cause a relatively high corrosion level under the pool, which is confirmed by the measurements of corrosion distribution along the rebar. Hence, local corrosion along the rebar length can be simulated by the proposed test method.
- (3) The test results for concrete cracking behavior show that when corrosion distributes nearly uniformly along the length of the rebar, the internal crack patterns for the cases with 30mm and 10mm concrete cover both consist of parallel cracks to the concrete surface. In the case of local corrosion that is corrosion concentrates at the center part of the rebar, the internal crack pattern varies along the rebar length. At the center part the inclined lateral crack appears instead of the parallel crack as shown by 2D cracking behavior, which can lead to cover spalling, while at the area with less rebar corrosion only vertical cracks are obvious. The test results suggest that the applicability of the theoretical crack patterns is limited since they do not account for the effect of various corrosion states.
- (4) The corrosion-expansion model can simulate reasonable crack patterns compared to the test results, if the corrosion distribution is properly assumed. The analysis indicates that for 2D cracking behavior internal crack propagation is dependent on the corrosion pattern around the rebar rather than the cover thickness. If corrosion distributes broadly, parallel cracks also appear for 10mm cover. The analysis also clarifies that the occurrence of inclined lateral crack as shown by 3D cracking behavior may be due to the confinement of concrete surface deformation by the other part with less rebar corrosion. In addition, the parametric study on effect of concrete material properties by the corrosion-expansion model suggest that surface crack initiation is determined by concrete

tensile strength, while fracture energy has a great influence on the propagation of surface and internal cracks.

- (5) The digital image processing method applied in the tensile tests shows satisfactory accuracy for recording the development of local strain, which offers an available method for measurement of large strain in other loading tests. The tensile test results indicate that as corrosion develops the ultimate load of a corroded rebar decreases more than yield load, and elongation is most degraded. The residual tensile performance is largely related to radius loss variability along the rebar length. Local corrosion may result in a more tensile degradation.
- (6) The method for simulating electric corrosion process of rebar is proposed by combining the RBSM and a truss network model. In this method, Laplace equation and Faraday's law are used to evaluate the corrosion profile. Good agreement with the measurements of bare rebar specimens demonstrates that it can be applied to model the corrosion process due to a micro-cell corrosion circuit. The simulation of tensile performance of the corroded specimens is also in agreement with test data, suggesting that the residual performance can be accurately estimated when corrosion profile is taken into consideration.
- (7) An electro-mechanical model is developed on the basis of radius loss to analyze both concrete cracking and rebar tensile degradation. The model takes into account the effect of cracks on the corrosion process by assuming the relationship between current efficiency and crack width, which yields reasonable prediction of development of corrosion degree and corrosion profile compared to the test results. The simulated crack patterns and rebar tensile behavior are also in accordance with experimental results, which confirm the applicability of the time-dependent model to assess the corrosion-caused damages if corrosion occurs consistently along the rebar length. On the other hand, the analysis of the local corrosion case in comparison with the test results indicates that the corrosion process implemented in the test by using a short salt-water pool may be affected by other factors except the applied electric field. The transport and consumption of oxygen needs to be considered in the model for a better modeling, which can assist in the employment of the proposed

electric corrosion method to study corrosion-caused problems of reinforced concrete.

8.2 Recommendations for future study

This study has demonstrated that concrete surface cracking behavior is closely related to internal cracks development, which is affected by corrosion profile of rebar as well as many other factors including geometric features. When local corrosion occurs in the rebar circumferential direction or in the length direction, concrete surface deformation may be confined, leading to inclined lateral cracks inside concrete and a relatively insignificant surface crack. However, for on-site survey and maintenance surface observation is usually served as an important tool. Therefore it is essential to establish a prediction method that is capable of quantitatively evaluating internal crack propagation and rebar corrosion level from observed surface cracking conditions. This is the long-term goal for the improvement of the proposed electro-mechanical model.

The corrosion process of a rebar embedded in concrete is very complicated. It may be affected by many factors, such as transport of chloride ions, oxygen and water, consumption of oxygen as well as external electric field. Moreover, for the natural corrosion process caused by chloride attack, the macro-cell corrosion circuit appears in addition to micro-cell circuit. The proposed model has demonstrated the ability of simulating micro-cell corrosion process controlled by external electric field. To extend the applicability of the proposed model to assess the corrosion caused damage level of RC structures, the improvements accounting for other factors of corrosion process need to be made in the future work.

In this study, the penetration of corrosion products into cracks is not considered in the analytical model, since this effect is considered to have less effect on concrete crack pattern than the corrosion distribution. However, for a quantitative evaluation of crack evolution, the accommodation of corrosion products in cracks needs to be taken into account, which calls for the study of coupled fracture-flow modeling. The truss network model incorporated with the RBSM is capable of simulating diffusion of deleterious matters through cracks (Nakamura et al. 2006), which can be applied and quantified for such study.

References

- Akiyama, M., Frangopol, D.M, Matsuzaki, H., (2014). “Reliability-based durability design and service life assessment of concrete structures in a marine environment.” In: D.M. Frangopol and Y. Tsompanakis Ed. *Maintenance and Safety of Aging Infrastructure*. Florid: CRC Press, 1-26.
- Allam, I.M., Maslehuddin, M., Saricimen, H., Al-Mana, A.I., (1994). “Influence of atmospheric corrosion on the mechanical properties of reinforcing steel.” *Construction and Building Materials*, 8(1), 35-41.
- Almusallam, A.A., (2001). “Effect of degree of corrosion on the properties of reinforcing steel bars.” *Construction and Building Materials*, 15, 361-368.
- Alonso, C., Andrade, C., Rodriguez, J., Diez, J.M., (1998). “Factors controlling cracking of concrete affected by reinforcement corrosion.” *Materials and Structures*, 31, 435-441.
- Andrade, C., Alonso, C., García, D., Rodriguez, J., (1991). “Remaining lifetime of reinforced concrete structures: effect of corrosion in the mechanical properties of the steel.” *Symposium on Life Prediction of Corrodible Structures*. Cambridge, UK: 12/1-12/11.
- Andrade, C., (1993a). “Calculation of chloride diffusion coefficients in concrete from ionic migration measurements.” *Cement and Concrete Research*, 23(3), 724-742.
- Andrade, C., Alonso, C., Molina, F.J., (1993b). “Cover cracking as a function of bar corrosion: Part I – Experimental test.” *Materials and Structures*, 26, 453-464.
- Apostolopoulos, C.A. and Papadopoulos, M.P., (2007). “Tensile and low cycle fatigue behavior of corroded reinforcing steel bars S400.” *Construction and Building Materials*, 21, 855-864.
- Apostolopoulos, C.A., Demis, S., Papadakis, V.G., (2013). “Chloride-induced corrosion of steel reinforcement – mechanical performance and pit depth analysis.” *Construction and Building Materials*, 38, 139-146.

- Bažant, Z.P., (1979). “Physical model for steel corrosion in concrete sea structures – Theory.” *Journal of the Structural Division, Proceedings of the ASCE*, 105(ST6), 1137-1153.
- Bertolini, L., Elsener, B., Pedferri, P., Polder, R.B., (2004). “*Corrosion of steel in concrete*.” Germany: Wiley-VCH, 91-105.
- Cairns, J., Plizzari, G.A., Du, Y.G., Law, D.W., Franzoni, C., (2005). “Mechanical properties of corrosion-damaged reinforcement.” *ACI Materials Journal*, 102(4), 256-264.
- Callahan, J.P., Lott, J.L., Kesler, C.E., (1970). “Bridge deck deterioration and crack control.” *Journal of the Structural Division, Proceedings of the ASCE*, 96(10), 2021-2036.
- Caré, S. and Raharinaivo, A., (2007). “Influence of impressed current on the initiation of damages in reinforced mortar due to corrosion of embedded steel.” *Cement and Concrete Research*, 37, 1598-1612.
- Caré, S., Nguyen, Q.T., Beddiar, K., Berthaud, Y., (2010). “Times to cracking in reinforced mortar beams subjected to accelerated corrosion tests.” *Materials and Structures*, 43, 107-124.
- Chen, D. and Mahadevan, S., (2008). “Chloride-induced reinforcement corrosion and concrete cracking simulation.” *Cement and Concrete Composite*, 30, 227-238.
- Conyers, L.B., (2013). “*Ground-penetrating radar for archeology*.” 3rd ed. Maryland: AltaMira Press, 50.
- Dagher, H.J. and Kulendran, S., (1992). “Finite element modeling of corrosion damage in concrete structures.” *ACI structural Journal*, 89(6), 699-708.
- Djerbi, A., Bonnet, S., Khelidj, A., Baroghel-bouny, V., (2008). “Influence of traversing crack on chloride diffusion into concrete.” *Cement and Concrete Research*, 38, 877-883
- Dekoster, M., Buyle-Bodin, F., Maurel, O., Delmas, Y., (2003). “Modelling of the flexural behavior of RC beams subjected to localized and uniform corrosion.” *Engineering Structures*, 25, 1333-1341.
- Du, Y.G., Clark, L.A., Chan, A.H.C., (2005). “Residual capacity of corroded reinforcing bars.” *Magazine of Concrete Research*, 57(3), 135-147.
- Du, Y.G., Chan, A.H.C., Clark, L.A., (2006). “Finite element analysis of the effects of radial expansion of corroded reinforcement.” *Computers and Structures*, 84, 917-929.

- El Maaddawy, T. and Soudki, K., (2003). "Effectiveness of impressed current technique to simulate corrosion of steel reinforcement in concrete." *Journal of Materials in Civil Engineering*, 15(1), 41-47.
- Gouda, V.K. and Halaka, W.Y., (1970). "Corrosion and corrosion inhibition of reinforcing steel: II. Embedded in concrete." *Corrosion Engineering, Science and Technology*, 5(5), 204-208.
- Grimes, W.D., Hartt, W.H., Turner, D.H., (1979). "Cracking of concrete in sea water due to embedded metal corrosion." *Corrosion*, 35(7), 309.
- Jang, B.S. and Oh, B.H., (2010). "Effects of non-uniform corrosion on the cracking and service life of reinforced concrete structures." *Cement and Concrete Research*, 40, 1441-1450.
- JIS Z 2241 (2011). "*Method of tensile test for metallic materials.*" Tokyo: Japanese Standard Association, Z2241.
- JIS G 3122 (2010). "*Steel bars for concrete reinforcement.*" Tokyo: Japanese Standard Association, G3122.
- JSCE, (2002). "*Standard specifications for concrete structures construction.*" Tokyo: Maruzen.
- Kallias, A.N. and Rafiq, M.I., (2010). "Finite element investigation of the structural response of corroded RC beams." *Engineering Structures*, 32, 2984-2994.
- Kato, B., (1979). "Mechanical properties of steel under load cycles idealizing seismic action." *CEB Bulletin D' Information*, 131, 7-27.
- Kawai, T., (1977). "New element models in discrete structure analysis." *Journal of the Society of Naval Architects of Japan*, 141, 187-193.
- Kawamura, K., Nakamura, H., Kunieda, M., Ueda, N., (2009). "A fundamental study about the evaluation of crack propagation in concrete induced by rebar corrosion." *Proceedings of the JCI*, 31, 1075-1080 [in Japanese].
- Kawamura, K., Tran, K.K., Nakamura, H., Kunieda, M., (2010). "Surface crack propagation behavior against the surface deformation and inside cracks due to rebar corrosion." *Proceedings of the JCI*, 32, 1007-1012 [in Japanese].
- Kirby, G.N., (1996). "The corrosion of carbon and low-alloy steels." In: P.A. Schweitzer Ed. *Corrosion Engineering Handbook*. 2nd ed (3). Florida: CRC Press, 48.

- Lee, H.S. and Cho, Y.S., (2009). "Evaluation of the mechanical properties of steel reinforcement embedded in concrete specimen as a function of the degree of reinforcement corrosion." *International Journal of Fracture*, 157, 81-88.
- Li, C.Q., (2003). "Life-cycle modeling of corrosion-affected concrete structures: propagation." *Journal of Structural Engineering*, ASCE, 129(6), 753-761.
- Li, C.Q., Zheng, J.J., Lawanwisut, W., Melchers, R.E., (2007). "Concrete delamination caused by steel reinforcement corrosion." *Journal of Materials in Civil Engineering*, ASCE, 19(7), 591-600.
- Liu, Y.P. and Weyers, R.E., (1998). "Modeling the time-to-corrosion cracking in chloride contaminated reinforced concrete structures." *ACI Materials Journal*, 95(6), 675-681.
- Lundgren, K., (2002). "Modeling the effect of corrosion on bond in reinforced concrete." *Magazine of Concrete Research*, 54(3), 165-173.
- Mada, T., (2011). "Automatic Fourier analysis by EXCEL." *Technical Report of Technical Service Division, Research Institute for Applied Mechanics, Kyushu University*, 12, 1-8 [in Japanese].
- Malumbela, G., Moyo, P., Alexander, M., (2012). "A step towards standardizing accelerated corrosion tests on laboratory reinforced concrete specimen." *Journal of the South African Institution of Civil Engineering*, 54(2), 78-85.
- Mangat, P. S. and Elgarf, M. S., (1999). "Flexural strength of concrete beams with corroding reinforcement." *ACI Structural Journal*, 96(1), 149-158.
- Maslehuddin, M., Allam, I.M., Al-Sulaimani, G., Al-Mana, A.I., Abduljauward, S.N., (1990). "Effect of rusting of reinforcing steel on its mechanical properties and bond with concrete." *ACI Materials Journal*, 87(5), 496-502.
- Michel, A., Pease, B.J., Peterova, A., Geiker, M.R., Stang, H., Thybo, A.E.A., (2014). "Penetration of corrosion products and corrosion-induced cracking in cementitious materials: Experimental investigations and numerical simulations." *Cement and Concrete Composites*, 47, 75-86.
- Moliton, A., (2007). "*Basic electromagnetism and materials*." New York: Springer. 51-56.
- Mullard, J., Stewart, M.G., (2011). "Corrosion-induced cracking: New test data and predictive models." *ACI Structural Journal*, 108(1), 71-79.

- Nakamura, H., Srisoros, W., Yashiro, R., Kunieda, M., (2006). "Time-dependent structural analysis considering mass transfer to evaluate deterioration process of RC structures." *Journal of Advanced Concrete Technology*, 4(1), 147-158.
- Nguyen, Q.T., Millard, A., Caré, S., L'Hostis, V., Berthaud, Y., (2006). "Fracture of concrete caused by the reinforcement corrosion products." *Journal of Physics IV France*, 136, 109-120.
- Nossoni, G. and Harichandran, R., (2012). "Current efficiency in accelerated corrosion testing of concrete." *Corrosion*, 68(9), 801-809.
- Palsson, R. and Mirza, M.S., (2002). "Mechanical response of corroded steel reinforcement of abandoned concrete bridge." *ACI Structural Journal*, 99(2), 157-162.
- Papadopoulos, M.P., Apostolopoulos, C.A., Alexopoulos, N.D., Pantelakis, S.G., (2007). "Effect of salt spray corrosion exposure on the mechanical performance of different technical class reinforcing steel bars." *Materials and Design*, 28, 2318-2328.
- Papadopoulos, M.P., Apostolopoulos, C.A., Zervaki, A.D., Haidemenopoulos, G.N., (2011). "Corrosion of exposed rebars, associated mechanical degradation and correlation with accelerated corrosion tests." *Construction and Building Materials*, 25, 337-374.
- Poursaeed, A. and Hansson, C.M., (2009). "Potential pitfalls in assessing chloride-induced corrosion of steel in concrete." *Cement and Concrete Research*, 39, 391-400.
- Qiao, D., Nakamura, H., Miura, T., (2014). "Numerical investigation of effects of material properties on corrosion-induced concrete crack propagation." *Proceedings of the JCI*, 36, 1162-1167.
- Qiao, D., Nakamura, H., Yamamoto, Y., Miura, T., (2015a). "Evaluation method of tensile behavior of corroded reinforcing bars considering radius loss." *Journal of Advanced Concrete Technology*, 13, 135-146.
- Qiao, D., Nakamura, H., Tran, K.K., Yamamoto, Y., Miura, T., (2015b). "Experimental and analytical evaluation of concrete cover spalling behavior due to local corrosion." *Journal of Structural Engineering*, JSCE, 61A, 707-714.
- Qiao, D., Nakamura, H., Yamamoto, Y., Miura, T., (2015c). "Analysis of effects of non-uniform corrosion on concrete cracks propagation." *Proceedings of the JCI*, 37, 961-966.
- Rasheeduzzafar, Al-Saadoun, S.S., Al-Gahtani, A.S., (1992). "Corrosion cracking in relation to bar diameter, cover, and concrete quality." *Journal of Materials in Civil Engineering*, 4(4), 327-342.

- Segerlind, L.J., (1984). “*Applied finite element analysis.*” 2nd ed. New York: John Wiley and Sons Press, 138-144.
- Sutton, M.A., Wolters, W.J., Peters, W.H., Ranson, W.F., McNeill, S.R., (1983). “Determination of displacements using an improved digital correlation method.” *Image and Vision Computing*, 1(3), 133-139.
- Toongoenthong, K. and Maekawa, K., (2005). “Simulation of coupled corrosive product formation, migration into crack and propagation in reinforced concrete sections.” *Journal of Advanced Concrete Technology*, 3(2), 253-265.
- Tran, K.K., Nakamura, H., Kawamura, K., Kunieda, M., (2011). “Analysis of crack propagation due to rebar corrosion using RBSM.” *Cement and Concrete Composite*, 33(9), 906-917.
- Treadaway, K.W.J., Cox, R.N., Brown, B.L., (1989). “Durability of corrosion resisting steels in concrete.” *ICE Proceedings*, 86(2), 305-331.
- Tsutsumi, T., Matsushima, M., Murakami, Y., Seki, H., (1996). “Study on crack models caused by pressure due to corrosion products.” *Doboku Gakkai Ronbunshu*, 30(2), 159-166 [in Japanese].
- Val, D.V., Chernin, L., Stewart, M.G., (2009). “Experimental and numerical investigation of corrosion-induced cover cracking in reinforced concrete structure.” *Journal of Structural Engineering*, ASCE, 135(4), 376-385.
- Vu, K., Stewart, M.G., Mullard, J., (2005). “Corrosion-induced cracking: Experimental data and predictive models.” *ACI Structural Journal*, 102(5), 719-726.
- Wang, Y.H., Jiang, J.H., Wanintrudal, C., Du, C., Zhou, D., Smith, L.M., Yang, L.X., (2010). “Whole field sheet-metal tensile test using digital image correlation.” *Experimental Techniques*, 34(2), 54-59.
- Yamamoto, Y., Nakamura, H., Kuroda, I., Furuya, N., (2008). “Analysis of compression failure of concrete by three-dimensional rigid body spring model.” *Doboku Gakkai Ronbunshu*, 64(4), 612-630 [in Japanese].
- Yuan, Y., Ji, Y., Shah, S. P., (2007). “Comparison of two accelerated corrosion techniques for concrete structures.” *ACI Materials Journal*, 104(3), 344-347.
- Yuan, Y.S. and Ji, Y.S., (2009). “Modeling corroded section configuration of steel bar in concrete structure.” *Construction and Building Materials*, 23, 2461-2466.
- Yunovich, M. and Thompson, N.G., (2003). “Corrosion of highway bridges: Economic impact and control methodologies.” *Concrete International*, 25(1), 52-57.

Zhang, W.P., Song, X.B., Gu, X.L., Li, S.B., (2012). "Tensile and fatigue behavior of corroded rebars." *Construction and Building Materials*, 34: 409-417.